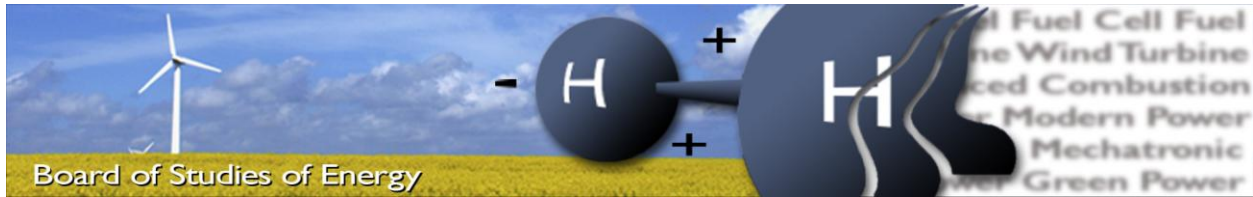


5/27/2014

**AALBORG
UNIVERSITY**

**SENSORLESS CONTROL OF PMSM
USING THREE LEVEL NPC CONVERTER**

Student | Florin Valentin Traian Nica



Title: Sensorless control of PMSM using three level NPC converter
Semester: 10th
Semester theme: Optimisation, Diagnostics and Control of Power Electronic Drives of Converters
Project period: 01.09.2013 – 27.05.2014
ECTS: 50
Supervisor: Ramkrishan Maheshwari; Ewen Ritchie; Krisztina Leban;
Project group: PED4-1045

Florin Valentin Traian Nica

SYNOPSIS:

This project is focused on the construction of a three level neutral point clamped prototype converter, for a wind turbine application. The converter has to ensure the control for a vertical axis Darreius wind turbine, which has special requirements for the system. Two sensorless control strategies are proposed, implemented and tested in laboratory experiments, to determine the best method. The conclusion of the experiments is that sensorless field oriented control is the most adequate control to be implemented for this type of application.

Copies: 3
Pages, total: 83
Appendix: 3
Supplements: CD

By signing this document, each member of the group confirms that all group members have participated in the project work, and thereby all members are collectively liable for the contents of the report. Furthermore, all group members confirm that the report does not include plagiarism.

Preface

The current report, entitled “Sensorless control of PMSM using three level NPC converter” was written by Florin Valentin Traian Nica, master student of Power Electronics and Drives, at the Department of Energy Technology, Aalborg University, Denmark.

The project was proposed by Ewen Ritchie, associate professor, and Krisztina Leban, Ph.D. student, as part of a European Programme contracted by Aalborg University, called DeepWind. The span of the project was one school year, started on 1st of September 2013 and finished on 27th May 2014, thus being the master thesis project of the author.

Reading Instructions

The text is divided into seven chapters plus two appendixes. The chapters are consecutive numbers, whereas the appendixes are labelled with capital letters.

The references are shown in form of number placed into square brackets. Additional information about each reference is presented in Bibliography.

The format of equations is (X.Y), where X is the chapter number and Y is the equation number.

The format of figures is Fig. X.Y, where X is the chapter number and Y is the figure number.

The format of tables is TABLE X.Y, where X is the chapter number and Y is the table number.

The enclosed CD-ROM contains the report in Word and PDF format, two Matlab Simulink models, which present different approaches of constructing the model, an extra Matlab Simulink Library, constructed by the author and images with laboratory results.

Acknowledgments

The author will like show its gratitude to the supervisors, for their extensive support during the entire project period. Special thanks are made to Krisztina Leban and Ewen Ritchie, for their financial and moral support during the two year master programme.

Summary

In order to help the reader understand the structure of the report, a summary of all the chapters is made in the following.

1. Introduction

This chapter presents at the beginning a short retrospective of wind energy evolution during the last years. This retrospective is necessary to understand way the European Union has proposed the DeepWind Programme.

A short description of the DeepWind Programme is presented afterwards, along with the tasks that Aalborg University has to fulfil.

Because one of these tasks represents the starting point for the current master thesis, a more detailed description is made about this task.

The last part of the chapter presents the objectives along with the limitations.

2. Theoretical Background

The most important theoretical concepts used during the project are presented in this chapter.

The chapter starts by presenting the three level neutral point clamped (NPC) converter, because this topology is used for the prototype. Only the most important information about the converter is presented here, along with a selection of references.

The problem and solution for the neutral point voltage balance is presented, because this topic is very important for the NPC, and it is part of the practical implementation.

The chapter continues by presenting the permanent magnet synchronous machine (PMSM) model, in a short section.

The state of the art for scalar and vector control is presented in the last part of the chapter, along with the control theory specific for PMSM.

3. Control Description and Implementation

This chapter presents which control methods are selected for the project. Because a decision was made to use both scalar and vector control, these two are presented separately.

Scalar control is presented first, followed by vector control. As it can be seen from the report, these two control methods have a similar structure with similar components. All these similar components will be presented, in the vector control subchapter, to avoid repeating the same theory twice.

After each control method is described, the implementation process is presented. This implementation process provides the PI controller parameters.

The last part of the chapter presents the speed and position estimator. Although the estimator is used for vector control, it is presented in a separate subchapter, because it represents the most important component of the control.

4. Simulations

Using the information from chapter two and three, a Simulink model of the entire system is created. These simulations were selected based on the second objective.

The results are presented for each simulation, along with necessary explanation.

5. Hardware Design of Converter

The main circuits of the three level NPC prototype are presented in this chapter. Only general block diagrams are used to highlight the main circuits, because the design was not made during this project. For a more detailed description of the prototype and the components, references are provided.

6. Laboratory Experiments

During this chapter, all the laboratory experiments are presented with measurements and explanations. In order to have a comparison between the Simulink model and the real system, the tests are made under similar conditions as the simulations.

7. Conclusions

This chapter presents the main conclusions of the project.

Appendix A. Reference Frame Transformation

The reference frame transformations used in the report are presented.

Appendix B. Neutral Point Voltage Balance Results

The voltage measurements obtained, using space vector modulation, are presented at the beginning. The rest of the appendix presents the DC link voltages for all the experiments, obtained using sinusoidal pulse width modulation.

Appendix C. Numeric Parameters

All the numeric values used during the project are presented in this appendix. These numeric values represent the machine parameters, the control parameters and the convertor parameters.

Contents

1	Introduction.....	1
1.1	Wind Energy Evolution	1
1.2	DeepWind Programme.....	2
1.3	Converter and Control for DeepWind Programme.....	3
1.4	Project Objectives	4
1.5	Project Limitations.....	5
2	Theoretical Background.....	7
2.1	Three Level NPC Converter	7
2.2	Neutral Point Voltage Balance.....	8
2.3	Modulation Strategies	10
2.3.1	Sinusoidal PWM.....	10
2.3.2	Space Vector Modulation	12
2.4	Permanent Magnet Synchronous Machine Model.....	15
2.5	Control of PMSM	17
2.5.1	Scalar Control	17
2.5.2	Vector Control	19
3	Control Description and Implementation.....	21
3.1	Scalar Control (I-f Control)	21
3.2	Vector Control (Field Oriented Control)	23
3.2.1	Controller Design Requirements.....	25
3.2.2	Current Controller.....	25
3.2.3	Flux control loop.....	30
3.2.4	Speed Controller	30
3.2.5	Anti-Windup	33
3.3	Rotor Position Estimation.....	34
4	Simulations	37
4.1	Model Overview	37
4.2	Scalar Control Simulations	38
4.2.1	Speed reference variation.....	38

4.2.2	Load torque variation	40
4.3	Vector Control Simulations	41
4.3.1	Speed reference variation.....	41
4.3.2	Load torque variation.....	43
4.3.3	Transition from motor to generator.....	43
4.3.4	Emergency breaking	44
4.3.5	Holding the machine at zero speed	46
5	Hardware Design of Converter	49
5.1	General Structure	49
5.2	Power Side	50
5.3	Control Side	51
6	Laboratory Experiments.....	57
6.1	Laboratory Setup.....	57
6.2	Scalar Control Experiments	58
6.2.1	Speed reference variation.....	58
6.2.2	Load torque variation.....	59
6.3	Vector Control Experiments	60
6.3.1	Speed reference variation.....	60
6.3.2	Load torque variation.....	61
6.3.3	Transition from motor to generator.....	62
6.3.4	Emergency breaking	64
6.3.5	Holding the machine at zero speed	65
7	Conclusions.....	67
Appendix A.	Reference Frame Transformation.....	69
Appendix B.	Neutral Point Voltage Balance Results	73
Appendix C.	Numeric Parameters	77

1 Introduction

This chapter presents the wind energy evolution in the last years at a global level. The focus will be then changed to the European Union and its programmes, which support the development of renewable energies. A short presentation of one of these programmes, contracted by Aalborg University, called DeepWind, will be made, to relate the requirements of the programme with the project at hand. The objectives of this project will be presented in the second part, along with necessary information for each objective. The final part of the chapter will present the limitations imposed for the project.

1.1 Wind Energy Evolution

Political and economical conditions have lead to a significant increase in research and development of renewable energies in the last decade [1, 2]. Because of this, wind energy has become one of the mainstream renewable technologies with more than 300,000MW installed globally until 2013 [2], as it can be seen from Fig. 1.1.

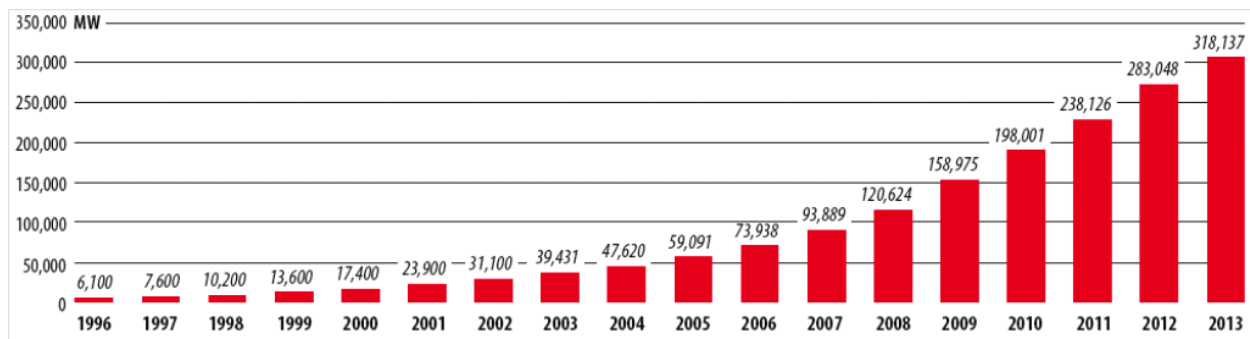


Fig. 1.1. Global cumulative installed wind capacity 1996-2013 [2].

From the total amount of wind power installed globally until 2013, Europe is the leading region, with 38% of the total installed renewable power [2], which covers approximately 7% of the electricity demand.

Europe is the leader in installed wind power due to the policies implemented, and due to the long term objectives imposed by the European Union [3]. These targets, presented in [3], require that by 2050, 50% of the energy consumed in Europe to be produced by wind turbines.

In order to achieve this goal, massive investments are made in research and development, to increase the energy capacity of each generator, and to provide better solutions for the structure [3]. As a result, the average generator capacity installed each year has increased from 200kW for onshore and 450kW for offshore in 1991, to 1,700kW for onshore and 2,800kW for offshore in

2010 [3]. This trend is expected to be maintained in the future, allowing for an increase above 3,000kW.

TABLE 1.1.
LONG TERM OBJECTIVES SET BY THE EU REGARDING WIND POWER [3].

	Onshore wind (GW)	Offshore wind (GW)	Total wind energy capacity (GW)	Average capacity factor onshore	Average capacity factor offshore	(TWh) onshore	(TWh) offshore	(TWh) total	EU-27 gross electricity consumption	Wind power's share of electricity demand
2020	190	40	230	26%	42.3%	433	148	581	3,690	16%
2030	250	150	400	27%	42.8%	591	562	1,154	4,051	29%
2050	275	460	735	29%	45%	699	1,813	2,512	5,000	50%

The European Union is supporting this development through Framework Programmes since 1984 and plans to continue at least until 2020 [4]. Aalborg University is one of the participants engaged in one of these programmes called DeepWind [5]. A short description of the programme is presented in the following section.

1.2 DeepWind Programme

The DeepWind programme was proposed on the hypothesis that a new wind turbine concept, developed specifically for offshore, has potential for better cost efficiency than existing offshore technology [5].

Considering this hypothesis a series of objectives have been set [5]:

- To explore the technologies needed for development of a new, simple, floating offshore concept, with a vertical axis rotor, and a floating and rotating foundation;
- To develop calculation and design tools for development and evaluation of very large wind turbines, based on this concept;
- Evaluation of the overall concept with floating offshore horizontal axis wind turbines;

As part of the DeepWind programme Aalborg University is responsible for a series of tasks:

- Design the bearings of the wind turbine;
- Construct a design tool which is able to design a wind turbine generator in the range of 5 to 20MW, specific for an offshore application;
- Propose a converter topology adequate for this application;

As an integrated part in the DeepWind Programme, the current master thesis focuses on the converter topology for the wind turbine.

1.3 Converter and Control for DeepWind Programme

In order to identify the best converter topology for the current application, a student project was proposed at Aalborg University [6]. The project concluded that the best topology to be used in this situation is the three level neutral point clamped (NPC) converter [6].

This converter topology is preferred, instead of the two level converter, which is most widely used, because of its advantages as: reduced voltage across each switch (only half of the DC link voltage per each switch, compared to the entire DC link voltage per each switch, for the two level), reduced current ripple losses, reduced switching/conduction losses and reduced total harmonic distortion.

The decision was made to use the three level NPC converter. A small scale prototype of the converter is built. This step is considered to be the first objective of the current master thesis, which will be presented in more detail in the following subchapter.

Although the control of the converter is not a task required for Aalborg University, by the DeepWind Programme, it will be considered as an objective for the current master thesis.

When the control strategy is developed, the particularities specific to this application must be taken into consideration. As a start, it should be noted that the participants engaged in this project, responsible with the structure of the wind turbine, have proposed a vertical axis Darrieus type turbine.

This turbine has to be anchored to the bottom of the sea, leaving the entire structure to float. Because of the uniqueness of the construction, the generator along with the converter will be located underwater, at the bottom of the wind turbine.

The Darrieus wind turbine imposes special requirements for the control strategy, requirements which must be taken into consideration when the control is elaborated. These special requirements, specific to the Darrieus wind turbine, are presented in the following:

- The unique structure restricts it from self-starting even with high levels of wind speed. Hence, the generator will have to work as a motor in the starting phase and accelerate the turbine until a certain rotating speed is reached. During the start procedure, since the machine will be working as a motor, power will be consumed from the grid;
- Stopping the turbine. The size and weight of the entire structure creates a very large moment of inertia, and because the turbine cannot be stopped using traditional mechanical breaks, the generator has to be able to stop the entire structure;
- Pitch control cannot be implemented for this system, since the blades of the turbine are fixed. Hence the entire structure will have to be controlled by the generator via the converter.

Based on the information presented and the requirements imposed by the DeepWind Programme, the objectives for the current master thesis can be elaborated.

1.4 Project Objectives

To have a clear understanding of why the following objectives are selected for this project, each objective will be presented in a separated section, along with all the necessary information.

Objective 1:

A three level NPC prototype converter has to be constructed.

The prototype is constructed as a requirement of the DeepWind Programme, to test the topology proposed for the main converter. A secondary reason is that the converter has to drive a small scale generator prototype, which was constructed to test the analytical design program.

The main beneficiaries of this objective are the people involved in the DeepWind project and the author of this thesis, because of the experience gained while constructing a convertor and working in a laboratory.

The PCB schematics used in the current project are taken from a previous AAU project [7], in order to save time with converter design. All the components are ordered according to the bill of materials, provided in the project, and the soldering and testing part is made by the author, in the laboratory.

Objective 2:

Propose suitable control strategies for the converter, in different working situations as:

- starting the turbine as motor;
- working as a motor;
- working as a generator;
- emergency breaking;
- holding the turbine at zero speed;

The Darreius wind turbine imposes special requirements for the converter, like the ones presented in the Converter and Control for DeepWind Programme subchapter presented earlier. The control implemented on the converter has to be able to handle all these situations;

The main beneficiary of this objective is the author conducting this report, because it has to study the state of the art methods in control strategies, and propose suitable ones for this project. Also the DeepWind Programme will benefit from this objective, ensuring that tests can be made in different situations.

To complete this objective, a review of the state of the art methods in control is made. Using the information gained, the most suitable method that can be applied on this system is selected.

Objective 3:

Construct a mathematical model of the system and simulate the proposed control strategies.

The simulations are made to: test the functionality of the system, test the control strategies selected during the previous objective and to improve the control by tuning the system. Also, the

simulation provides important information before the real system is tested, information which can be used to improve the system and to reduce the implementation time.

After the model is constructed in Matlab Simulink, the control is implemented to drive the system. In order to validate the control, numerous simulations are made using the conditions imposed at objective two.

Objective 4:

Test the converter in the laboratory for all the situations simulated.

On the constructed converter, the proposed control strategies are tested to validate the behaviour of the system and to verify its functionality.

The author of this report is the main beneficiary of this objective because it has the chance to learn how to build a setup in the laboratory, study, develop and implement DSP programming on the convertor and test the overall system;

With the constructed converter, and the available machine prototype, provided by the DeepWind project, the setup is made. The control is implemented on a DSP, thus providing the control for the converter.

1.5 Project Limitations

Because of limited time and/or resources some limitations have to be imposed to the project:

- The design of the converter is not an objective for this project. The design presented in [7] will be used to construct the converter.
- Sinusoidal pulse width modulation, without DC balance capabilities, is used in laboratory experiments;
- Because field weakening control is not an objective for this project, it was only presented as a theoretical concept. Experimental tests were made in the laboratory, using this control, but are not presented in the report.

2

Theoretical Background

This chapter presents the main theoretical topics that will be required to handle the objectives. The focus is placed on the most important components of the system: converter, machine and control. In the first section, a short description of the three level NPC converter is made, information which is required to understand its structure and functionality. The model of the permanent magnet synchronous machine in rotating “dq” reference frame is presented afterwards. The state of the art control methods that can be applied for this type of machine are presented in the last section.

2.1 Three Level NPC Converter

The circuit diagram of a three level neutral point clamped (NPC) converter is presented in Fig. 2.1. [8]. It can be observed that two capacitors (C_{d1}, C_{d2}) are placed on the DC link, creating a neutral point 0. The two diodes connected to the neutral point (D_{c1}, D_{c2}) are called clamping diodes. E is the voltage across the DC capacitors and it is normally half of the DC voltage V_{dc} , but neutral point voltage deviation can appear because the capacitors are charged and discharged by the neutral current i_0 [8].

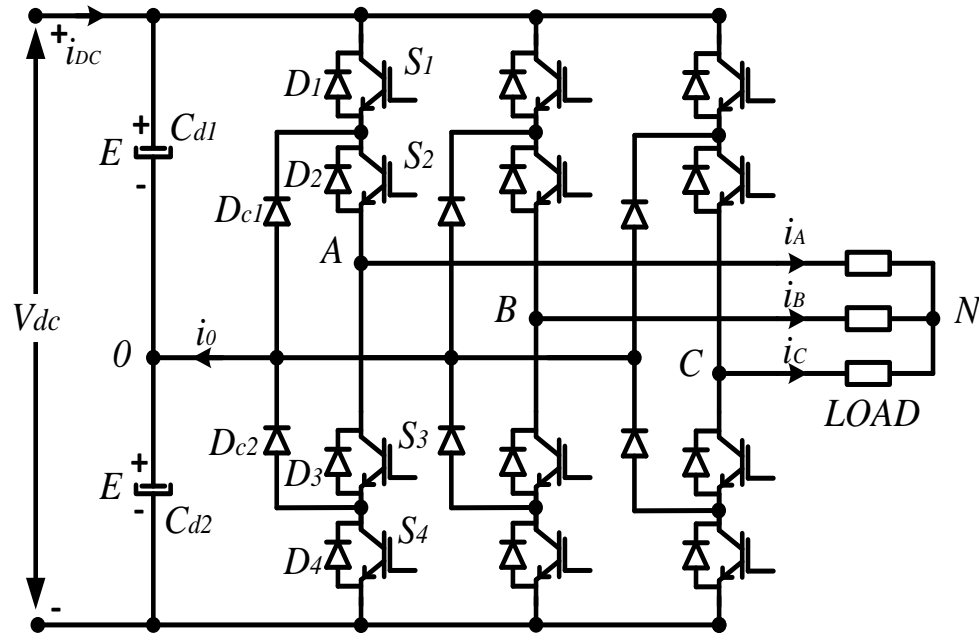


Fig. 2.1. Three level NPC converter [8]

The working procedure of the converter is represented by the switching states of each phase. Since the procedure is similar for each phase, only the switching states for phase A are presented in TABLE 2.1.

TABLE 2.1
SWITCHING STATES FOR ONE PHASE OF THE CONVERTER

Switching State	Switching State for Phase A				Phase Voltage (V_{A0})
	S1	S2	S3	S4	
P	On	On	Off	Off	E
0	Off	On	On	Off	0
N	Off	Off	On	On	-E

As it can be seen from the table, in order to obtain at the output of the converter a positive voltage equal with the voltage across the capacitor E , the upper two switches S_1 and S_2 have to be on and the lower two switches S_3 and S_4 have to be off. This is also called the P switching state because it produces a positive voltage at the output.

To obtain a negative voltage at the output, with the same magnitude, the status of the switches has to be opposite to the P state, and this is called N switching state.

The three level NPC converter is also able to produce a zero voltage level at the output, which is determined by the switching state 0 , when the interior switches (S_2 and S_3) are on, and the exterior switches are off (S_1 and S_4).

From these three switching states (P , N and 0) it should be noted that switch one and switch three always work in opposition ($S_1 = \bar{S}_3$), same as switch two and four ($S_2 = \bar{S}_4$).

By properly controlling these switching states, on all three phases, the neutral point voltage unbalance can be eliminated. The reasons why this phenomenon can appear are presented in the following section.

2.2 Neutral Point Voltage Balance

The neutral point voltage balance can be influenced by numerous parameters [8], as: different parameters for the DC link capacitors, DC capacitor failure, different parameters for the switching devices and unbalanced loads.

If the neutral point voltage balance problem is not considered and corrected, problems can appear in the system [8], as: premature failure of the switching devices, increased total harmonic distortion, modulation ratio limited by the terminal with the lower voltage.

This problem can be solved by applying the adequate switching state on each of the three phases. To have a unified notation of the switching state on all three phases, the space vector term was introduced [8]. The space vector considers the switching state on each phase, by using the output phase voltage, and it can be expressed using the following equation:

$$\vec{V}_s = \frac{2}{3} [V_{A0} + aV_{B0} + a^2V_{C0}] \quad (2.1)$$

, where: \vec{V}_s - space vector;

V_{A0} - voltage on phase A (considering the neutral point 0 as reference);

$$a = e^{j(2\pi/3)};$$

A more detailed explanation regarding the space vector term will be made in the following sections. At this point it is sufficient to know that the three level NPC converter has the ability to generate four groups of space vectors based on their magnitude, each corresponding to different switching states (TABLE 2.3).

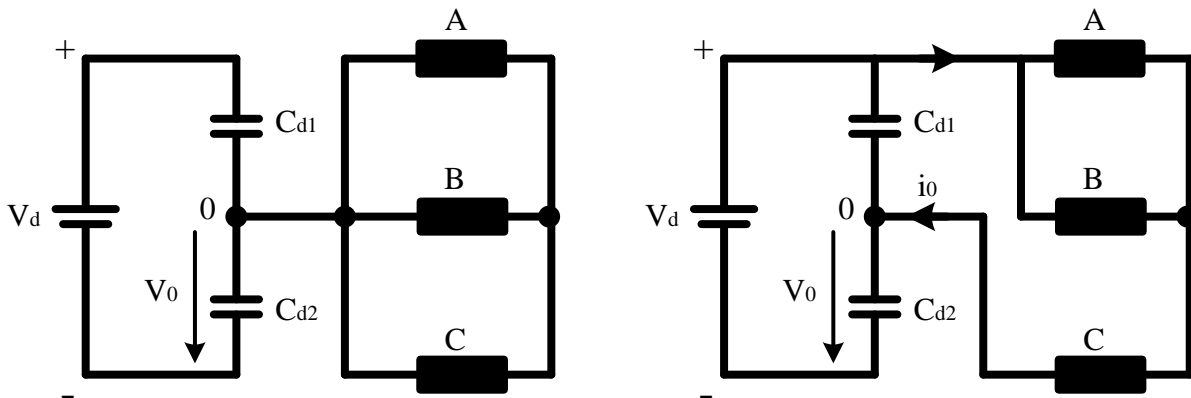
Each of these space vectors has a different influence on the neutral point voltage [8], influence that will be analyzed in the following, using the switching states presented in Fig. 2.2.

Zero space vectors (Fig. 2.2.a.) have no influence on the neutral point voltage balance, because they ensures the connection of the converter terminals (A, B and C) with only one of the DC states at a time (positive, zero or negative DC voltage) [8].

Small space vectors have a powerful influence over the voltage balance. This is because when a P switching state is active (Fig. 2.2.b.), the load is connected between the positive DC voltage and neutral point, causing the current i_0 to flow towards the neutral point 0, which increases V_0 . In the opposite situation, when an N switching state is active (Fig. 2.2.c.), the current i_0 flows from the neutral point 0 towards the negative point N, causing a decrease in V_0 [8].

Medium space vectors (Fig. 2.2.d.) also have an influence over the neutral point voltage balance. Even though at each moment one converter terminal is connected to a different DC point, the voltage V_0 can increase or decrease depending on the operating condition [8].

Large space vectors (Fig. 2.2.e.) do not affect the voltage balance of the neutral point [8]. This is because the load terminals are connected between the positive and negative DC terminals, while the neutral point is left unconnected [8].



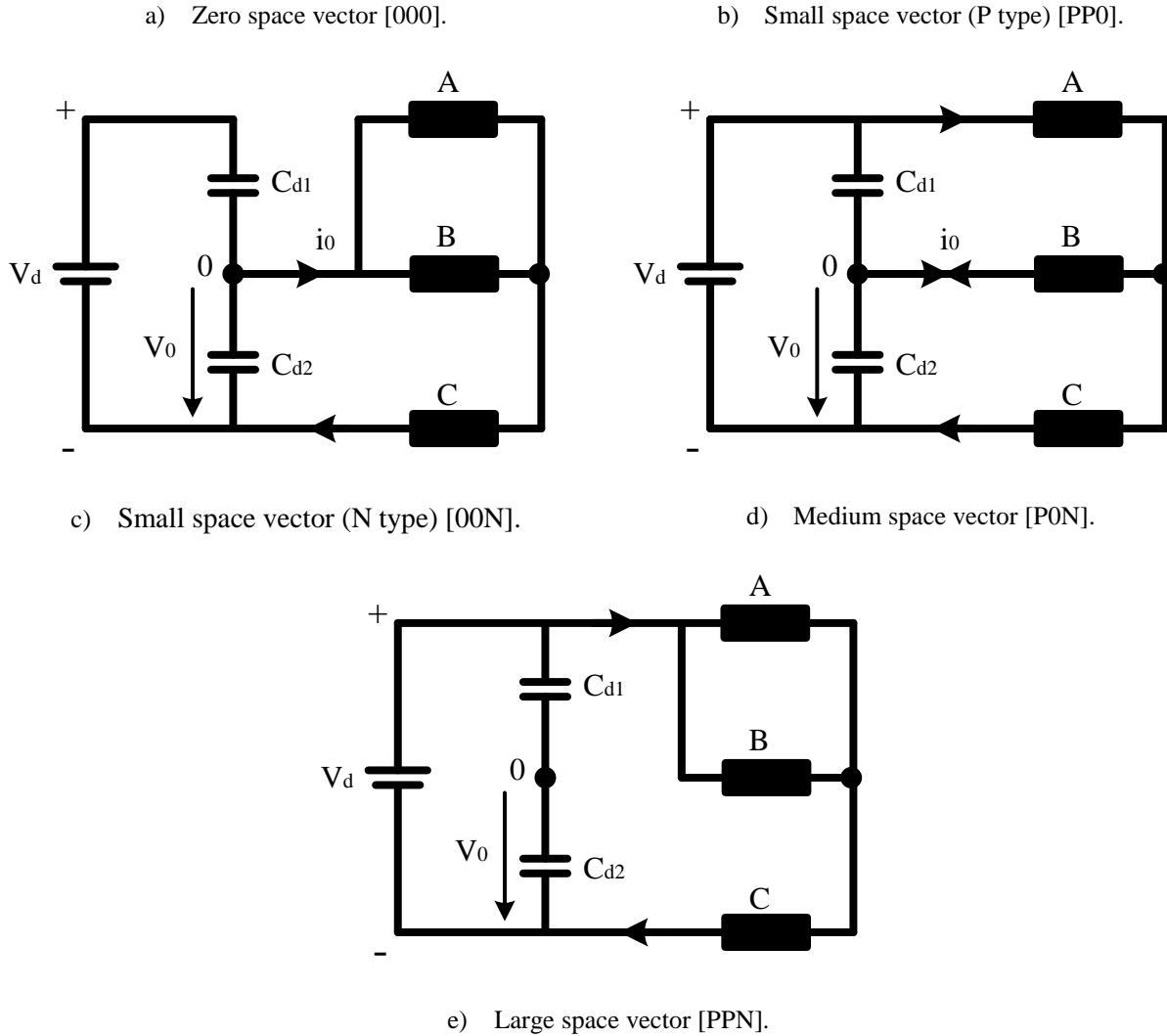


Fig. 2.2. Effect of space vectors on neutral point voltage balance [8].

By adequately controlling the space vectors during the modulation, neutral point voltage balance can be achieved. Two of the most widely used modulation strategies will be presented in the following.

2.3 Modulation Strategies

Numerous modulation strategies have been proposed for the three level NPC converter [9]. The most common known and used are:

- Sinusoidal pulse width modulation (SPWM);
- Space vector modulation (SVM);

2.3.1 Sinusoidal PWM

This method is based on the comparison between a sinusoidal reference signal and two carrier signals (V_{c1}, V_{c2}).

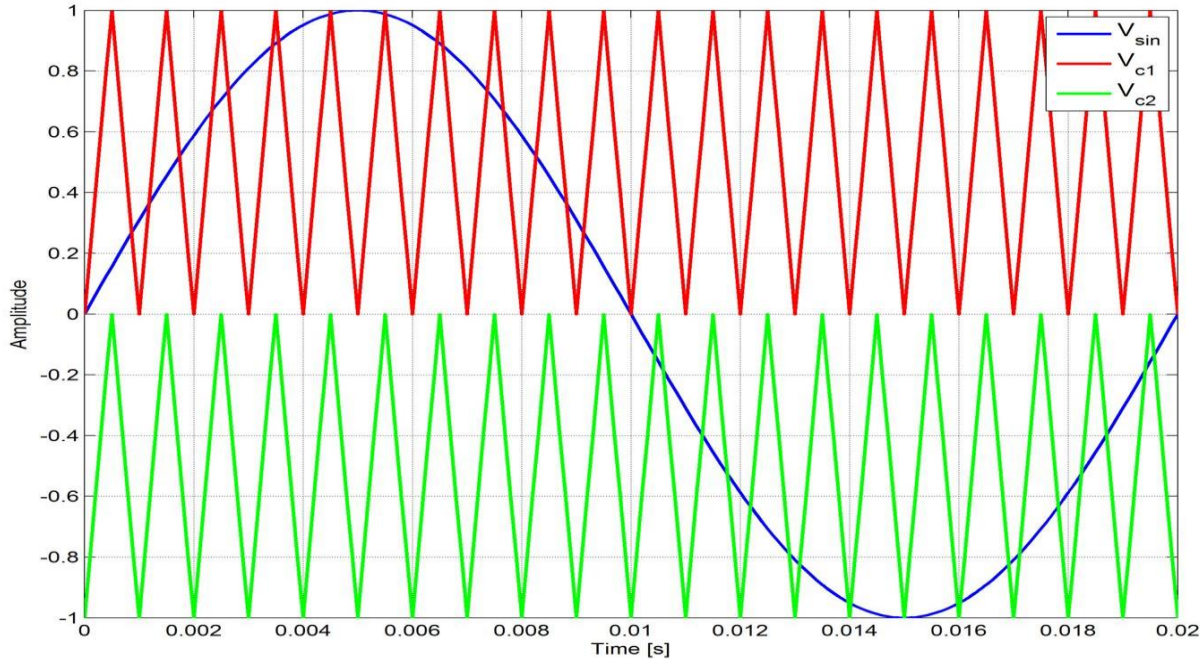


Fig. 2.3. Sinusoidal PWM.

Because the first carrier signal V_{c1} is always bigger than the second carrier signal V_{c2} , and because the switches work in opposition ($S_1 = \bar{S}_3$ and $S_2 = \bar{S}_4$), it is sufficient to define two states for the PWM logic (TABLE 2.2).

TABLE 2.2
LOGIC OF THE CARRIER BASED PWM METHOD

Cases	Switch State
$V_{sin} > V_{c1}$	$S_1 = \bar{S}_3 = ON$
$V_{sin} < V_{c2}$	$S_2 = \bar{S}_4 = ON$

Besides the classical method presented here, where the modulation signal is sinusoidal with only one frequency component, there are numerous other sinusoidal PWM strategies developed to improve the quality of the result [9].

SPWM can be used as a modulation strategy because it ensures a natural balance in the DC link, when no external factors affect the system. The disadvantage of this method appears when an external factor influences the DC neutral point voltage. In this situation the balance cannot be ensured, which can cause a fault to appear in the system.

In order to provide a safe operation, even when external factors affect the DC link voltage, a different modulation strategy has to be used. This strategy is presented in the following.

2.3.2 Space Vector Modulation

The three level NPC converter has $3^3=27$ switching states combinations, which can generate different space vectors. A classification of all the space vectors obtained using (2.1) is made based on magnitude and type, in TABLE 2.3.

TABLE 2.3
VOLTAGE VECTORS AND SWITCHING STATES [8]

Vector Classification	Vector Magnitude	Space Vector	Switching State		
			P type		N type
Zero Vector	0	\vec{V}_0	000	PPP	NNN
Small Vector	$\frac{1}{3}V_{dc}$	\vec{V}_1	P00		0NN
		\vec{V}_2	PP0		00N
		\vec{V}_3	0P0		NON
		\vec{V}_4	0PP		N00
		\vec{V}_5	00P		NN0
		\vec{V}_6	POP		ON0
Medium Vector	$\frac{\sqrt{3}}{3}V_{dc}$	\vec{V}_7		PON	
		\vec{V}_8		OPN	
		\vec{V}_9		NP0	
		\vec{V}_{10}		NOP	
		\vec{V}_{11}		ONP	
		\vec{V}_{12}		PNO	
Large Vector	$\frac{2}{3}V_{dc}$	\vec{V}_{13}		PNN	
		\vec{V}_{14}		PPN	
		\vec{V}_{15}		NPN	
		\vec{V}_{16}		NPP	
		\vec{V}_{17}		NNP	
		\vec{V}_{18}		PNP	

As it can be observed from TABLE 2.3 and from Fig. 2.2, only the small space vector has two switching state types, positive and negative. These two types produce a space vector with the same magnitude and angle. The difference between the two switching states is the direction of the neutral current i_0 . For the positive type the current enters the DC link, while for the negative type the current is taken out of the DC link.

Using the space vectors presented in TABLE 2.3 in the correct manner, the neutral point voltage balance can be maintained, even when external influences affect the DC voltage [8]. A modulation technique which has this capability is presented in the following [7].

In order to understand which space vectors must be for each situation, all the space vectors are arranged in a diagram made out of six sectors, each sector having two regions, as it can be seen in Fig. 2.4 and Fig. 2.5.

From Fig. 2.5, it can be seen that the first region is situated between $[0^\circ, 30^\circ]$ and the second region is situated between $[30^\circ, 60^\circ]$. Another important information that has to be considered is that each region contains four space vectors. For example, sector one, region one contains: \vec{V}_0 , \vec{V}_1 , \vec{V}_7 and \vec{V}_{13} .

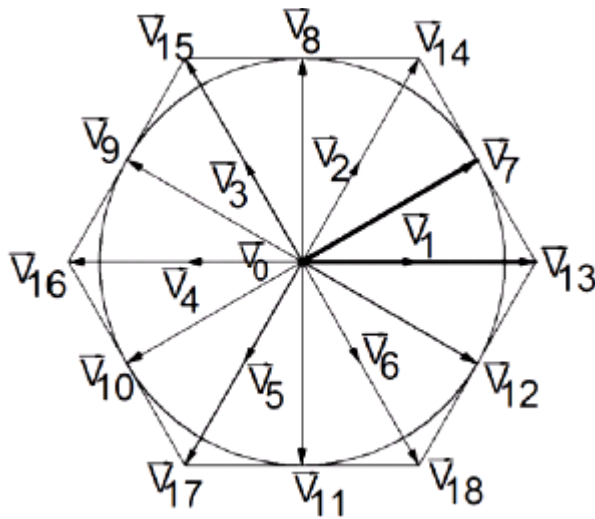


Fig. 2.4. Space vector diagram divided in sectors and regions [7].

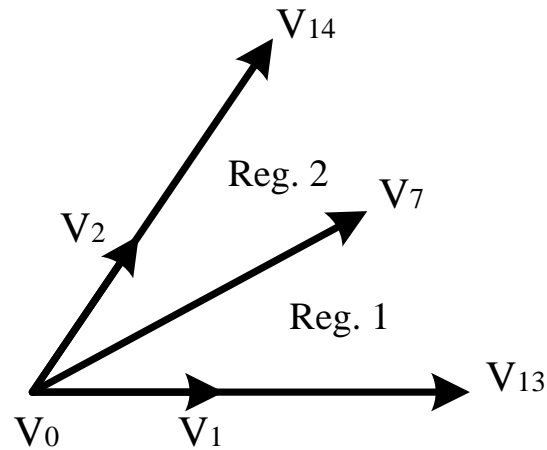


Fig. 2.5. Space vector from sector 1, region 1 and 2.

The neutral point voltage balance is maintained by alternating the small space vector from positive type to negative type, when there is no fault in the system. When the voltage on the lower capacitor (V_0) increases above a predefined value, the negative type small space vector is used in the modulation, to draw the current out of the DC link. In the opposite situation, when the voltage on the lower capacitor (V_0) decreases below a predefined value, the positive type small space vector is used, to send current to the DC link.

In order to use all four space vectors the modulation index has to be considered. The modulation index is defined as:

$$m_i = \sqrt{3} V_{ref} / V_{dc} \tag{2.2}$$

, where: V_{ref} - magnitude of the reference voltage;

The modulation index is in the $[0, 1]$ range because the maximum magnitude of the reference vector \vec{V}_{ref} corresponds to the radius of the largest circle that can be inscribed within the hexagon in Fig. 2.4, which is equal to the medium space vectors.

The modulation index will determine the dwell time for the zero space vector \vec{V}_0 according to:

$$T_d = (1 - m_i) \cdot T_s \quad (2.3)$$

, where: T_d - dwell time for the zero space vector;

T_s - sampling time;

As it can be seen from (2.3), if the modulation index is equal to one, the zero space vector is not used.

In order to calculate the required dwell time for the other three space vectors, the volt-second balance principle is applied.

This principle states that the product between the reference voltage \vec{V}_{ref} and the sampling time T_s is equal to the sum of voltage multiplied by the time of the chosen space vectors [8].

To better explain this principle it will be consider that the voltage reference vector \vec{V}_{ref} is situated in sector one, region one. This means that the nearest three vectors are \vec{V}_1 , \vec{V}_7 and \vec{V}_{13} .

Based on the volt-second balance principle the equations can be written:

$$\vec{V}_1 t_a + \vec{V}_7 t_b + \vec{V}_{13} t_c = \vec{V}_{ref} T_s \quad (2.4)$$

$$t_a + t_b + t_c = T_s \quad (2.5)$$

, where: t_a , t_b , and t_c are the calculated dwell times for \vec{V}_1 , \vec{V}_7 and \vec{V}_{13} , not the final dwell times.

The space vectors are expressed in the following form:

$$\vec{V}_{ref} = V_{ref} e^{j\theta} \quad \vec{V}_1 = \frac{1}{3} V_{dc} \quad \vec{V}_{13} = \frac{2}{3} V_{dc} \quad \vec{V}_7 = \frac{\sqrt{3}}{3} V_{dc} e^{j\pi/6} \quad (2.6)$$

Substituting (2.6) in (2.4) yields:

$$\frac{1}{3} V_{dc} t_a + \frac{\sqrt{3}}{3} V_{dc} e^{j\pi/6} t_b + \frac{2}{3} V_{dc} t_c = V_{ref} e^{j\theta} T_s \quad (2.7)$$

From (2.7), if Euler's formula is applied and the real part is separated from the imaginary part the following two equations can be obtained [8]:

$$Re: \quad t_a + \frac{3}{2} t_b + 2 \cdot t_c = \sqrt{3} m_i T_s \cos \theta \quad (2.8)$$

$$Im: \quad \frac{1}{2} t_b = m_i T_s \sin \theta \quad (2.9)$$

Because there are three unknowns t_a , t_b , and t_c and only two equations (2.8) and (2.9), equation (2.5) is added to the system. Solving the system of equations and extracting the modulation index from each equation will result in:

$$t_a = 2T_s - T_s(\sqrt{3} \cdot \cos \theta + \sin \theta) \quad (2.10)$$

$$t_b = 2T_s \sin \theta \quad \text{for } \theta \in \left[0, \frac{\pi}{6}\right] \quad (2.11)$$

$$t_c = -T_s + T_s(\sqrt{3} \cdot \cos \theta - \sin \theta) \quad (2.12)$$

Because there are four space vectors used for modulation, the calculated dwell times t_a , t_b , and t_c are must be divided by the modulation index. The division creates the required time for the zero space vector. The four dwell times used in the modulation are:

$$T_a = \frac{t_a}{m_i} \quad T_b = \frac{t_b}{m_i} \quad T_c = \frac{t_c}{m_i} \quad T_d = (1 - m_i) \cdot T_s \quad (2.13)$$

The same procedure is applied for the second region and the calculated dwell times are:

$$t_a = 2T_s - T_s(\sqrt{3} \cdot \cos \theta + \sin \theta) \quad (2.14)$$

$$t_b = T_s(\sqrt{3} \cdot \cos \theta - \sin \theta) \quad \text{for } \theta \in \left[\frac{\pi}{6}, \frac{\pi}{3}\right] \quad (2.15)$$

$$t_c = -T_s + 2T_s \sin \theta \quad (2.16)$$

If the reference vector is placed in another sector (II to VI) the same equations as for the first sector can be used, keeping into consideration the difference between region one and two. Before the dwell time calculations, the angle has to be reduced to the first sector, as in (2.17).

$$\theta_n = \theta - \frac{\pi}{3}(n - 1) \quad (2.17)$$

, where: θ_n – the angle reduced to sector one;

θ – reference vector position (angle of $\overrightarrow{V_{ref}}$);

n – the sector number.

2.4 Permanent Magnet Synchronous Machine Model

In order to construct the mathematical model of a permanent magnet synchronous machine (PMSM) the following assumptions are made [10]:

- Saturation is neglected;
- The induced electromagnetic force (EMF) is sinusoidal;
- Eddy currents and hysteresis losses are negligible;
- There are no field current dynamics;
- The “d” axis is aligned with the permanent magnet flux linkage(λ_{pm});

The voltage equations in rotating “dq” reference frame are:

$$v_d = R_s i_d + \frac{d\lambda_d}{dt} - \omega_r \lambda_q \quad (2.18)$$

$$v_q = R_s i_q + \frac{d\lambda_q}{dt} + \omega_r \lambda_d \quad (2.19)$$

, where: $v_{d,q}$ - voltage on d, q axis [V];

$i_{d,q}$ - current on d, q axis [A];

R_s - stator resistance [Ω];

$\lambda_{d,q}$ - flux linkage on d, q axis [Wb];

ω_r - rotor electrical speed [rad/sec];

The flux equations are:

$$\lambda_d = L_d i_d + \lambda_{pm} \quad (2.20)$$

$$\lambda_q = L_q i_q \quad (2.21)$$

, where: $L_{d,q}$ - inductance on d, q axis [H];

λ_{pm} - flux linkage due to magnets placed on the rotor, which links the stator [Wb];

The electromagnetic torque equation is:

$$T_e = \frac{3}{2} p [(L_d - L_q) i_d + \lambda_{pm}] i_q \quad (2.22)$$

, where: T_e – electromagnetic torque [N · m];

p - number of pole pairs;

For the special case presented by the PMSM, where the inductances along the d and q axes are equal ($L_d = L_q$), equation (2.22) can be simplified to:

$$T_e = \frac{3}{2} p \lambda_{pm} i_q \quad (2.23)$$

The dynamic equation for the speed of the machine is:

$$J \frac{d\omega_m}{dt} = T_e - T_L - B \omega_m \quad (2.24)$$

, where: J - moment of inertia [$\text{kg} \cdot \text{m}^2$];

ω_m – rotor mechanical speed [rad/sec];

T_L - load torque [N · m];

B – viscous friction constant [-];

2.5 Control of PMSM

Depending on the multitude of application where drives are being used, numerous types of control strategies have been developed during the time, starting from the most basic ones, as using a variable resistor to manipulate the voltage, to the most advance ones as servo-drive control [11]. The difference between all these control strategies is in the ease of implementation, performance and cost. In order to have an idea of the difference between different control strategies a comparison from [11] is presented in the following.

TABLE 2.4

PERFORMANCE COMPARISON BETWEEN DIFFERENT CONTROL STRATEGIES AND POSSIBLE APPLICATIONS [11]

	Simple Scalar Control	Scalar Control (compensated)	Voltage Vector Control	Flux Vector Control	Servo Drive
Speed Range	1:10 (open loop)	1:25 (open loop)	1:50 (open loop)	1:10000 (closed loop)	1:10000 (closed loop)
Static Speed Accuracy	5 %	2 %	1 %	0 %	0 %
Torque Rise Time	Not available	Not available	10 ms	< 1 ms	< 1 ms
Speed Rise Time	> 100 ms	> 50 ms	> 20 ms	< 10 ms	< 10 ms
Starting Torque	Low	Medium	High	High	High
Cost	Very Low	Low	Medium	High	High
Possible Applications	Pumps, Fans	Conveyors	Crane, Pack	Crane, Lifts	Robots

As it can be seen from TABLE 2.4, only control strategies that can be implemented on converters are presented. These control strategies can be separated in two classes, scalar control and vector control. Both scalar and vector control strategies are implemented in the current project to test the theoretical concept on a real system and to get a better knowledge of how the methods behave. To do so, first, the state of the art of each control strategy is presented in the following of this chapter. After the state of the art, the control methods selected for this project are presented in more detail in the following chapter, along with the implementation method.

2.5.1 Scalar Control

Being initially developed for the induction machine, this motor drive control strategy is used in systems which do not require high dynamic performances because of its simplicity and low cost [11, 12].

As a speed control strategy it takes into consideration two of the properties specific for the induction machine [12]:

- The torque-speed characteristic is predominantly steep in the region of synchronous speed, which means that the electrical rotor speed is close to the electrical frequency. By controlling the frequency, the speed of the machine can be controlled;
- The voltage equation (2.25), expressed in steady state, highlights the fact that the flux linkage term has a much higher influence than the resistive term in the voltage equation for medium to high speed situation.

$$\bar{v}_s = R_s \bar{i}_s + j\omega_r \bar{\lambda}_s \quad (2.25)$$

$$\Lambda_s = \frac{V_s}{\omega_r} = \frac{V_s}{2\pi f} \quad (2.26)$$

, where: Λ_s - magnitude of the stator flux linkage;

V_s - magnitude of the applied voltage;

As it can be seen in equation (2.26), the magnitude of the flux linkage is in fact the ratio between the magnitude of the applied voltage, and rotor electrical speed. This helps us understand that in order to maintain a constant flux linkage, to avoid saturation, the ratio should be kept constant [12]. This ratio also gives the name of this method, being widely known as V/f control.

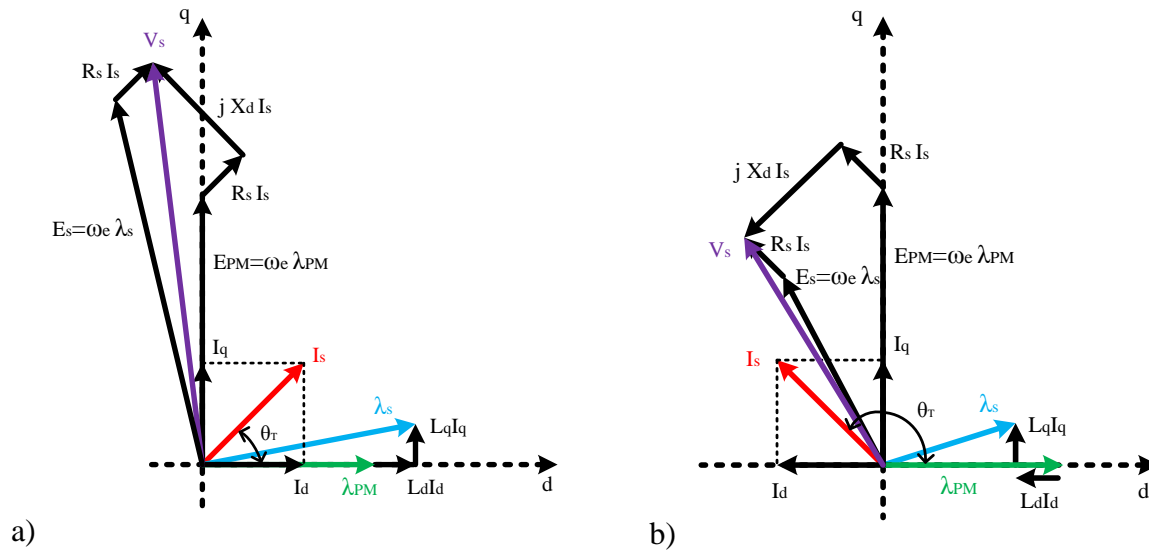


Fig. 2.6. Phasor diagram of PMSM with d-axis aligned with the rotor magnet flux λ_{pm} [13].

The phasor diagrams of the PMSM presented in Fig. 2.6 are used to better understand the main disadvantage of this control strategy. By only controlling the voltage and the frequency, and not the current on the direct and quadrature axis, the magnetisation of the machine cannot be control properly [12, 13].

As stated in [12, 13], high values of V/f cause an increase in the direct axis component of the current i_d , which produces an over-excitation in the machine Fig. 2.6 a). On the other hand, for low V/f values the direct axis component of the current i_d , becomes negative and the machine experiences under-excitation Fig. 2.6 b).

Using this method, problems are experienced at low speeds, where the frequency has a small value and the resistive term cannot be neglected. To handle this problem, various compensation methods have been proposed, as it can be found in [12, 14-17].

When this control method is applied to PMSM, stability problems will appear because of desynchronization between the rotor speed and the applied frequency [14-18]. This desynchronization between the two frequencies will make the operation impossible.

The classical solution which can be implemented during the manufacturing process is to provide the rotor with damper windings [18]. These damper windings will ensure the synchronization between the two frequencies. However, this solution increases the cost significantly and it is proven to be problematic when it comes to the design of surface mounted PMSM [18].

Different other solutions have been proposed in the literature to deal with this problem by employing a close loop control, such as in [15-17] where the perturbation of the current in the DC link was used to modulate the frequency. The power efficiency was the main objective presented in all three references, with similar approach in [15] and [16], where the voltage was controlled using a search algorithm which ensures a minimum input power to the PMSM. In [17] the objective was to control the voltage in order to obtain unity power factor.

In [14] a voltage control method is used to improve the low speed performance, along with a small signal model which modulates the applied frequency proportional to the input power perturbation.

The cited methods conclude that a better stability is achieved, without the need of damper windings in the rotor, although in [15-17] poor performance was obtained for low speed operation.

A different scalar control method, called I-f control, is presented in [19], for start up without the need of initial rotor position estimation and ultra low speed sensorless control. This method also ensures over-current protection by controlling separately the i_d and i_q currents. The disadvantage presented by this method is the absence of an analytical method to design the I-f controller.

2.5.2 Vector Control

By comparison with the scalar control, vector control allows separate close loop control of both flux and torque [13], by separately controlling the direct and quadrature axis currents i_d and i_q . These two currents are controlled through the voltage v_d and v_q , according to the following equations, derived from (2.18) and (2.19).

$$\frac{di_d}{dt} = -\frac{R_s}{L_d}i_d + \frac{L_q}{L_d}\omega_r i_q + \frac{1}{L_d}v_d \quad (2.27)$$

$$\frac{di_q}{dt} = -\frac{R_s}{L_q}i_q - \frac{L_d}{L_q}\omega_r i_d - \frac{\omega_r}{L_q}\lambda_{pm} - \frac{1}{L_q}v_q \quad (2.28)$$

Vector control can ensure optimum control of the machine under different working conditions, such as: maximum torque per ampere ratio (MTPA), maximum torque per flux ratio, unity power factor.

In the current project the MTPA strategy is implemented. Using this strategy, the control ensures minimum current is used to achieve the required torque, which maximizes the machine efficiency [20]. To achieve MTPA ratio the torque angle θ_T , between the PM flux linkage phasor and the current phasor, has to be maintained at 90° (Fig. 2.8). By doing this the direct axis current i_d , which does not contribute to the production of torque (2.23) is cancelled, and the quadrature axis current i_q becomes equal with the current magnitude ($i_q = \hat{I}_s$).

This situation can be observed in the phasor diagram Fig. 2.7. Here it can be seen that the stator flux linkage is produced by the permanent magnet flux and the flux on the q axis.

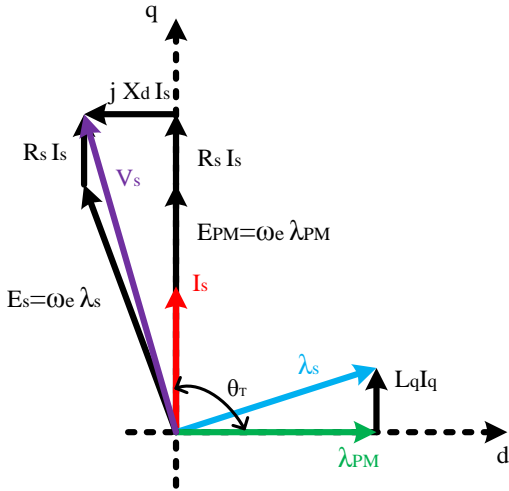


Fig. 2.7. Phasor diagram of vector controlled PMSM for MTPA [13].

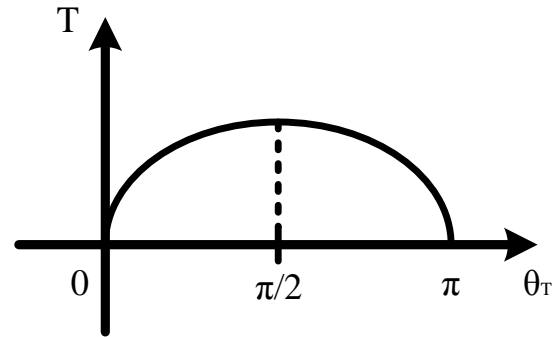


Fig. 2.8. Torque magnitude as a function of the torque angle.

To obtain this behaviour a technique best known as field oriented control (FOC) is used. This technique employs cascaded close loop systems to control the speed and torque, by means of speed controller and current controller. A more in depth description of FOC will be made in the following chapters.

3

Control Description and Implementation

This chapter presents the control strategies that are selected for this project. After the selected scalar and vector control is presented, the implementation method is made. Because scalar and vector control use relatively the same structure, the common components are presented in the vector control part. The last part of the chapter presents the rotor position estimator.

3.1 Scalar Control (I-f Control)

Although V/f control is the most popular scalar control method, it was not selected for this project because of its disadvantages related to PMSM, presented in the previous chapter. Instead, I-f control was preferred because of its advantages, as [19]:

- ability to protect the system by directly controlling the current;
- similar structure and components as FOC;
- the variation in machine parameters has a limited influence over the control;
- capability to start at full load independent of the rotor position;
- in wind turbine applications it is recommended for maintenance situations, when the rotor has to be moved only slightly;

To observe the similarities with FOC, which is presented in more detail in the following subchapter, a block diagram of the scalar control is presented in Fig. 3.3.

The main difference is that a current reference is given directly to the “ q ” axis, eliminating the speed control loop. The “ d ” axis is kept at zero for the same reason as for FOC, to ensure better efficiency for the machine.

If the quadrature axis current is maintained constant during the entire operating procedure, the active power will decrease when the speed reaches nominal value, providing only the necessary power to drive the machine. The rest of the electric power sent to the machine will be transformed to reactive power, which reduces the efficiency and demagnetizes the permanent magnets (Fig. 3.1).

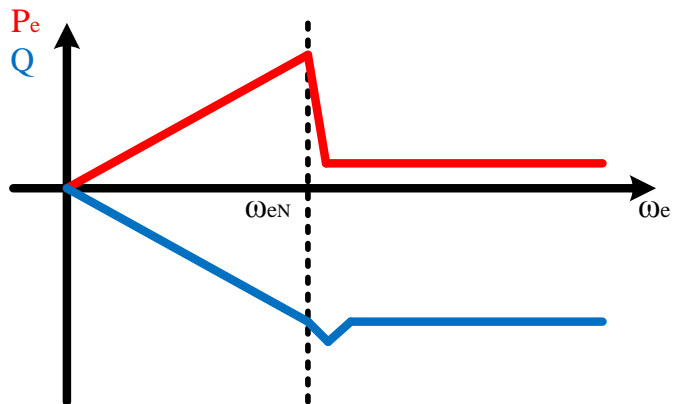


Fig. 3.1. Active and reactive power variation during the starting procedure ($i_q^* = \text{constant}$).

To ensure the best efficiency possible using scalar control, the reference quadrature axis current i_q^* has to be controlled as a function of reference frequency f^* .

If the reference quadrature axis current i_q^* is decreased, after the nominal speed is achieved, the active power is maintained at the same level, while the magnitude of the reactive power is reduced (Fig. 3.2). It has to be noted here that because the imposed rotor position is not equal with the real rotor position, unity power factor cannot be achieved. The quadrature axis current i_q^* has to be maintained at an adequate value, to ensure stable operation.

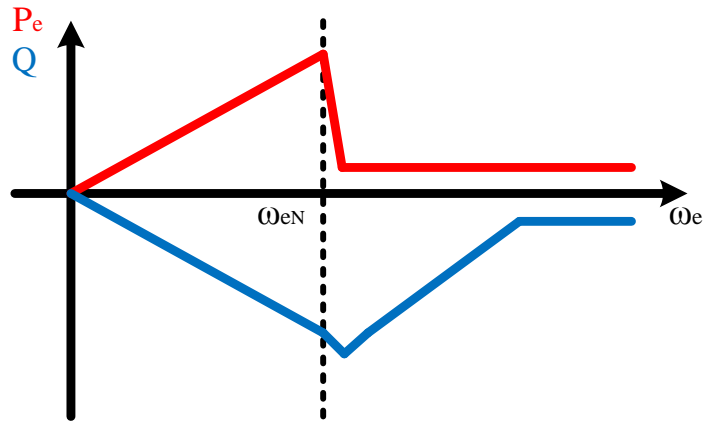


Fig. 3.2. Active and reactive power variation during the starting procedure ($i_q^*(f^*)$).

An important disadvantage, that makes this control unusable for a wind turbine application, must be stated here. Because there is no outer speed loop to provide at any moment the adequate reference quadrature axis current i_q^* , this control cannot be used in all situations required by the system. For example, when the transition from motor to generator is made, the sign of the current reference has to be modified manually by the user, at the same time, or else the control becomes unstable. Also, if a considerable load torque is applied, the current is not able to produce sufficient electromagnetic torque, causing the drive to lose stability.

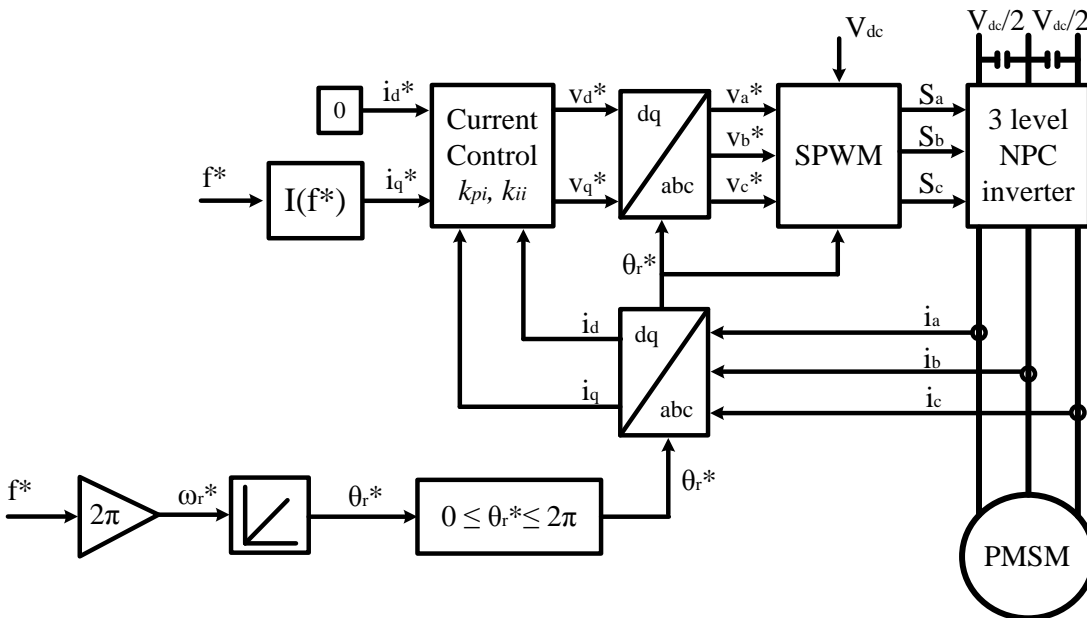


Fig. 3.3. Block diagram of closed loop I-f scalar control [19].

Because of these factors, this control cannot be applied to drive a wind turbine. However, this control is recommended for maintenance situations, when the turbine has to be moved only for short periods of time, at a small speed [19].

This control does not use any position or speed information from an encoder or estimator; instead the position is derived from the frequency command given to the machine. By imposing the position, the reference frequency controls the speed of the machine.

As for FOC two proportional integrators (PI) controllers are used to control the current. Because these two PI controllers have the same structure as for FOC, the implementation method is presented in the following subchapter, where FOC is explained.

The “ dq ” voltage obtained after the PI controllers, which is considered in this case to be the reference voltage, is transferred to “ abc ” reference frame in order to create the command for the switches.

As for vector control, the measured current of the machine is used as a feedback, making it a closed loop control.

3.2 Vector Control (Field Oriented Control)

As stated in the previous chapter the vector control method selected for this project is sensorless field oriented control, working in a MTPA strategy. The implemented block diagram of the control is presented in the following:

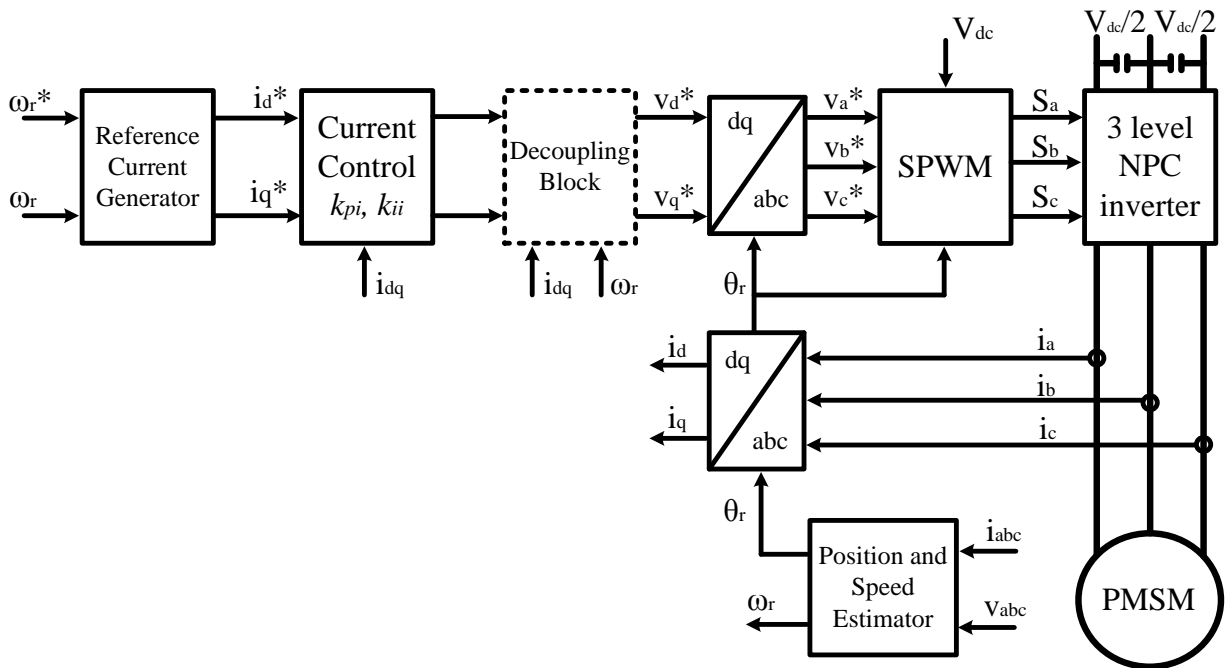


Fig. 3.4. Block diagram of the sensorless FOC.

To ensure safe operation inside the speed range and above it, three types of controllers will be implemented: flux controller, which has as input the flux on the “ d ” axis and produces as output

the reference current on the “ d ” axis, speed controller, which has as input the speed error and produces at the output the reference current on the “ q ” axis, and current controller, which has as input the current error and produces at the output the reference voltage.

The reference current generator block, where the PI controllers for speed and flux are implemented, is presented in more detail in the following figure.

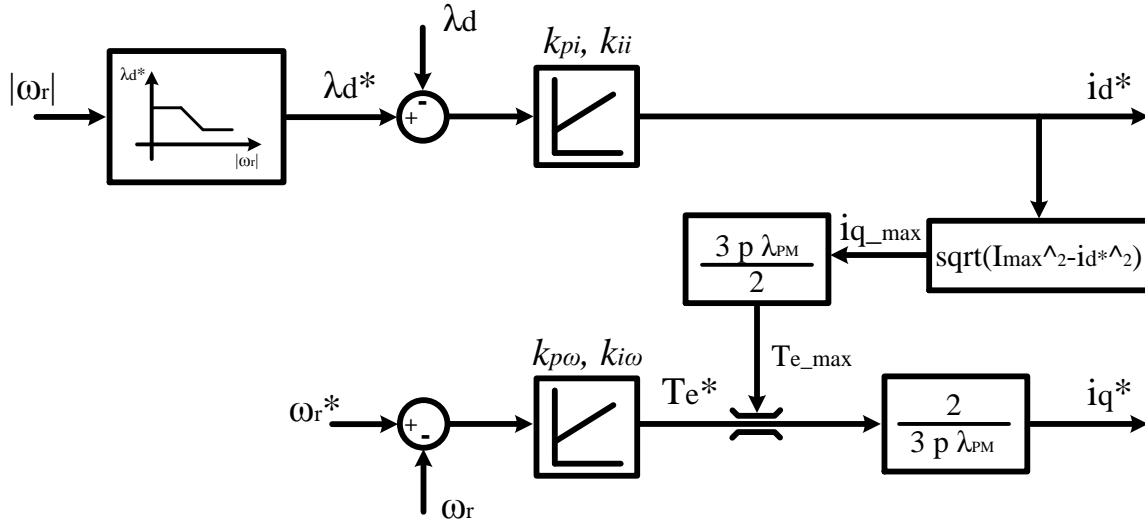


Fig. 3.5. Reference current generator block.

Using field weakening the speed of the machine is increased above nominal speed by decreasing the flux and controlling the torque limits [21].

On the “ d ” axis the current reference is given as a function of the speed magnitude. This behaviour is summarising in the following:

$$\omega_r \leq \omega_{rN} \Rightarrow \lambda_d^* = \lambda_{PM} \Rightarrow i_d^* = 0 \quad (3.1)$$

$$\omega_r > \omega_{rN} \Rightarrow \lambda_d^* = \frac{\omega_{rN}}{\omega_r} \lambda_{PM} \Rightarrow i_d^* = \frac{\lambda_d^* - \lambda_{PM}}{L_d} < 0 \quad (3.2)$$

The direct current has to be reduced ($i_d < 0$) in order to reduce the back-EMF component along the q axis (2.19). Because the direct axis current (i_d) affects the magnetisation it should be limited to a minimum value, at which $\lambda_d^* = 0$.

$$i_{d_min}^* = -\frac{\lambda_{PM}}{L_d} < 0 \quad (3.3)$$

During field weakening control the magnitude of the direct axis current increases ($|i_d| > 0$). This increase has to be taken into consideration in order to limit the current.

When i_d^* current is modified, the maximum $i_{q_max}^*$ current is calculated, in order to limit the torque, using the following equation.

$$i_{q_max}^* = \sqrt{\hat{I}_{max}^2 - i_d^2} \quad (3.4)$$

, where: \hat{I}_{max} - peak value of the maximum allowed current;

Using this approach the control ensures that the machine always runs inside the safety limits.

With the reference currents determined, the error can be calculated. This error is fed to the PI current controllers to provide the voltage command. The decoupling terms, presented in (3.5) and (3.6) are added to the voltage signal, to ensure the decoupling present in the machine equations (2.18) and (2.19).

$$V_{d_decoup} = -\omega_r L_q i_q \quad (3.5)$$

$$V_{q_decoup} = \omega_r (\lambda_{PM} + L_d i_d) \quad (3.6)$$

With the decoupling done, the reference “dq” voltage is transferred to “abc” reference frame, using [4], before the switch modulation is generated.

Because the position and speed estimator represents an important part of the control, it is presented as a separate subchapter, after all FOC components are depicted.

The implementation methods for the current, flux and speed PI controllers are made in the following, starting with the design requirements.

It has to be noted here that in certain situations, the variables will be replaced with their numerical values. These numerical values are presented in Appendix C.

3.2.1 Controller Design Requirements

In the process of designing the current, flux and speed controllers the following design requirements have been taken into consideration:

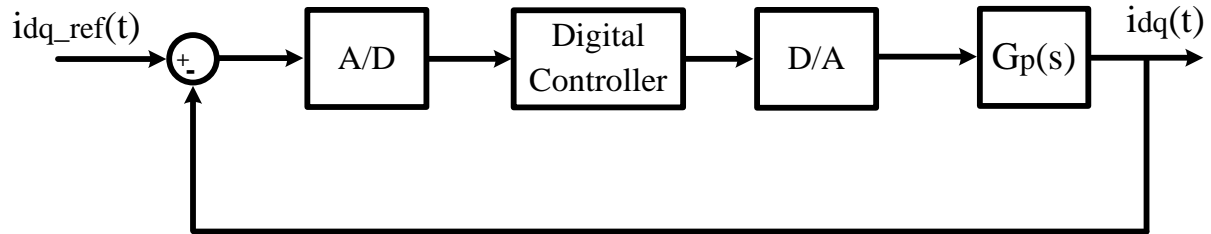
- Steady state error less than 1%;
- Overshoot less than 5%;
- Rise time for the current controller less than 40 sampling periods ($40 \cdot T_s = 10 [ms]$);
- Rise time for the speed controller less than 400 sampling periods ($400 \cdot T_s = 100 [ms]$);
- Bandwidth of the speed controller has to be at least 10 times slower than the bandwidth of the current controller;

With the requirements imposed for all controllers, the implementation process is presented separately in the following.

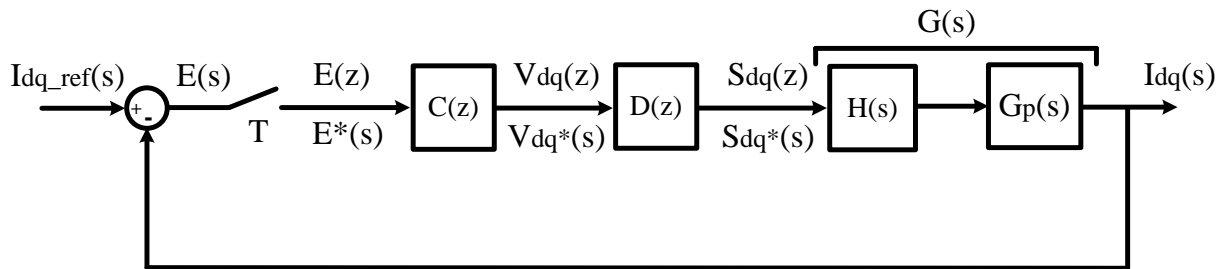
3.2.2 Current Controller

To design the current controllers the machine equations (2.18) and (2.19) must be used to create the plant of the system ($G_p(s)$). The plant constitutes a first order transfer function (3.10), which has the voltage as input, and the current as output.

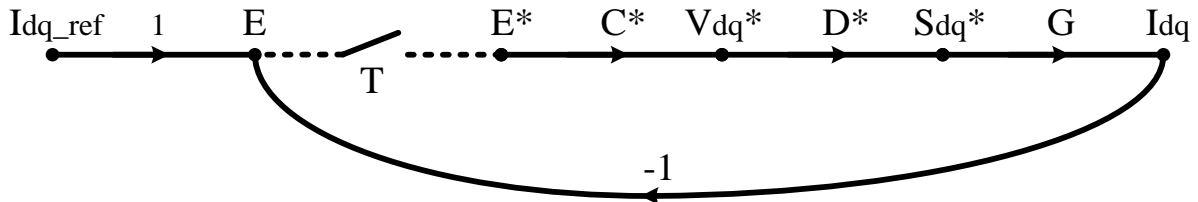
The hardware configuration of the current control is given in Fig. 3.6 a), where the digital controller (PI controller) is implemented, along with the digital to analogue converter (PWM) and the analogue to digital converter (sampler and data hold).



a) Hardware configuration.



b) Block diagram.



c) Flow graph.

Fig. 3.6. Digital control system of the current control loop.

The block diagram, in part b), presents all the signals and transfer functions existent in the current loop. The transfer functions are:

PI controller;

$$C(z) = k_{pi} + \frac{k_{ii}T_s z}{z - 1} \quad (3.7)$$

, where: k_{pi} - current proportional gain;

k_{ii} – current integral gain;

T_s - sampling time [s];

z - discrete time variable;

D/A converter, represents the PWM modulation. To represent the delay introduces by the PWM process, a unity time delay is used.

$$D(z) = \frac{1}{z} \quad (3.8)$$

A/D converter, represents the zero order hold block. This is always required after the ideal sampler [22]. The transfer function of the zero order hold is [22]:

$$H(s) = \frac{1 - e^{-sT_s}}{s} \quad (3.9)$$

Plant, represented by the electrical equations (2.18) and (2.19) of the machine, after the decoupling terms have been eliminated. The remaining components, inductance and resistance, form a first order transfer function.

$$G_p(s) = \frac{1}{L_q \cdot s + R_s} \quad (3.10)$$

A simplification in the system is made by combining the zero order hold block ($H(s)$), with the plant ($G_p(s)$), to create only one transfer function.

$$G(s) = H(s) \cdot G_p(s) = \frac{1 - e^{-sT_s}}{s} \cdot \frac{1}{L_q \cdot s + R_s} = \frac{1 - e^{-sT_s}}{s \cdot (L_q \cdot s + R_s)} \quad (3.11)$$

To determine the system expression, a flow graph (Fig. 3.6 part c)) of the system has to be created. The flow graph is created to represent the sampler influence, using dashed line. The sampler imposes a problem in the system because it does not have a transfer function [22].

Once the flow graph is created, the signals are attributed to the correct position. A note has to be made here regarding the starred variables (E^* , V_{dq}^* , S_{dq}^*) and transfer functions. ($C^*(s)$, $D^*(s)$). These starred variables and transfer functions appear in the system because of the ideal sampler and have a direct link to the z domain [22].

$$E^*(s) = E(z)|_{z=e^{sT}} \quad (3.12)$$

To determine the system output, it has to be expressed like the sampler input, in terms of the system input and sampler output [22].

$$E(s) = I_{dq_ref}(s) - G(s) \cdot D^*(s) \cdot C^*(s) \cdot E^*(s) \quad (3.13)$$

$$I_{dq}(s) = G(s) \cdot D^*(s) \cdot C^*(s) \cdot E^*(s) \quad (3.14)$$

Starring (3.13), and solving for $E^*(s)$ yields:

$$E^*(s) = \frac{I_{dq_ref}^*(s)}{1 + G^*(s) \cdot D^*(s) \cdot C^*(s)} \quad (3.15)$$

Transferring (3.14) in the z domain and replacing $E(z)$ using (3.15) yields:

$$I_{dq}(z) = \frac{G(z) \cdot D(z) \cdot C(z)}{1 + G(z) \cdot D(z) \cdot C(z)} I_{dq_ref}(z) \quad (3.16)$$

Equation (3.16) represents the closed loop transfer function of the current controller. To determine the PI parameters, all transfer functions have to be replaced in (3.16). Because the plant transfer function (3.11) is in the s domain, it has to be transferred to the z domain first.

$$G(s) = A(s) \cdot B^*(s) = \frac{1}{s \cdot (L_q \cdot s + R_s)} \cdot (1 - e^{-sT_s}) \quad (3.17)$$

The transfer function $G(s)$ is separated in two transfer functions, continuous transfer function $A(s)$ and starred transfer function $B^*(s)$, to simplify the procedure. These two transfer functions are then transferred to z domain separately.

$$A(s) = \frac{1}{s \cdot (L_q \cdot s + R_s)} = \frac{1}{R_s} \cdot \frac{\frac{R_s}{L_q}}{s \cdot \left(s + \frac{R_s}{L_q}\right)} \quad (3.18)$$

By defining $\tau = \frac{R_s}{L_q}$, and using the z transform tables,

$$A(z) = \frac{1}{R_s} \cdot Z \left[\frac{\tau}{s \cdot (s + \tau)} \right] = \frac{1}{R_s} \cdot \frac{z(1 - e^{-\tau T_s})}{(z - 1)(z - e^{-\tau T_s})} \quad (3.19)$$

The starred transfer function is transferred to the z domain using (3.12).

$$B(z) = B^*(s)|_{e^{sT_s}=z} = 1 - z^{-1} = \frac{z - 1}{z} \quad (3.20)$$

Replacing (3.19) and (3.20) in (3.17) yields:

$$G(z) = A(z) \cdot B(z) = \frac{1}{R_s} \cdot \frac{z(1 - e^{-\tau T_s})}{(z - 1)(z - e^{-\tau T_s})} \cdot \frac{z - 1}{z} = \frac{1}{R_s} \cdot \frac{1 - e^{-\tau T_s}}{z - e^{-\tau T_s}} = \frac{0.0159}{z - 0.9887} \quad (3.21)$$

A bode diagram is plotted in Fig. 3.7 to present the difference between the continuous plant transfer function (3.10), and the discrete transfer function (3.21). From the response it can be seen that the influence of the zero order hold block (3.9) is very limited.

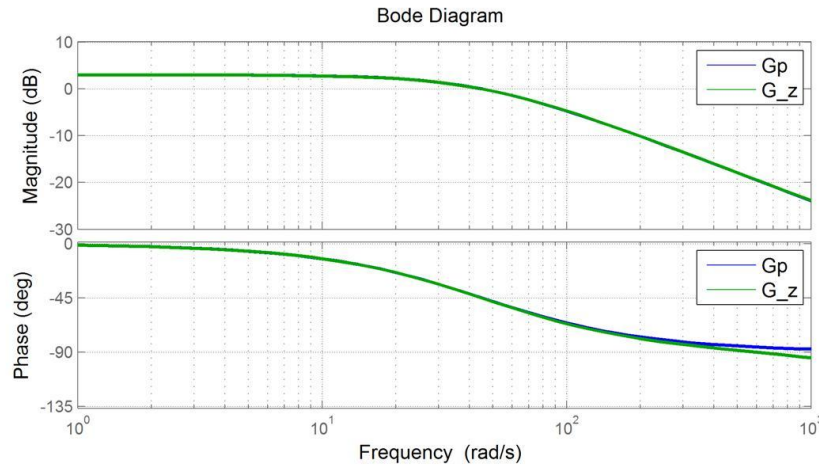


Fig. 3.7. Bode diagram of continuous transfer function (3.10) and discrete transfer function (3.21)

Replacing (3.7), (3.8) and (3.21) in (3.16), yields:

$$H_{cl}(z) = \frac{I_{dq}(z)}{I_{dq_ref}(z)} = \frac{0.0159 \cdot (k_{pi} + k_{ii}T_s)z - 0.0159 \cdot k_{pi}}{z^3 - 1.9887 \cdot z^2 + [0.0159 \cdot (k_{pi} + k_{ii}T_s) + 0.9887]z - 0.0159 \cdot k_{pi}} \quad (3.22)$$

Using all transfer functions obtained, and the design requirements imposed at the beginning, the PI parameters are determined using Matlab's application, Control System Tuning.

The determined PI controller is:

$$C(z) = k_{pi} + \frac{k_{ii}T_s z}{z - 1} = 4.03 + \frac{158 \cdot T_s z}{z - 1} = \frac{4.04 \cdot z - 3.99}{z - 1} \quad (3.23)$$

From

Fig. 3.8 it can be seen that for the selected PI parameters, the steady state error is below 1%, no overshoot appears, the rise time is 8.2 [ms] and the settling time is 18.4 [ms]. All these parameters correspond to the requirements imposed for the controller.

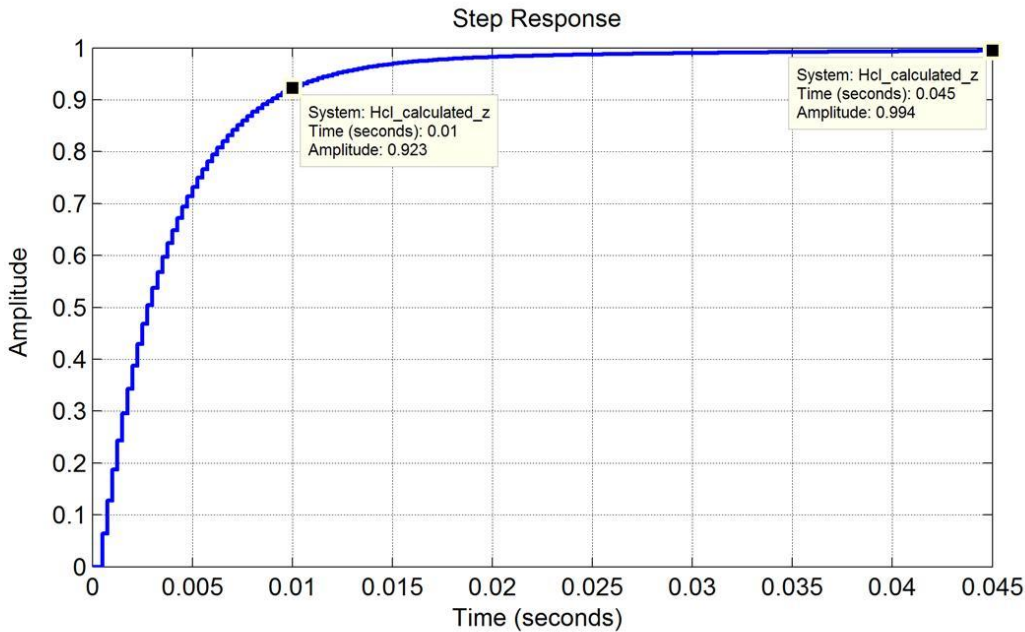


Fig. 3.8. Step response of the current closed loop transfer function (3.22).

From Fig. 3.9 it can be seen that the system is stable because all the poles are situated inside the unity circle. Furthermore, a gain margin of 23.9[dB] and a phase margin of 85.8 [deg] can be observed in the open loop Bode plot, which ensures the loop to be stable.

From the last plot, where the closed loop Bode diagram is presented, the bandwidth of the controller can be obtained. For the current control loop the bandwidth is 277 [rad/sec].

As for the current controller, the machine equation is required to develop the control. In this case the mechanical equation is used (2.24), in which the speed is a function of the torque.

To better understand the structure of the system a block diagram is presented in Fig. 3.10. Here it can be observed that the current control loop is situated inside the speed control loop.

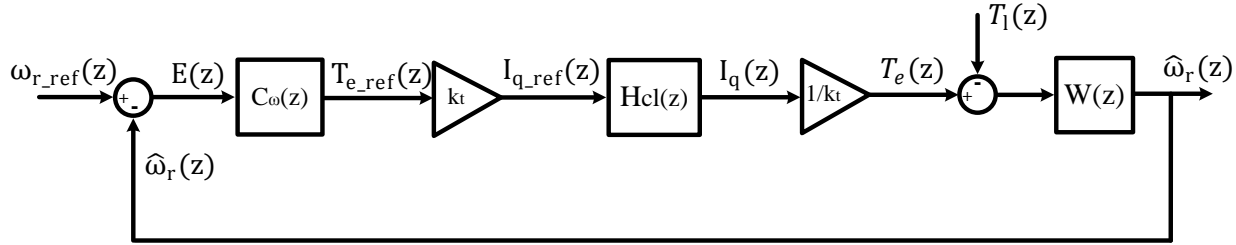


Fig. 3.10. Block diagram of the speed control loop.

The transfer functions are:

PI controller;

$$C_w(z) = k_{pw} + \frac{k_{iw}T_s z}{z - 1} \quad (3.25)$$

, where: k_{pw} - speed proportional gain;

k_{iw} – speed integral gain;

Current loop, represents the close loop transfer function of the current, determined earlier after the PI was selected. The transfer function is presented in (3.22).

Plant, represented by the mechanical equation (2.24) of the machine;

$$W(s) = \frac{1}{J \cdot s + B} \quad (3.26)$$

Because the plant is in s domain, it has to be transferred to z domain before the closed loop transfer function is determined. To diversify the procedure, Matlab is used this time to obtain the discret time transfer function.

$$W(z) = \frac{0.002629}{z - 1} \quad (3.27)$$

As for the current control loop, Matlab's Control System Tuning application was used to determine the PI coefficients.

$$C_w(z) = k_{pw} + \frac{k_{iw}T_s z}{z - 1} = 2.1 + \frac{0.844 \cdot T_s z}{z - 1} = \frac{2.1 \cdot z - 2.1}{z - 1} \quad (3.28)$$

From Fig. 3.11 it can be seen that for the selected PI parameters, the steady state error below 1%, the overshoot is 2.1 [%], the rise time is 86.7 [ms] and the settling time is 144 [ms]. All these parameters correspond to the requirements imposed for the controller.

From Fig. 3.12 it can be seen that the system is stable because all the poles are situated inside the unity circle. Furthermore, a gain margin of 39.2[dB] and a phase margin of 83.6 [deg] can be observed in the open loop Bode plot, which ensures the loop to be stable.

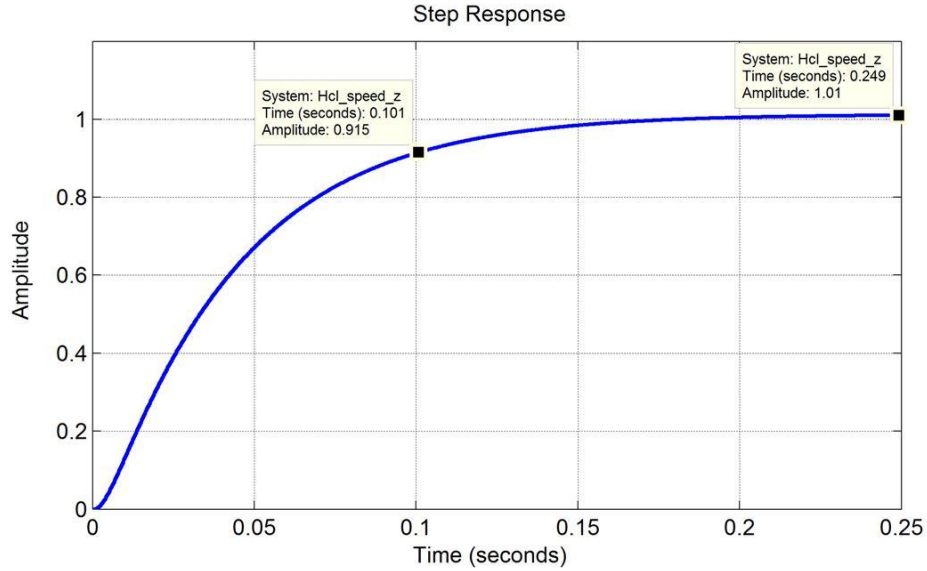


Fig. 3.11. Speed control step response (continuous).

The last plot presents the bandwidth of the controller, which is 24.27 [rad/s]. The ratio between the bandwidths of the two controllers is $277/24.27 = 11.27$. Because the ratio between the two controllers is greater than 10, the last requirement is fulfilled.

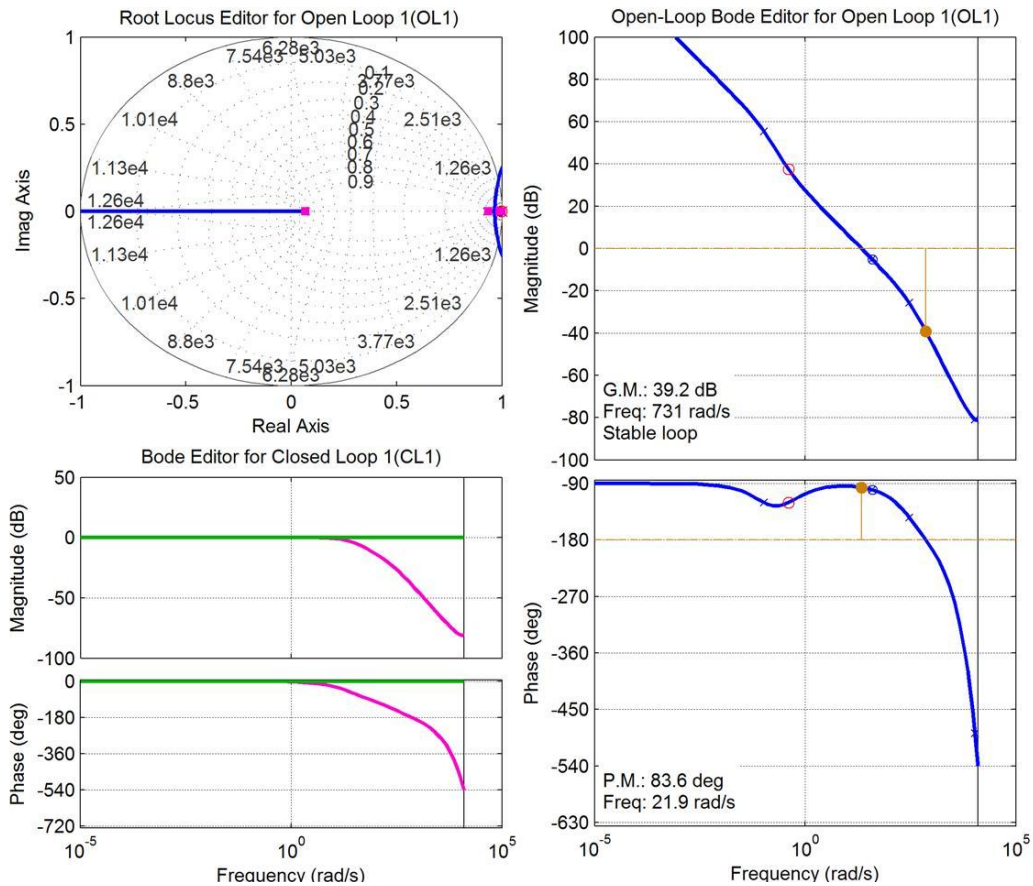


Fig. 3.12. Plots of the speed control system: a) Root locus, b) Open loop Bode and c) Closed loop Bode.

The last components of the control that have to be implemented are the limitations. These limitations maintain the output of the PI controller in a safety region. However, when the output of the PI exits the safety limit, a phenomenon called integrator windup appears [23]. Because this phenomenon can affect the performance of the control, it is analysed in the following.

3.2.5 Anti-Windup

The windup phenomenon appears mainly when a large error is sent to the PI, error which determines the output to vary outside the safety limit. Because the output is limited, the input error cannot be reduced as fast as the controller requires. This behaviour, determines the integrator term to increase significantly in order to correct the input error, phenomenon also called windup [23]. The windup effect has to be eliminated from the system because it produces a large overshoot and a high settling time [23].

In order to deal with this problem a tracking anti-windup solution is used, Fig. 3.13 [23, 24].

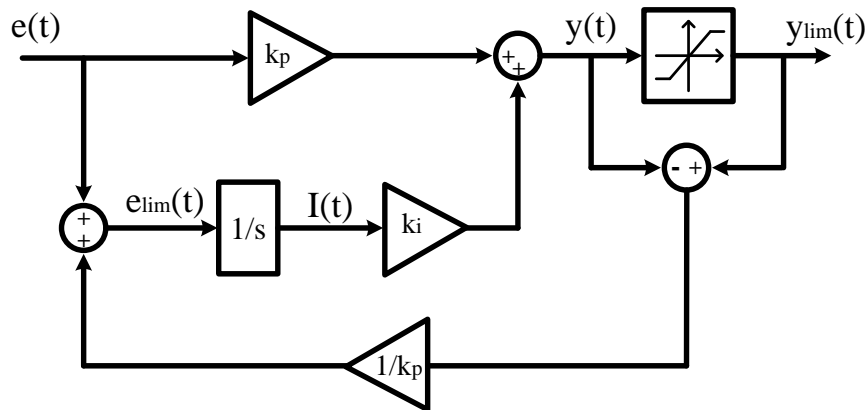


Fig. 3.13. PI controller with anti-windup.

This solution is explained starting with the classical PI controller, without anti-windup, which is created using the following equations:

$$\frac{dI(t)}{dt} = e(t) \quad (3.29)$$

$$y(t) = k_p e(t) + k_i I(t) \quad (3.30)$$

$$y_{lim}(t) = [y(t)]_{min}^{max} \quad (3.31)$$

To avoid integrator windup the input error $e(t)$ has to be reduced for the integrator sum $I(t)$, when the system enters saturation mode. The new input error $e_{lim}(t)$ has to ensure that the output is identical with limited output ($y(t) = y_{lim}(t)$) [24].

$$y_{lim}(t) = k_p e_{lim}(t) + k_i I(t) \quad (3.32)$$

From (3.30) and (3.32) the new error can be determined.

$$e_{lim}(t) = e(t) + \frac{1}{k_p} [y_{lim}(t) - y(t)] \quad (3.33)$$

Using the new error to determine the integrator sum, the new controller equations can be written.

$$\frac{dI(t)}{dt} = e_{lim}(t) \quad (3.34)$$

$$y(t) = k_p e(t) + k_i I(t) \quad (3.35)$$

$$y_{lim}(t) = [y(t)]_{min}^{max} \quad (3.36)$$

From (3.38) it can be observed that the new error is used only to calculate the integrator sum, the proportional part of the control uses the original error $e(t)$.

Once the PI controllers are implemented with anti-windup, the only remaining problem is to determine the rotor position. Because a sensorless method was selected to determine the rotor position, this method will be presented in the following.

3.3 Rotor Position Estimation

The method used to determine the rotor position and speed is generally known as the back-EMF method [11, 25, 26]. In order to estimate the position, the mathematical model of the machine, in dq reference frame is used (2.18) and (2.19).

The two equations can be written in vectorial form as:

$$\bar{v}_{dq} = R\bar{i}_{dq} + \frac{d\bar{\lambda}_{dq}}{dt} + j\omega_r \bar{\lambda}_{dq} \quad (3.37)$$

$$\bar{\lambda}_{dq} = L_d \bar{i}_d + \lambda_{mpm} + jL_q \bar{i}_q \quad (3.38)$$

The method requires that the equations should be transferred to $\alpha\beta$ reference frame:

$$\bar{v}_{\alpha\beta} = R\bar{i}_{\alpha\beta} + \frac{d\bar{\lambda}_{\alpha\beta}}{dt} \quad (3.39)$$

$$\bar{\lambda}_{\alpha\beta} = (L_d \bar{i}_d + \lambda_{mpm} + jL_q \bar{i}_q) e^{j\theta_r} \quad (3.40)$$

Since the position term (θ_r) appears only in the flux linkage equation (3.40), this will be the equation from where the position will be computed. An important transformation must be made in order to extract the position.

$$\bar{\lambda}_{\alpha\beta} = (L_d \bar{i}_d + \lambda_{mpm} - L_q \bar{i}_d + L_q \bar{i}_d + jL_q \bar{i}_q) e^{j\theta_r} \quad (3.41)$$

In order to better understand the meaning of each term in the equation it is written in the following form:

$$\bar{\lambda}_{\alpha\beta} = L_q \bar{i}_{\alpha\beta} + [(L_d - L_q) \bar{i}_d + \lambda_{mpm}] e^{j\theta_r} \quad (3.42)$$

From (3.42) it can be seen that the direct current component i_d affects only the amplitude, of the vector that contains the rotor position information. Knowing this, the rotor position (angle), can be expressed.

$$\angle[(L_d - L_q)i_d + \lambda_{mpm}]e^{j\theta_r} = \angle e^{j\theta_r} = \angle(\bar{\lambda}_{\alpha\beta} - L_q\bar{i}_{\alpha\beta}) \quad (3.43)$$

The estimated rotor position can be obtained using the following equation:

$$\hat{\theta}_r = \tan^{-1} \frac{\lambda_\beta - L_q i_\beta}{\lambda_\alpha - L_q i_\alpha}, \quad \text{for} \quad \begin{cases} \lambda_\alpha = \int (v_\alpha - R i_\alpha) dt \\ \lambda_\beta = \int (v_\beta - R i_\beta) dt \end{cases} \quad (3.44)$$

Some problems must be considered when using this method, as: integration requires an initial value and a small drift in current value will cause increasing error after integration [21]. Because these influences can affect the computation, rendering the method unviable, an adaptive correction has to be implemented.

The correction method that was selected to be implemented in this project uses two elements: a drift compensation loop and a phase lock loop (PLL) [21, 26]. In the following, both methods will be explained along with the implementation method.

➤ Drift Compensation Loop

This subsystem is implemented to eliminate the error before integration, by comparing two flux values in stationary reference frame ($\alpha\beta$). The first $\alpha\beta$ flux value is obtained using (3.44). The second flux value is determined in dq reference frame, using (2.20) and (2.21), result which is transferred to $\alpha\beta$ reference frame.

The difference between the two fluxes represents the error sent to the PI controller. As output, the PI controller produces a voltage component V_{comp} , which is used to eliminate the drift.

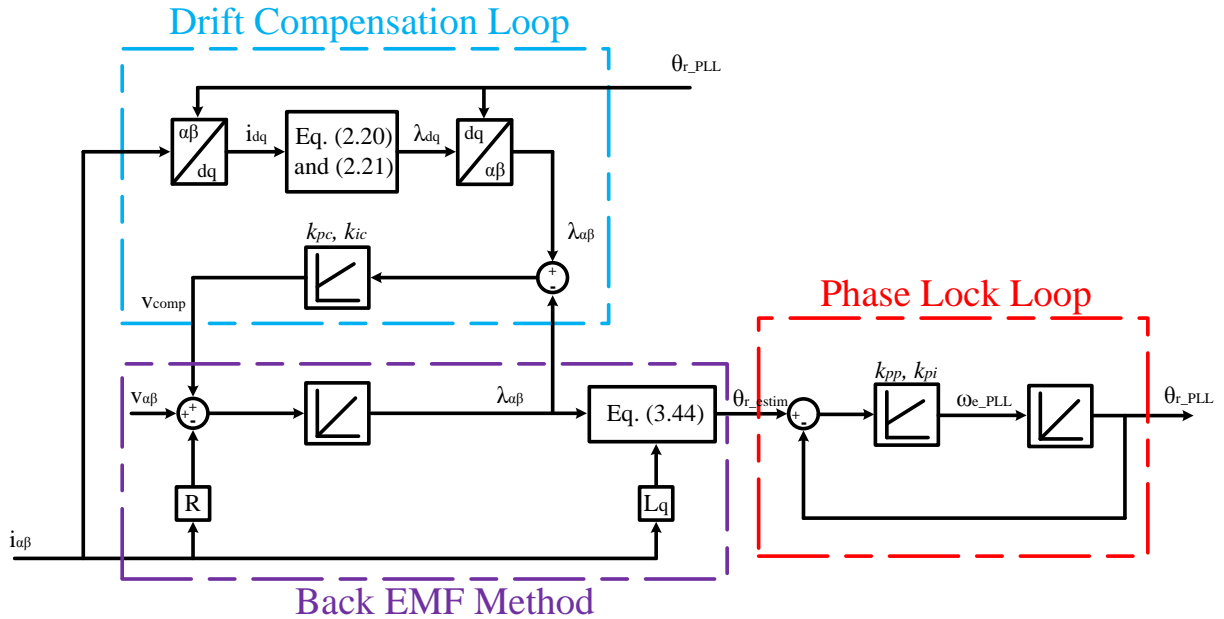


Fig. 3.14. Block diagram of back-EMF method along with drift compensation and PLL [21].

➤ Phase Lock Loop

The PLL implemented in the system is placed after the back-EMF method. It is used to eliminate the error in the estimated position, by taking as an input the estimated position (3.44) and comparing it to the output of the PLL, which will represent the actual estimated rotor position.

The main disadvantage of the back-EMF method comes from its name. The method is unable to provide the correct information at very low speeds. This is because the back-EMF term contains the speed variable. When the speed is close to zero, the back-EMF term is very small, and the estimated position is not precisely estimated.

Because of this problem, during the start up procedure, the rotor will produce an initial vibration, until the alignment is achieved, followed by a smooth transition, until the reference speed is reached. This problem was observed in simulations and in laboratory experiments.

4 Simulations

The model created, along with the control, is tested during a series of simulations to observe the performance. The simulation conditions are selected considering the objectives imposed in the first chapter. This chapter will present the result of each simulation, along with necessary explanation. All simulation are made using Matlab Simulink. To get familiarized with the Matlab Simulink model, an overview is presented at the beginning.

4.1 Model Overview

As it could be seen in Fig. 4.1 the model consists out of three main blocks: permanent magnet synchronous machine, field oriented control, and speed and position estimator.

Besides the main blocks, three selectors are employed to allow the user a fast change between different load types and different working conditions.

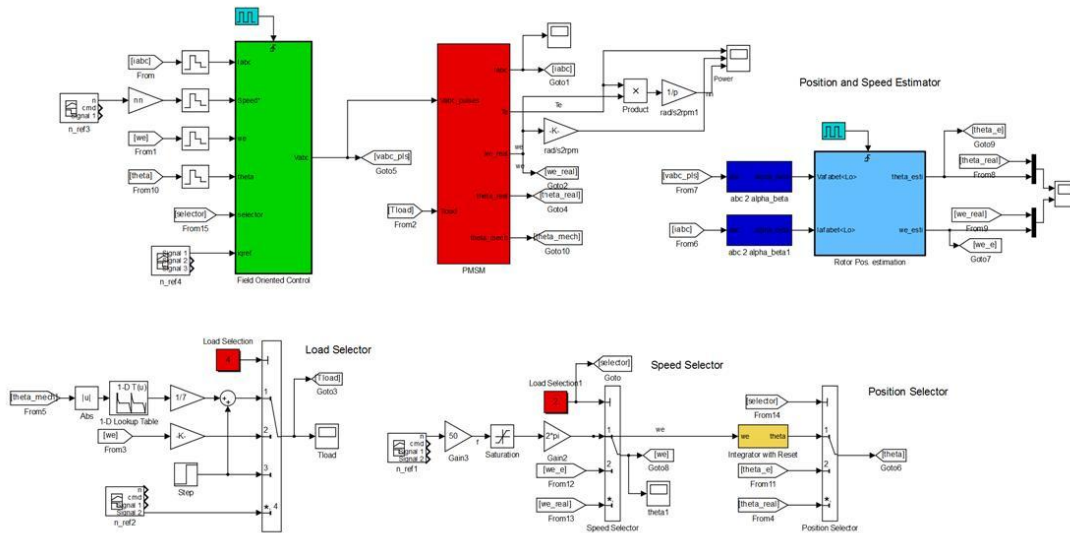


Fig. 4.1. Matlab Simulink model of the system.

A more complex model, containing more components, like the three level NPC converter, AC voltage source, diode bridge rectifier and SPWM, was also created. Because both models provide similar results, the simplified model is used for the report.

Using this model, a series of simulations are made. These simulations are developed to test the control for all the requirements imposed in the objectives.

4.2 Scalar Control Simulations

According to the description provided in previous chapters, scalar control is unable to operate in all situations required by the objectives. Because of this factor, and because the dynamic performance is reduced, compared to vector control, this is considered to be an alternative control strategy, not the main control. Only two simulations are made using scalar control, to verify how the control reacts during speed variation and during load torque disturbance.

4.2.1 Speed reference variation

The first simulation is made to test how the control behaves when the reference speed is modified. From Fig. 4.2, it can be seen that during the starting procedure small oscillations in speed appear. These oscillations appear because the position imposed from the reference frequency is not aligned with the rotor position.

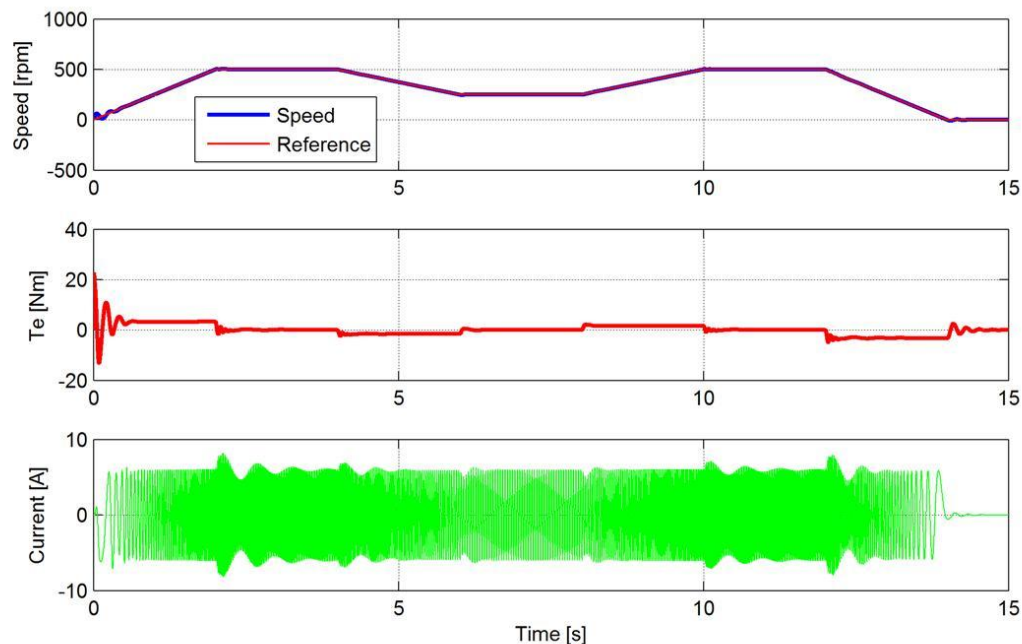


Fig. 4.2. Result of speed reference variation using scalar control.

As it could be seen from Fig. 4.2 and Fig. 4.3, the current is sinusoidal with a constant magnitude during the entire simulation time. Small changes in current magnitude appear only during the transient regime.

For a better view of voltage and current in steady state, Fig. 4.3 presents a closer perspective. Here we can observe that the current and the voltage are sinusoidal, with a phase shift of approximately 90° .

The large phase shift, which determines a small power factor, appears because the simulation is done without adding a load to the system. Without a load, the active power required by the machine is very small. Because the control maintains the current at a high value, even during no

load situation, a significant amount of apparent power is provided at the terminals, power which becomes reactive power, as it was explained in Scalar Control (I-f Control).

This large phase shift, combined with the current magnitude, determines an inefficient operation.

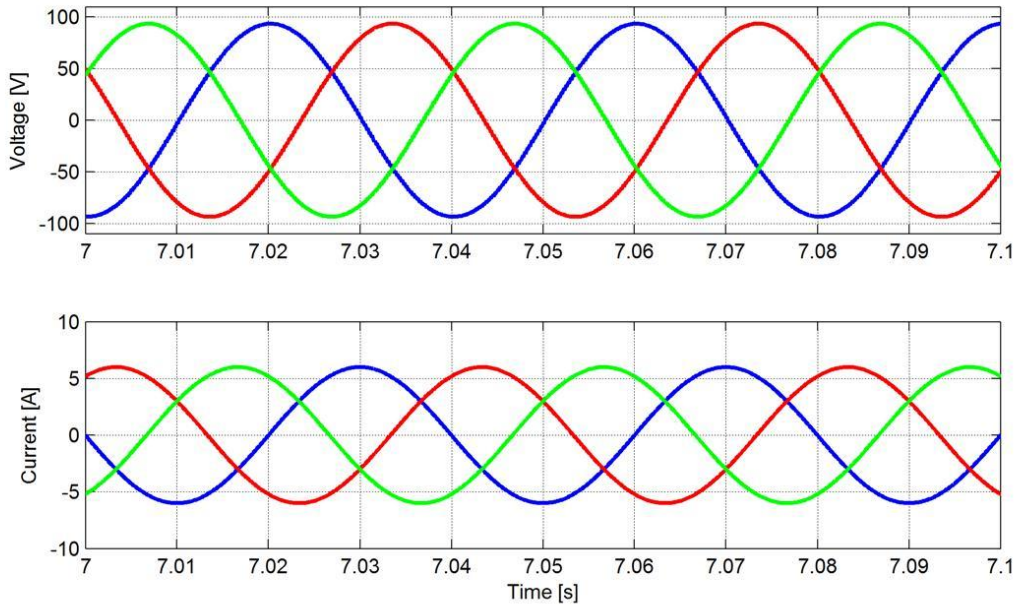


Fig. 4.3. Voltage and current in steady state situation.

To increase the efficiency, a modified method is proposed in Scalar Control (I-f Control) subchapter. This method requires that the reference quadrature axis current (i_q^*) is modified as a function of frequency, according to Fig. 4.4.

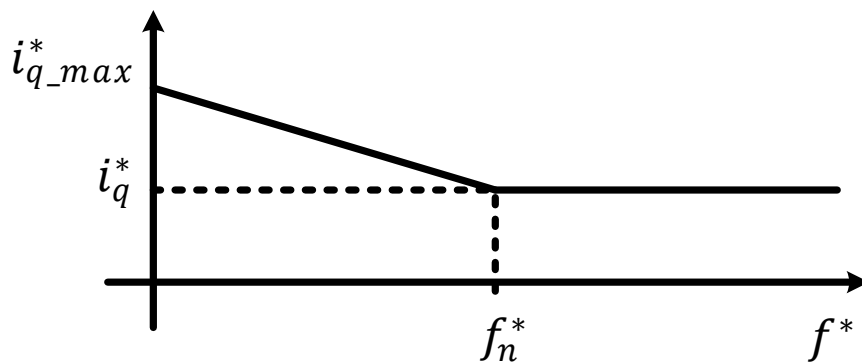


Fig. 4.4. Reference quadrature axis current (i_q^*) as a function of frequency.

The maximum current is applied only at the beginning, to provide sufficient torque during the starting procedure. The reference quadrature axis current (i_q^*) is reduced to 50% of the maximum value ($i_{q_max}^*$), when the frequency reaches nominal value.

The result of the simulation, presented in Fig. 4.5, shows that speed and the torque characteristics are not affected by this modification.

An important difference can be observed in the current waveform. In this situation the current has smaller amplitude, when the system enters steady state. However, from the result it can be seen that the oscillations have increased.

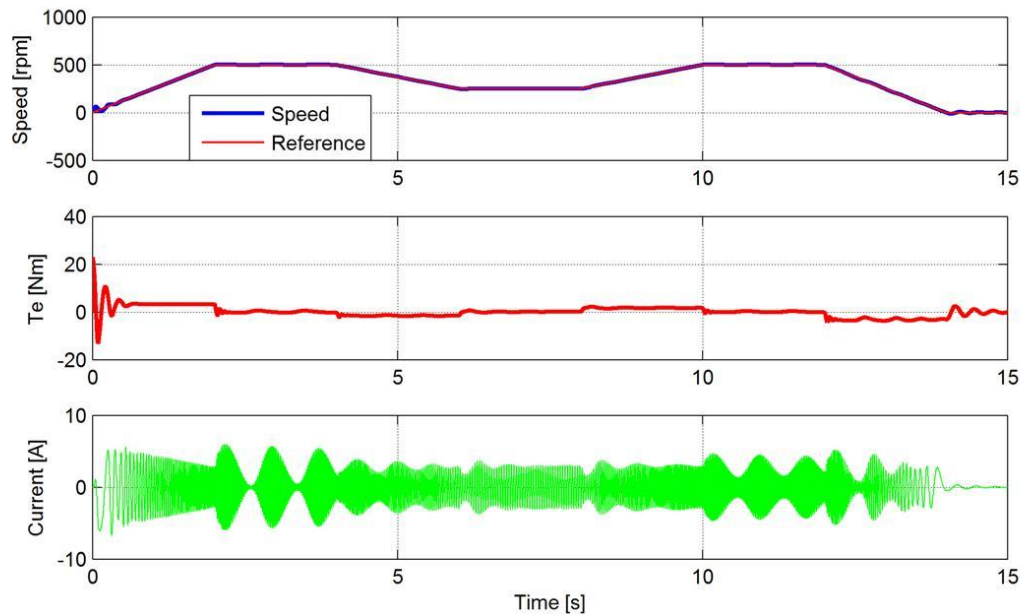


Fig. 4.5. Speed reference variation using scalar control (modified version).

To analyze the phenomenon, several simulations are done at different reference currents. From the results it was observed that the oscillations increase as the current is decreased. The reference current has to be maintained above a minimum value, to ensure system stability.

The disadvantage is that the minimum current value cannot be determined analytically because it is affected by numerous other parameters as, load torque, reference speed variation and PI parameters.

4.2.2 Load torque variation

The second simulation is made to determine how the control behaves when an external mechanical load is applied.

From Fig. 4.6, it can be seen that the control is able to maintain the speed within $\pm 2.4\%$ of the nominal speed.

This fast response is due to the fact that the electromagnetic torque has a fast response time, to counteract the load torque applied at the shaft.

From both the current and electromagnetic torque waveform, it can be seen that oscillations appear in the system before it enters steady state. These oscillations are caused by the fast response of the PI controllers.

As for the previous situation, the current and voltage variation is sinusoidal.

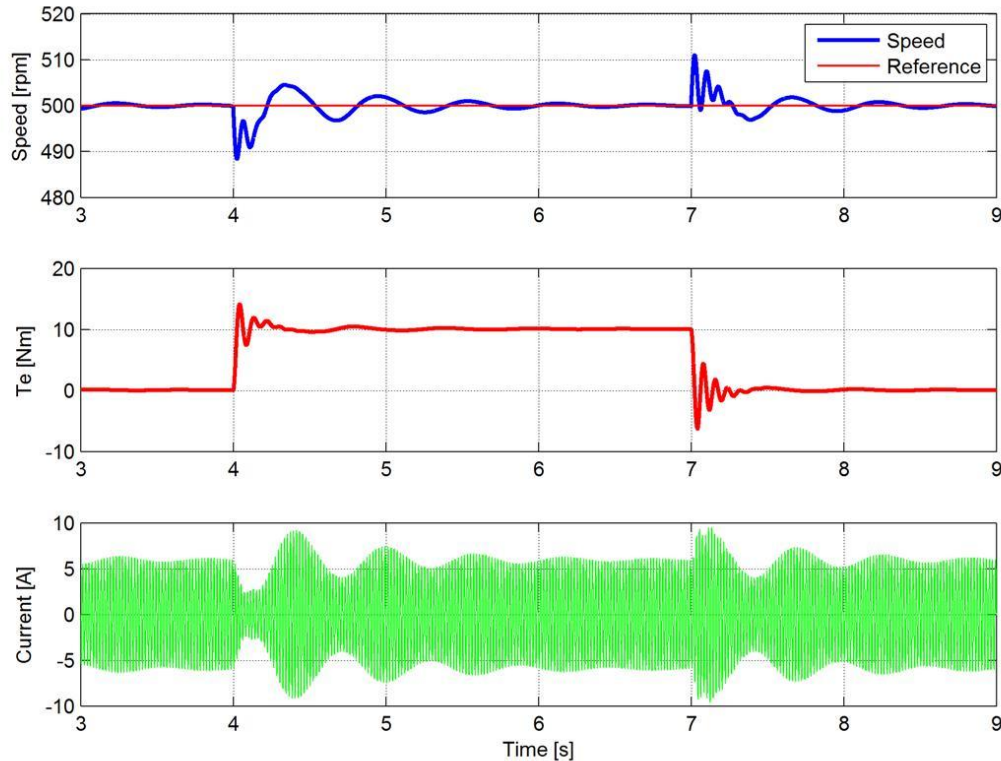


Fig. 4.6. Result of load torque variation using scalar control.

From the simulation, an increase in power factor is observed, when the load torque is applied. This is due to the fact that a higher amount of apparent power, supplied at the machine terminals, is used as active power.

4.3 Vector Control Simulations

Because this control is considered to be the primary control strategy for the drive, it will be tested in five different situations, according to the objectives.

The first two tests are made in similar conditions as the test made for scalar control. The difference is that for vector control, the reference speed is given using the step command, not the ramp command.

4.3.1 Speed reference variation

As for the previous case, the main objective of this simulation is to observe how the control behaves when the reference speed is modified.

Because the control is implemented using speed and position estimator, the performance of the estimator is also of main interest.

From Fig. 4.7, it can be seen that the control is able to provide a fast response, when the reference speed is modified.

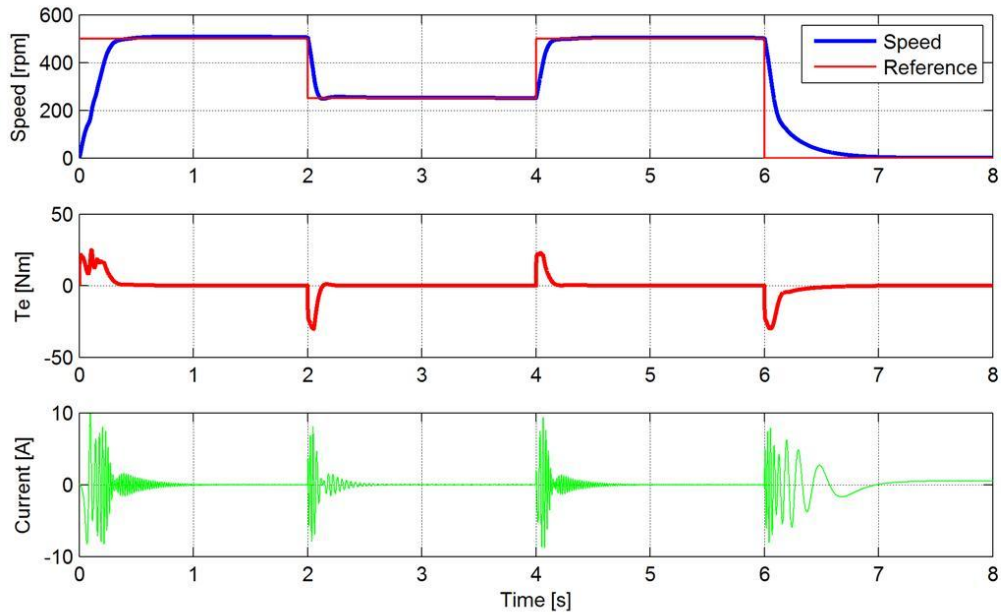


Fig. 4.7. Result of speed reference variation using vector control.

Compared to scalar control, a higher efficiency is achieved, because the current reference is provided by the outer speed loop.

From Fig. 4.8, it can be seen that the speed and position estimator is able to produce an accurate estimation, in less than a second. The fast response of the estimator enables the control to start the machine without the use of an encoder.

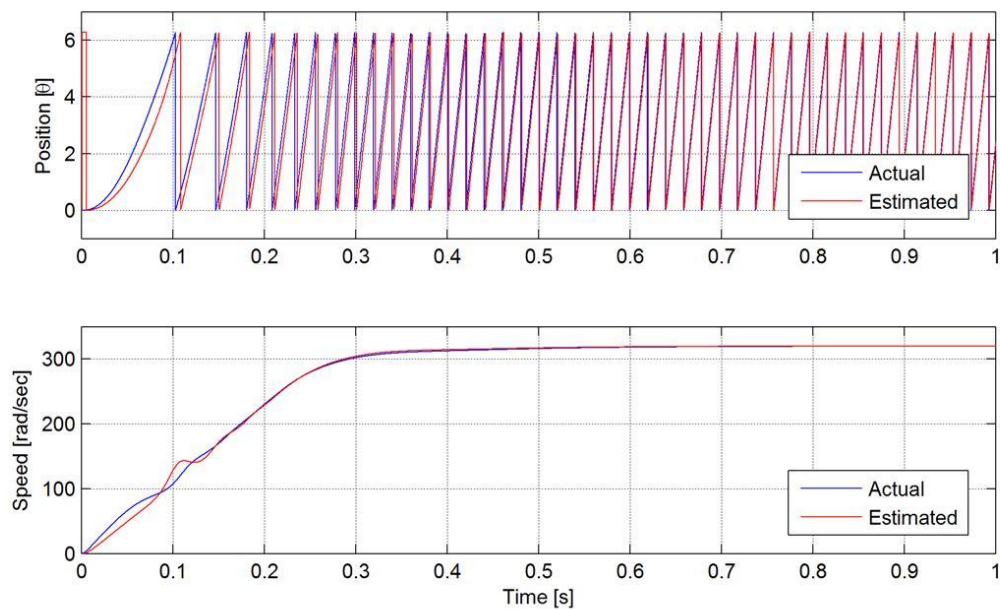


Fig. 4.8. Comparison between actual and estimated position, and speed.

4.3.2 Load torque variation

In the second simulation, the capability of the control to react in case of a load torque disturbance is tested. From the results presented in Fig. 4.9, it can be seen that the control manages to withstand the torque step. The speed of the machine decreases with approximately 18% of the nominal speed, when the load torque is applied. The maximum speed achieved, when the load torque is removed, is 12.5% the nominal speed.

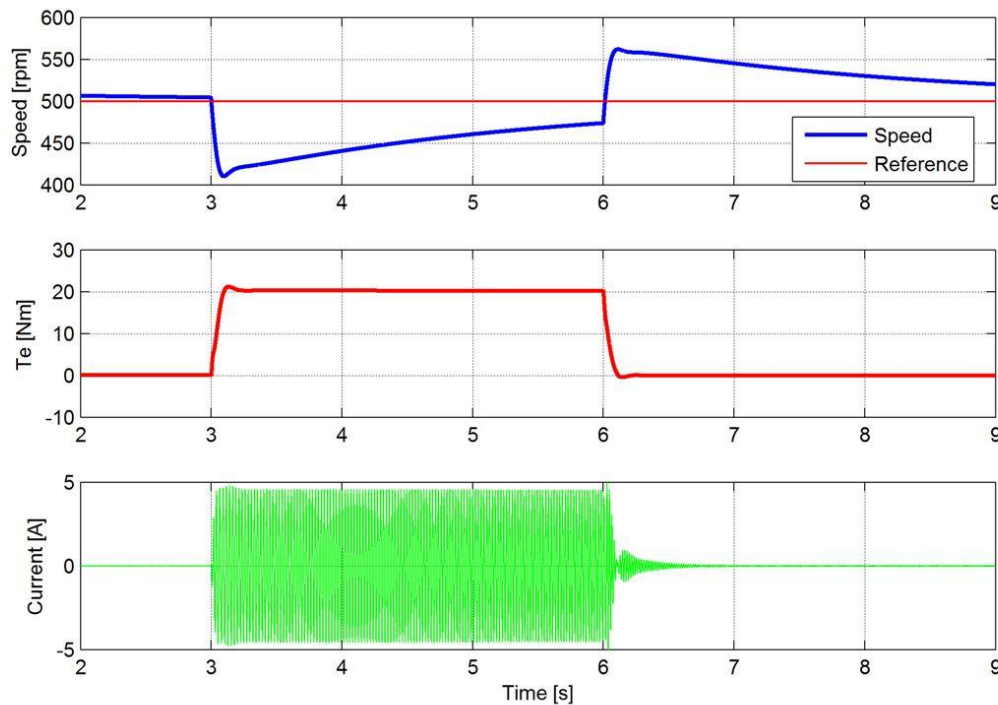


Fig. 4.9. Result of load torque variation using vector control.

From the current waveform it can be seen that compared to scalar control, no oscillations appear. The current is maintained inside the safety boundaries during the entire period.

4.3.3 Transition from motor to generator

As stated in the Converter and Control for DeepWind Programme subchapter, the Darreius wind turbine is unable to start without the help of the machine. Because of this factor, the machine has to be controlled in motor mode, until the required speed is achieved. Once the turbine is able to capture the wind power, the control must ensure a safe transition from motor to generator.

In order to test the transition from motor to generator and back, a load torque is applied at the shaft, having the same direction as the speed (Fig. 4.10).

From Fig. 4.11, it can be seen that the simulation result is very similar with the previous case. When the load torque, having the same direction as the speed, is applied, the speed of the drive increases too approximately 19% of the nominal speed. To maintain stability, the control counteracts the load torque by changing the direction of the electromagnetic torque.

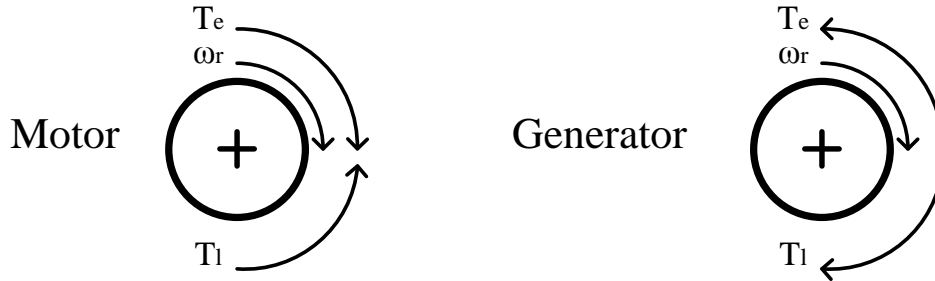


Fig. 4.10. Speed and torque direction for motor and generator mode.

Once the direction of the electromagnetic torque is opposite to the speed direction the machine enters generator mode. This operation mode continues until the load torque is removed.

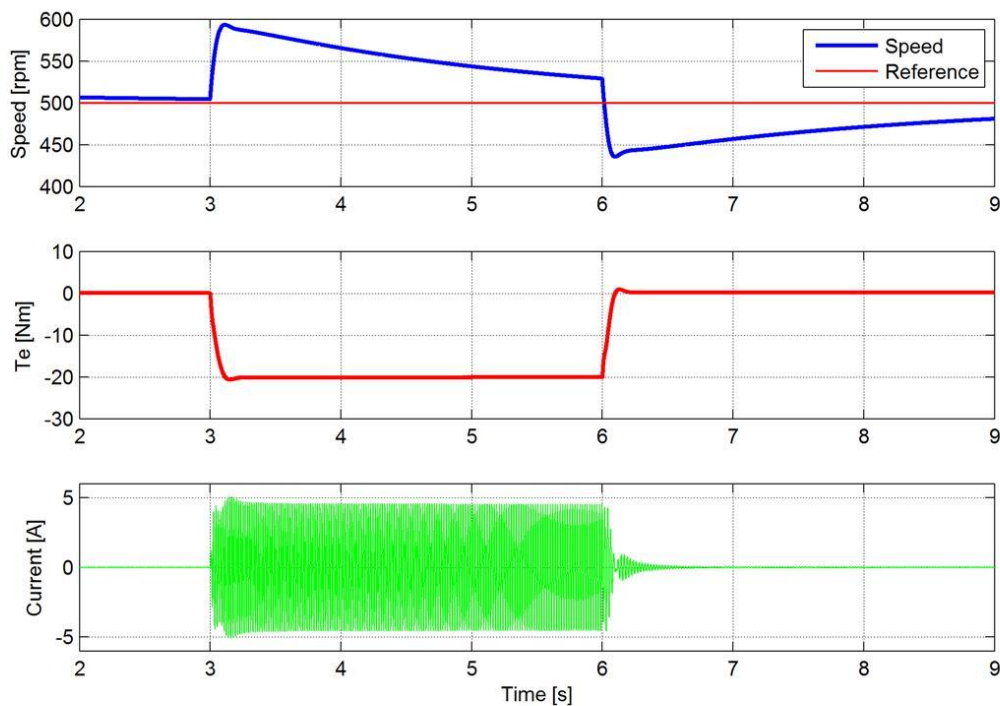


Fig. 4.11. Result of transition from motor to generator and back.

As it can be seen from the current waveform, the amplitude is maintained constant, inside the safety boundaries, during the entire procedure.

4.3.4 Emergency breaking

As it was explained in the Converter and Control for DeepWind Programme subchapter, mechanical breaks cannot be fitted to the turbine. The control must be capable to stop the turbine in case of an emergency, as high wind or high waves.

To emulate such a situation, the load torque was maintained constant during the breaking procedure, while the speed was brought down to zero in two seconds.

The speed was decreased using a ramp variation because of the following reasons:

- In case of a large structure, as the wind turbine is presumed to be, the transition from nominal to zero speed has to be smooth;
- To observe how the control behaves when the reference is given as a ramp command.

From the result presented in Fig. 4.12, it can be seen that between the reference and the actual speed there is a constant steady state error. This error is removed after the reference speed reaches zero.

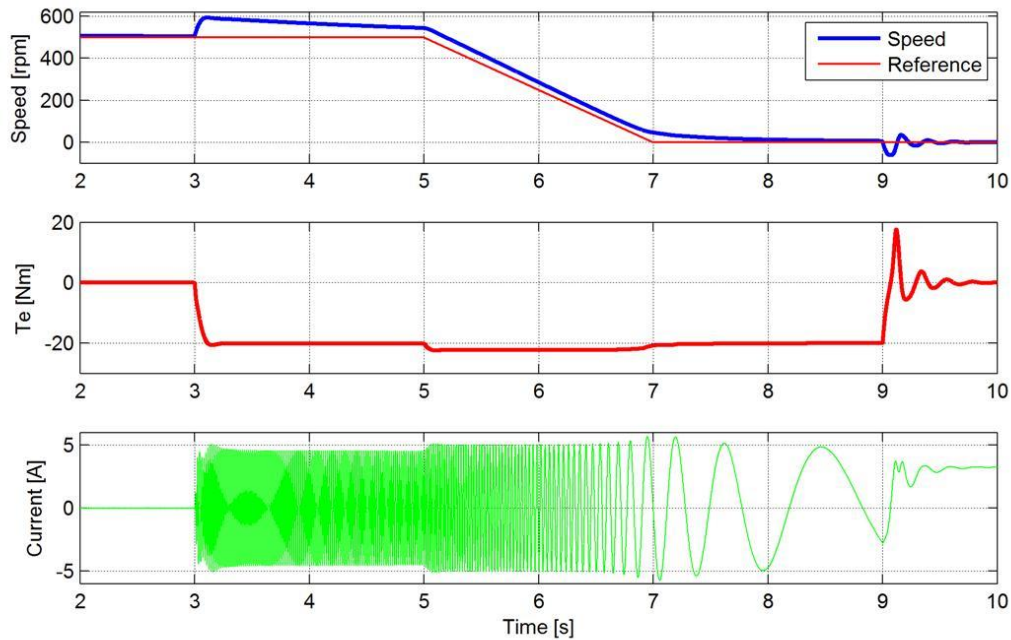


Fig. 4.12. Result of emergency breaking.

When the speed reaches zero, the estimator cannot provide the correct position and speed information, as it can be seen in Fig. 4.13. Because the simulation uses a simplified model, the speed of the machine is maintained constant at zero, while a load torque is applied, even though the estimated position is not similar with the actual position.

In a practical experiment, there are many other parameters that influence the control, which have to be considered, in order to ensure stability. The discussion regarding stability at very low speeds, in a practical system, is presented in Laboratory Experiments.

After the speed has reached zero and the load torque is removed, the control has to reduce the electromagnetic torque, in order for the speed to remain constant at zero.

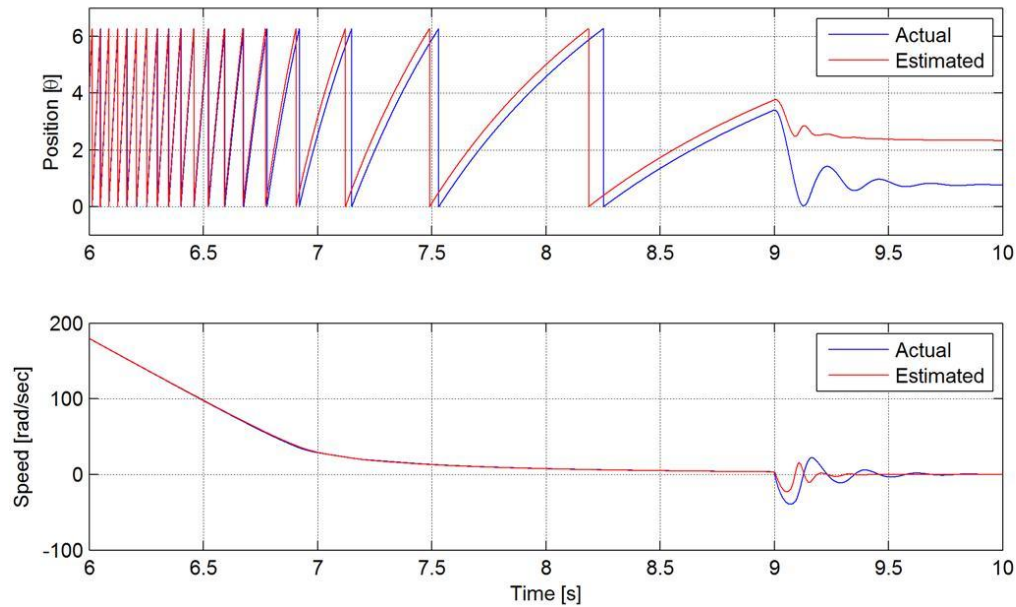


Fig. 4.13. Comparison between actual and estimated position, and speed, for the low speed range.

4.3.5 Holding the machine at zero speed

The last test required by the objectives is to maintain the speed of the machine at zero, while a load torque is applied.

Because the speed and position estimator cannot provide information about the position when the speed is zero, the control has difficulties to maintain the speed in a small interval, when a load torque is applied.

The control can react to torque disturbance, only after the estimator provides the proper position. Until the position is determined, the speed of the machine can increase to a high value.

From the simulation result (Fig. 4.14), it can be seen that the speed reaches a maximum value of 30% of the nominal speed.

After approximately half a second, the position estimator is able to determine the actual position (Fig. 4.15), causing the control to ensure a smooth transition to zero speed.

When the load torque is removed, the control produces an oscillatory response, until the speed becomes zero.

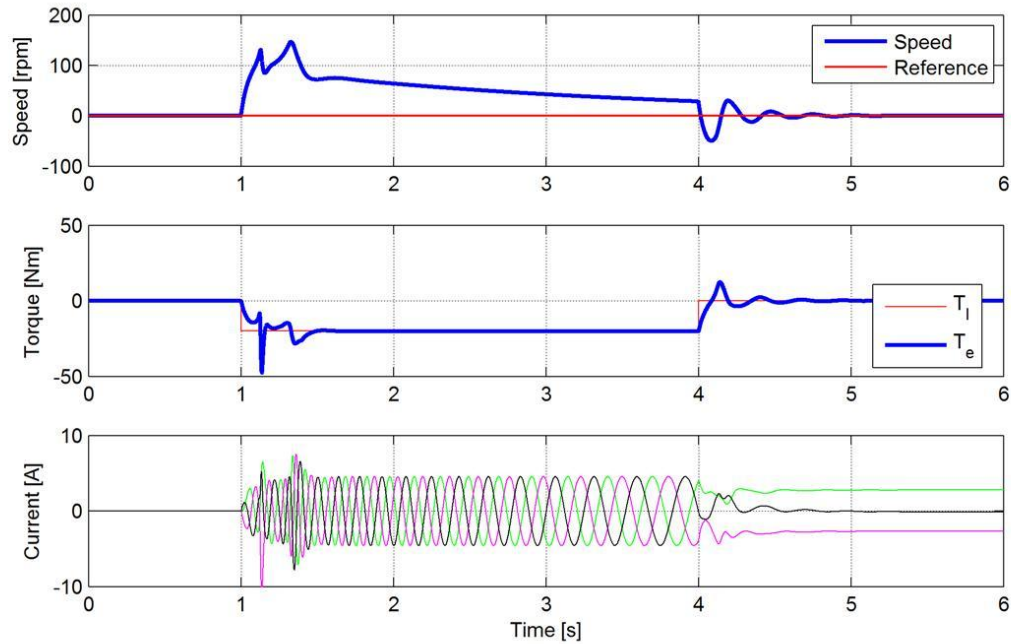


Fig. 4.14. Result of holding the machine at zero speed.

As for the previous case, the simplified model cannot recreate very accurately the practical situation. To have a better understanding of how the real system behaves during this experiment, please refer to Laboratory Experiments.

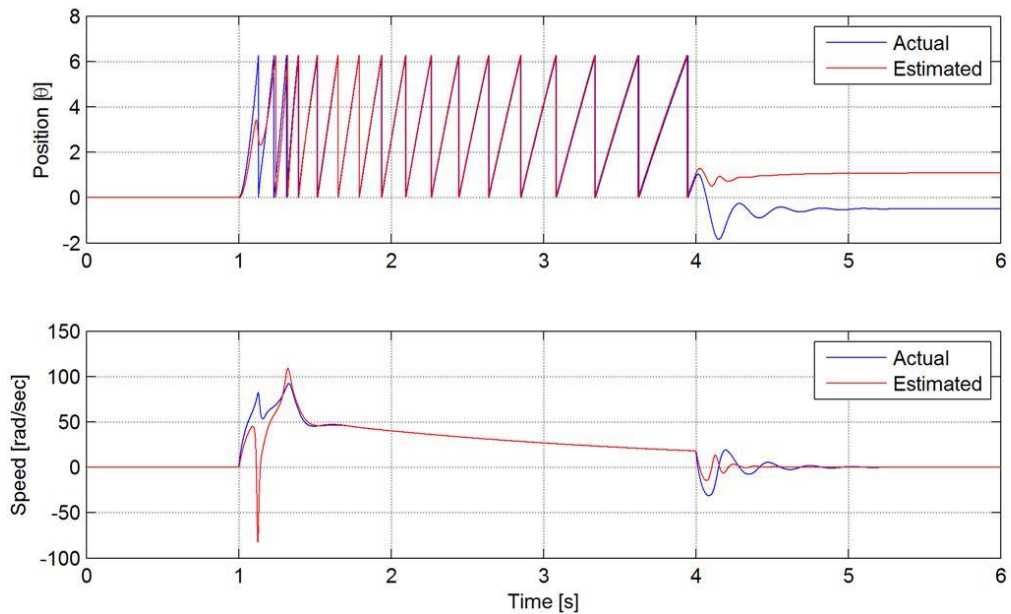


Fig. 4.15. Comparison between actual and estimated position, and speed, during holding the machine.

5

Hardware Design of Converter

In this chapter the design and the main circuits of the three level NPC converter are presented. Because the design was not an objective for this project, only the main parts of the converter will be presented here, with sufficient explanation in order for the reader to understand the hardware used. For more information about the design and the components, please refer to [7].

5.1 General Structure

Based on [7] and Fig. 5.1 it can be seen that the design is made in such a way as to separate the hardware into two isolated regions: the power side and the control side.

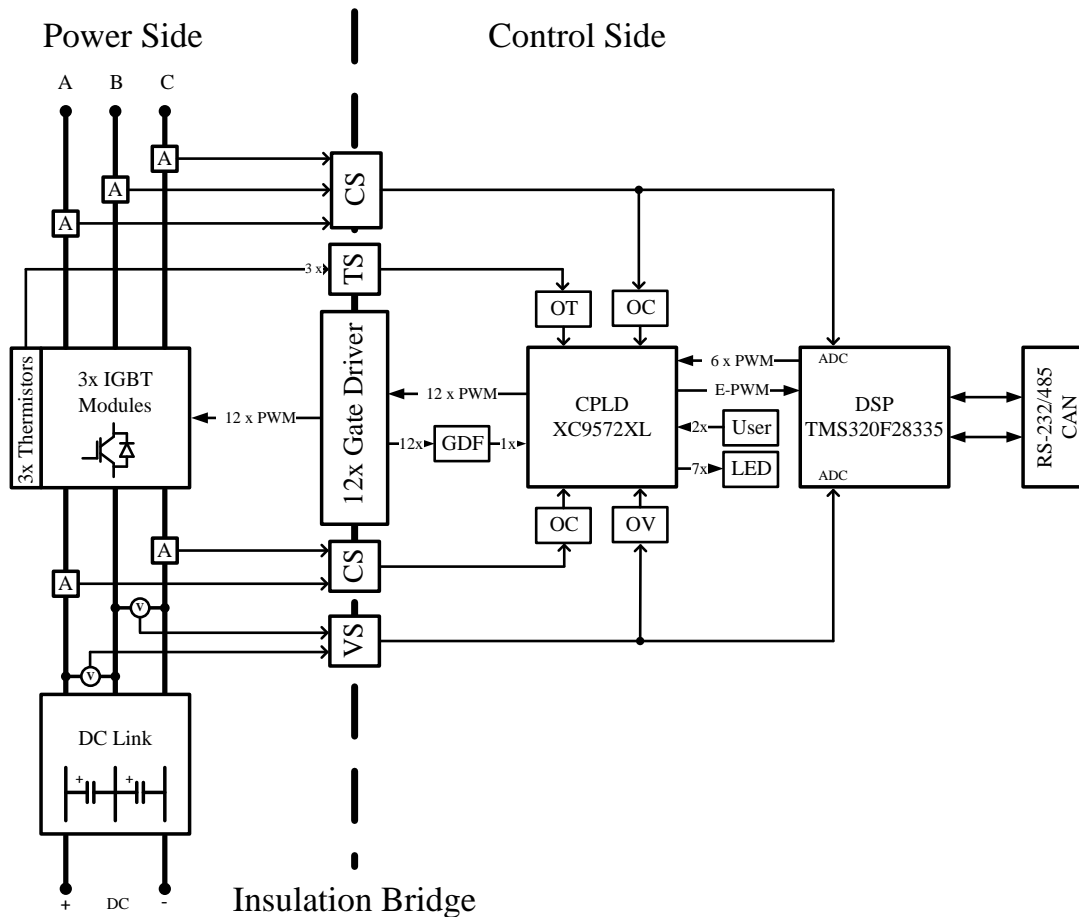


Fig. 5.1. Simplified schematic of constructed converter [7].

To facilitate the communication between these two regions, gate drivers, current sensors, voltage sensors and temperature sensors are used, which ensure that the two regions are decoupled. Also, it should be mentioned that the converter is constructed on a four layer printed circuit board (PCB), with stacked DC link layout, ground and power planes, in order to reduce the interference between different circuits [7].

In the following of this chapter, the main circuits from these two regions are presented.

5.2 Power Side

Besides the power components (IGBT modules and capacitors), the power side of the converter is made out of a series of measurements circuits. These measurement circuits represent the main advantage of this design, because using the signal acquired, a series of protections are implemented, as it can be mentioned: three phase AC over-current protection, DC over-current protection, DC over-voltage protection, over-temperature protection and gate driver protection.

All these main circuits will be shortly presented in the following, in order to highlight the components used and their functionality:

- b) **Capacitor bank**, made out of six 330 μF Panasonic capacitors, arranged in three parallel arms between the +HVDC and 0HVDC and three parallel arms between –HVDC and 0HVDC.
- c) **Three IGBT modules**, each representing one leg of the three level NPC converter;

The IGBT modules are produced by Semikron (SK50MLI065), and have the following properties, according to the datasheet [27]: compact design, 600V/50A per IGBT, direct copper bounded aluminium oxide ceramic (heat transfer and isolation), snubber-less design, improved commutation paths, controlled axial lifetime technology for freewheeling diodes.

- d) **Voltage dividers**, each constructed out of four high value resistors, used in the DC voltage measurement circuit to ensure a permanent connection to the DC link by reducing the current below the resistor current capability and to provide DC link voltage measurement;
- e) **Three NJ28 high accuracy thermistors**, used in the over-temperature protection circuit to detect the temperature of the IGBT modules. The thermistors have a negative temperature coefficient (NTC), meaning that the resistance decreases, while the temperature increases. At 25°C the resistance is 100 [k Ω].
- f) **Five Hall current sensors**, two for the DC side and three for the AC side, used to measure the high currents in the power region and output a reference voltage value which will be used in the control region for over-current protection and as measurement for the DSP;

The current sensors used in this design are Allegro ACS756 Hall Effect IC Sensors, which have the following properties [28]: total output error of 0.8%, very low power loss (130 $\mu\Omega$ resistance),

3kV isolation, small magnetic hysteresis, measurement of $\pm 50\text{A}$, and 2.5V output for 0A with $\pm 40\text{mV/A}$ characteristic.

For each measurement circuit, only the components situated in the power side have been presented here, while the rest of the circuits, which are situated in the control side, are presented in the following section.

5.3 Control Side

The control side of the converter is comprised of circuits which ensure the command, protection, signal acquisition and communication. Because all these circuits are explained in [7] only the main features of each circuit will be presented in the following, to help the reader understand the principle of operation.

1) Gate Driver Circuit

The gate driver Avago ACPL-332j was selected for this design to ensure the interface, protection and isolation between the power side and the control side.

The Avago ACPL-332j gate driver has the following features [29]: optically isolated power stage capable of driving IGBTs up to 150A and 1200V, desaturation detection, isolated fault feedback, active Miller clamping, “soft” IGBT turn off, 2.5A output current, small package.

The PWM signal, sent from the command circuit to the gate driver, is applied to the anode and cathode of the LED situated inside the gate driver. The LED is used in the gate driver to ensure galvanic isolation between the power side and the command side.

To ensure desaturation protection, the collector-emitter voltage (V_{ce}) is monitored during the conduction. If this voltage rises above 6.5V the IGBT is turned off and a fault signal is generated. To avoid false triggering the desaturation detection is disabled when the IGBT is not conducting.

2) Command Circuit

The modulation PWM signals provided to the gate drivers are generated by the digital signal processor (DSP). In the current configuration, the DSP only provides the signals for the upper two switches, of each leg. These six PWM signals are transmitted to the complex programmable logic device (CPLD), as it can be seen in Fig. 5.2.

Using the six PWM signals, the CPLD will generate the complementary PWM signals for the lower two switches of each leg, while introducing the dead time between the complementary signals.

All twelve PWM signals, from the CPLD, are transferred to a pair of octal buffers (SN74LVC540A), six PWM signals for each octal buffer. The octal buffer used in this design acts as a NOT logic circuit. This is because the anode of the LED, situated inside the gate driver, is connected to a 3.3V DC source, and the cathode is connected at the output of the octal buffer.

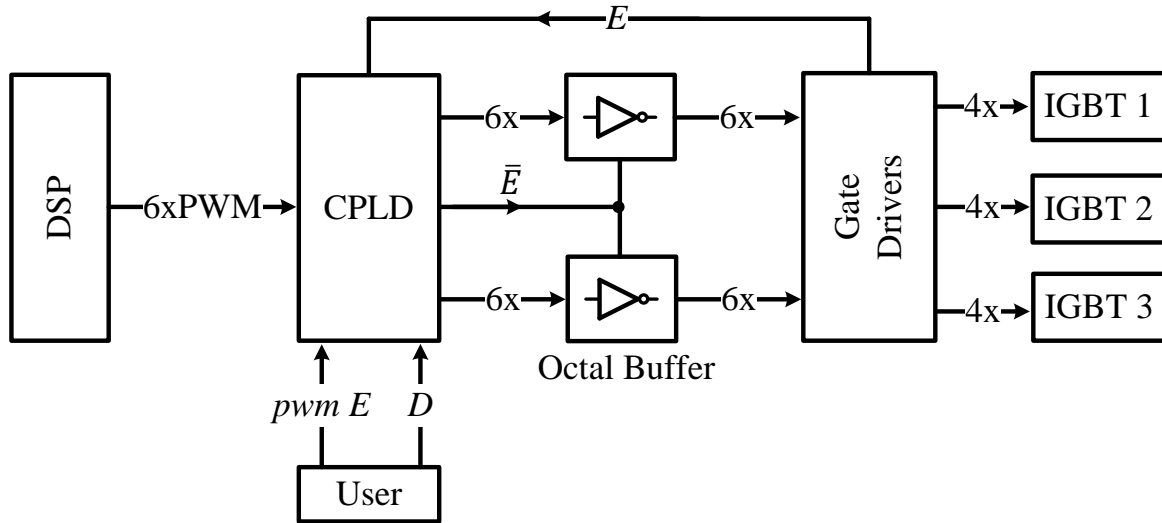


Fig. 5.2. Block diagram of the command circuit.

In this configuration, when a signal is transmitted from the CPLD, 3.3V or logic 1, the octal buffer inverts the signal to 0V or logic 0. The 0V state is transferred to the cathode and a potential difference appears at the LED terminals, enabling the current to pass through the LED, which commands the IGBT to conduct.

In the opposite situation, when the CPLD gives the 0V, or logic 0 command, the octal buffer inverts the signal to 3.3V, or logic 1. In this situation, because the cathode has the same potential as the anode, the current will not flow through the LED, which commands the IGBT not to conduct.

The octal buffers presented in the circuit are also used as a safety feature. When a fault is detected in the converter the octal buffers are disabled and the command to the gate drivers is blocked.

The user has the possibility to control the command circuit through two external buttons. The first button (*pwm E*) is used to trigger the PWM modulation, while the second button (*D*) is used to disable the modulation and to reset the protections.

3) Current Measurement Circuit

As stated earlier, five Hall current sensors are used in the converter. Two sensors are used for the DC link current and three sensors are used for the AC phase current. The current measurement circuit is implemented only for the AC phase current sensors. The circuit is comprised of the following components:

- Hall current sensor, presented earlier, which gives a reference of 2.5[V] at 0[A], and has a ± 40 [mV/A] characteristic.
- Voltage divider, is used to reduce the voltage level at 1.6667[V] for 0[A], with a characteristic of ± 26.6667 [mV/A]. This is done because the input signal to the DSP has to be in the 0-3[V] range.

- ADC buffer, constructed from an operational amplifier which is configured as a voltage follower, to isolate the ADC input of the DSP from the signal source;
- Two pairs of dual series small signal Schottky diodes, one before the ADC buffer, and the other after the ADC buffer; used to limit the voltage signal in the 0-3[V] range;
- ADC input port of the DSP;

To have a better understanding of how these components are connected to form the current measurement circuit, a block diagram of the circuit is presented in Fig. 5.3.

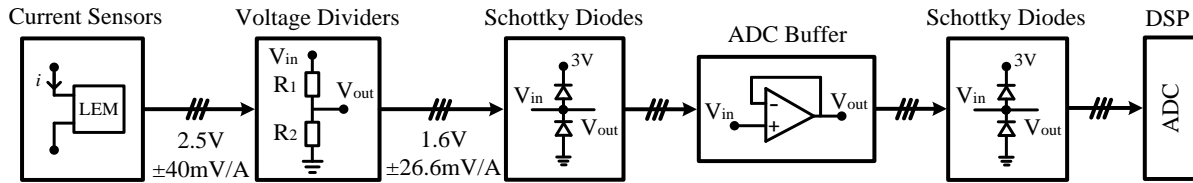


Fig. 5.3. Block diagram of current measurement circuit.

4) Over-Current Protection

The over-current protection circuit is implemented for all five current sensors. By doing this, protection is ensured for the DC side and for the AC side of the converter.

The over-current protection circuit is comprised out of (Fig. 5.4):

- Hall current sensor, same as for the current measurement circuit;
- Window comparator; for each measured signal a window comparator is used, to compare the signal with two reference signals, maximum and minimum reference. These two references can be set by the user through variable resistors. When the measured signal is between the two boundaries the window comparator has a high output state, which signals correct operation.
- Logic AND circuit. The signals from the window comparators are entered a logic AND circuit, and the result is sent to the CPLD.
- CPLD, receives the signals from the AND circuit and takes the appropriate action.

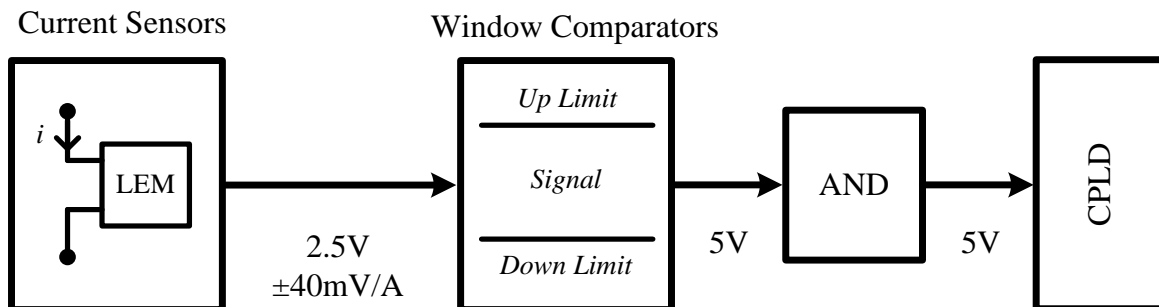


Fig. 5.4. Block diagram of the over-current protection circuit.

5) Voltage Measurement Circuit

In order to protect and control the converter, a voltage measurement circuit, for the DC voltage, is implemented on the converter. The circuit is comprised of (Fig. 5.5):

- Voltage dividers; as mention earlier, four voltage dividers are used to acquire the voltage signal from the DC link.
- Differential amplifier; Two differential amplifiers are used to manipulate the signal received from the voltage dividers.
- Voltage dividers; at the output of each differential amplifier a new voltage divider is placed to reduce the voltage level which goes to the ADC buffer;
- Schottky diodes and ADC Buffer with the same structure as for the current measurement circuit.

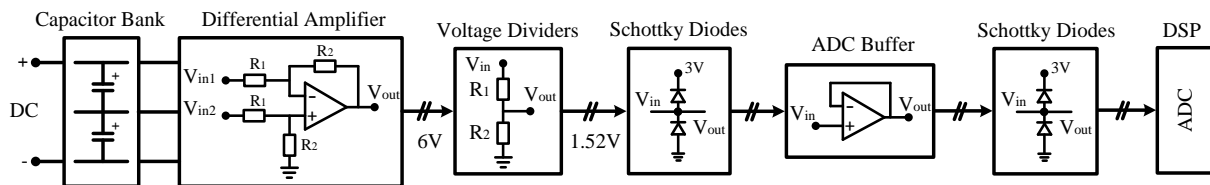


Fig. 5.5. Block diagram of the voltage measurement circuit.

Using this signal and the current signals a closed loop control can be implemented on the convertor, in order to increase the dynamic performance of the drive.

6) Over-Voltage Protection

In order to ensure the DC over-voltage protection and to simplify the hardware structure the circuit is comprised of components similar with the voltage measurement circuit and over-current protection circuit:

- Voltage dividers, differential amplifier and voltage dividers (components presented in the voltage measurement circuit);
- Window comparator; for each measured signal a window comparator is used, to compare the signal with two reference signals, maximum and minimum reference. These two references can be set by the user through variable resistors. When the measured signal is between the two boundaries the window comparator has a high output state, which signals correct operation.
- Logic AND circuit. The signals from the window comparators are entered a logic AND circuit, and the result is sent to the CPLD. In this way the CPLD is announced if an over-voltage situation appears in the converter.
- CPLD, which receives the signal from the fail gate and takes the appropriate action.

The circuit structure, in block diagram form, is presented in Fig. 5.6.

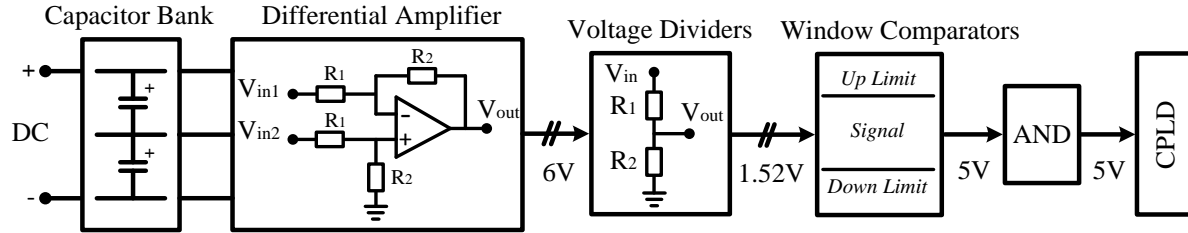


Fig. 5.6. Block diagram of the over-voltage protection circuit.

7) Over-Temperature Protection

The over-temperature protection circuit is used as a safety feature for long time operation. If the module temperature increases over a specified limit, the circuit is disabled and the fault is signalled to the user. The circuit is made out of the following components:

- Signal conditioning circuit; the thermistors are connected in a resistive circuit in order to modify the NJ28 characteristics.
- Window comparators; In this case the window comparator works different. The output of the acquisition circuit is inverted for both comparators, so that the comparators output is high (healthy situation) if the temperature is below the preset limits.
- Two logic AND gates are used to deal with the temperature measurement circuit, because there are two preset limits of temperature.
- CPLD receives the signal from the fail gate and takes the appropriate action.

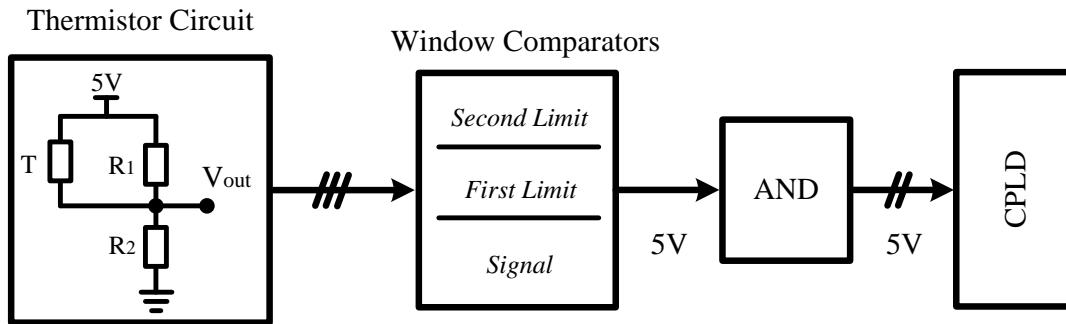


Fig. 5.7. Block diagram of the over-temperature protection circuit.

8) Communication Circuit

The converter has also implemented two communication circuits, CAN and RS-232/485, in order to facilitate the communication between the converter and an external program. Because this feature is not used in the current project it is not presented here. To get some knowledge about these two circuits please refer to [7].

6

Laboratory Experiments

This chapter presents the practical work done in the laboratory. At the beginning, the laboratory setup used to do all the experiments is presented. The experimental results are separated in two parts, based on the type of control implemented. The first part presents the tests done using scalar control, while the second part presents the tests done using vector control. The tests done on the drive are selected to be similar with the simulations.

6.1 Laboratory Setup

The laboratory setup used to do all the tests is presented in Fig. 6.1. The components that comprise the setup are: voltage source (grid), autotransformer, three phase diode bridge rectifier, resistor, three level NPC converter, PMSM, load machine, converter for the load machine and voltage source for the converter (grid). Also, two personal computers (PC) are used to independently control the two converters.

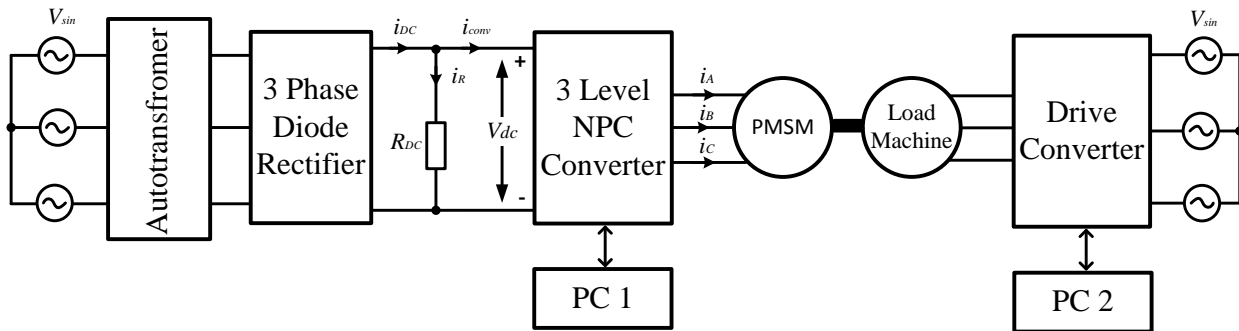


Fig. 6.1. Bloc diagram of laboratory setup.

In order to drive the PMSM, power is taken from the grid through an autotransformer and a three phase diode bridge rectifier. The autotransformer is used to adjust the DC link voltage at the output of the three phase diode bridge rectifier.

The configuration with autotransformer, diode bridge rectifier and resistor is used, instead of a simple DC voltage source, because the machine has to be controlled in generator mode. When the machine is working in generator mode, the three level NPC converter will behave as a rectifier, sending the AC power from the PMSM to the DC link. In this situation the power will be dissipated on the resistor, because the three phase diode bridge rectifier will block the power flowing to the grid.

A second synchronous machine is connected to the shaft of the PMSM, to act as a mechanical load. Torque control is implemented as a control strategy on the load machine.

A more in depth presentation of the laboratory setup is made in the videos written on the CD, which is attached to this report.

Because the DC link voltages are very similar for all the experiments, these results are presented in Appendix B, to avoid presenting very similar oscilloscope captures and repeating the same conclusion for each situation.

As stated in the chapter description, the following section will be divided in two parts. The first part presents the tests done using sensorless scalar control, while the second part presents the tests done using sensorless vector control.

6.2 Scalar Control Experiments

6.2.1 Speed reference variation

The speed control capability is tested in the first experiment. Because the dynamic response of the control is slower, the speed reference is modified using a ramp variation.

At the beginning the machine is started from zero to nominal speed in two seconds. As it could be seen in Fig. 6.2, no initial vibration occurs in the rotor during the starting procedure.

It has to be noted here that after numerous test made in the laboratory, it was observed that for different initial rotor positions, rotor vibrations can occur during the start up. To examine this behaviour the starting procedure was repeated at different initial rotor positions. From the results, it was observed that the rotor vibration depends on the initial position, and the control is able to start the machine independent of the rotor position.

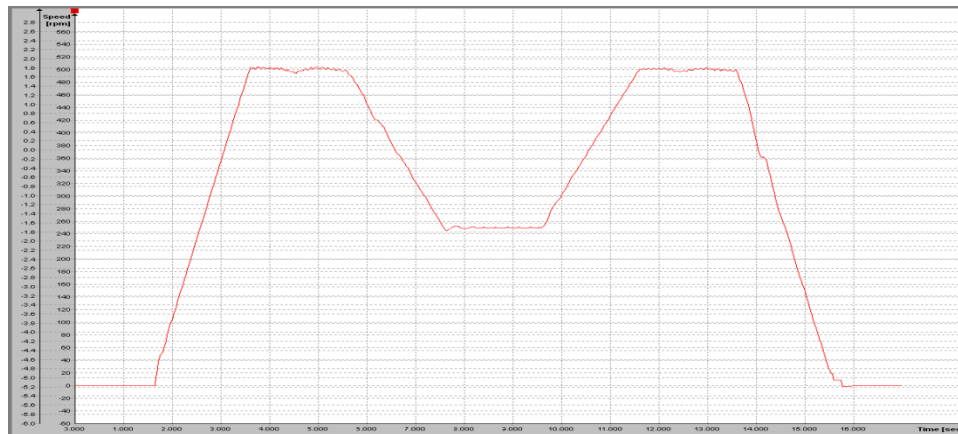


Fig. 6.2. Machine speed during speed reference variation (scalar control).

The speed of the machine is maintained at the same level for another two seconds, before is reduced to 50% of the nominal speed, in two seconds. After another two seconds, the speed is increased to nominal speed. The last part of the control focuses on stopping the machine. The speed of the machine is brought down to zero with a ramp variation, in two seconds.

The waveform of the phase current, during the entire test procedure is presented in Fig. 6.3. From this figure it can be seen that variations in current magnitude appear only during the transition period. In steady state, the control is able to maintain the amplitude of the current at the reference value during the entire testing procedure.

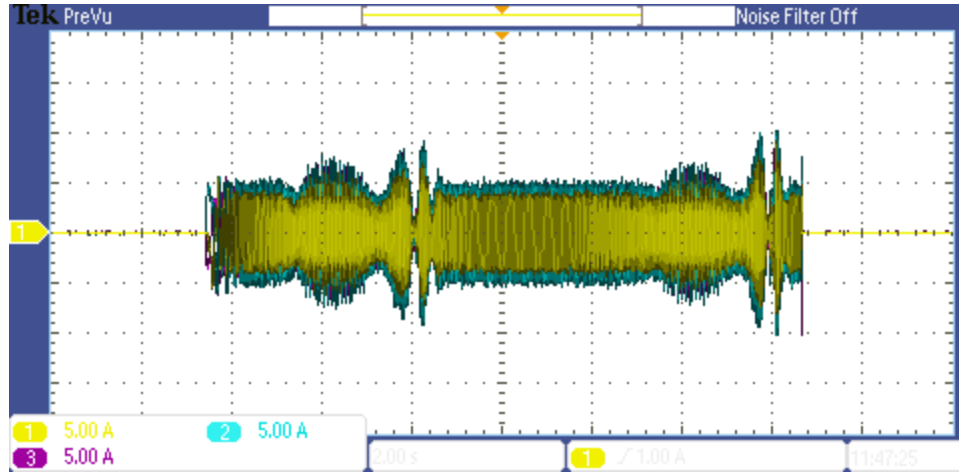


Fig. 6.3. Current waveform during scalar speed control ($i_q^* = \text{const.}$).

Similar to the simulation, a second experiment is done, where the reference quadrature axis current (i_q^*) varied as a function of frequency (Fig. 4.4). The current waveform for the second situation is presented in Fig. 6.4.

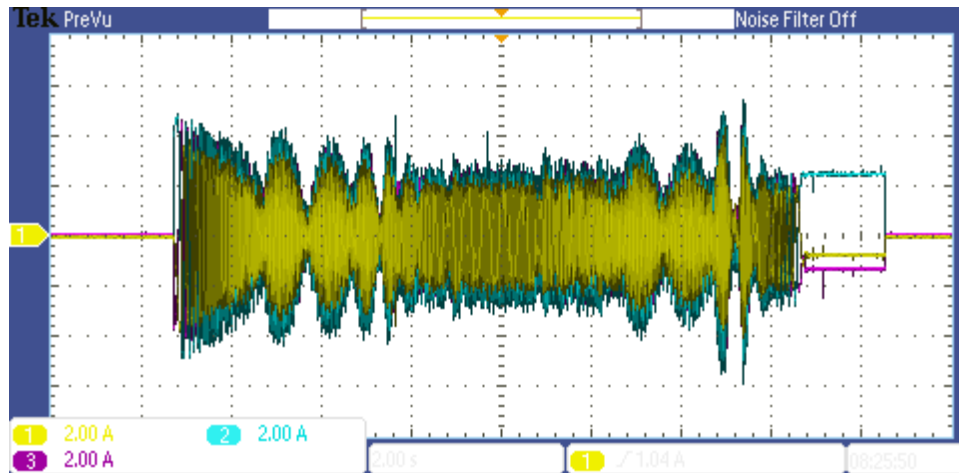


Fig. 6.4. Current waveform during scalar speed control ($i_q^*(f^*)$).

The decrease in current magnitude can be observed in the first region of Fig. 6.4. Compared to the initial situation, more powerful oscillations appear in the system. Because the result obtained here is similar with the simulation, the same conclusions are valid.

6.2.2 Load torque variation

As a second test, the load torque is modified in steps, to test the response of scalar control, when a load disturbance appears in the system. The result presented in Fig. 6.5 shows that the control

is capable to maintain the stability of the system. When the load torque is applied, the speed decreases only 1.4% from the nominal speed. System stability is achieved again, after one second of transitory regime.



Fig. 6.5. Machine speed (red) and load torque (blue), during load torque variation (scalar control).

When the load torque is removed, the speed increases with the same magnitude as for the previous case. A decreasing oscillatory regime is encountered in this situation, compared to the previous one. These oscillations can also be observed in the current waveform Fig. 6.6.

This test is done with the reference quadrature axis current (i_q^*) constant, to better highlight the disadvantage of this method. Although the control is able to maintain the current at a constant value, as it is required, this operating procedure is not efficient.

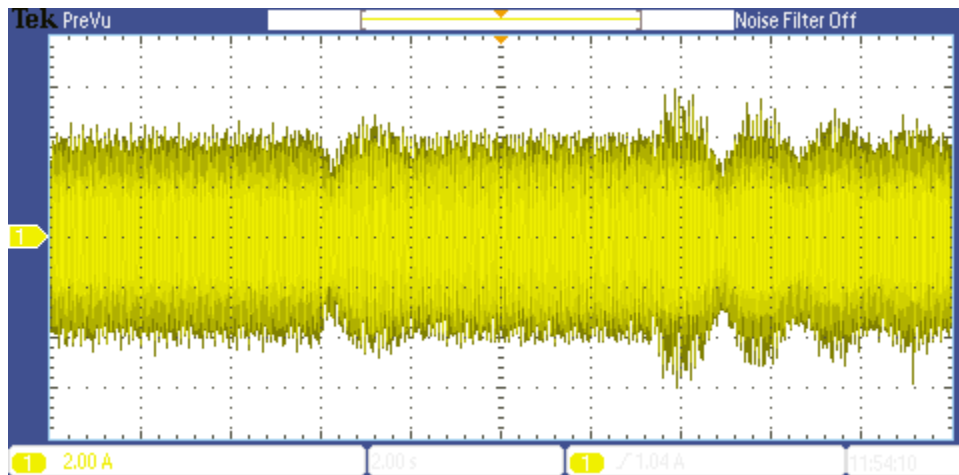


Fig. 6.6. Current waveform during load torque variation ($i_q^* = \text{const.}$).

6.3 Vector Control Experiments

6.3.1 Speed reference variation

All the conditions used to do the simulation are applied for this laboratory experiment.

From Fig. 6.7, it can be seen that the control is able to start the machine in 0.5 seconds, with no initial rotor vibrations. It has to be noted here, that similar to scalar control, the vibration is dependent on the rotor initial position.



Fig. 6.7. Machine speed during speed reference variation (vector control).

The reduced transition time between steady state situations, highlights the superior dynamic performance of vector control, compared to scalar control.

From the current waveform, presented in Fig. 6.8, it can be seen that the current is maintained between the safety boundaries, during the transient regime. Also, a far better efficiency is achieved, compared to scalar control, through MTPA strategy.

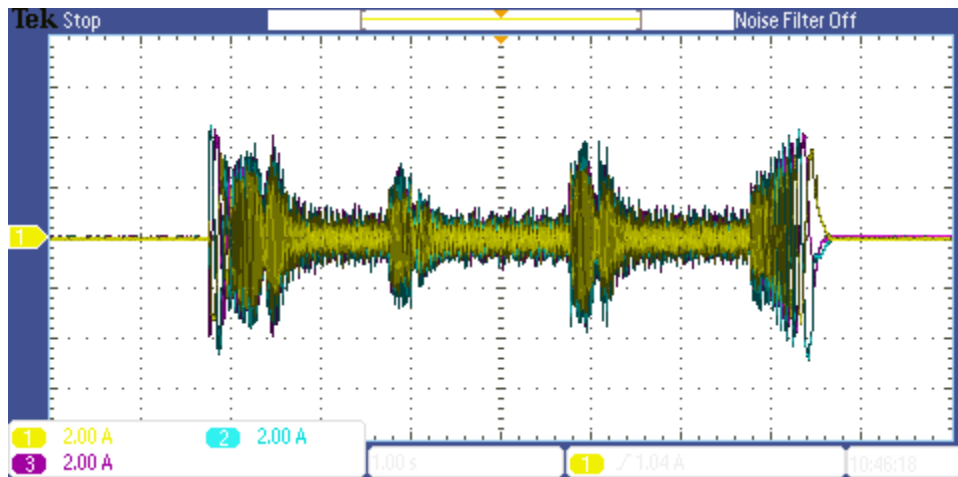


Fig. 6.8. Current waveform during vector speed control.

6.3.2 Load torque variation

In the second test, the stability of the control, during load torque variation, is tested. The load torque is applied at the shaft, using the secondary machine. The result of the test is presented in Fig. 6.9. As it can be seen, when the load torque is applied, the control is capable to correct the 3.6% speed decrease, in approximately three seconds.

When the load torque is removed, the speed reaches a maximum value of 6%, above the nominal speed. As for the previous situation, the control is capable to ensure stability, by reducing the speed at nominal value, in approximately four seconds.



Fig. 6.9. Machine speed (red) and load torque (blue), during load torque variation (vector control).

The current waveform, presented in Fig. 6.10, displays the current transition during the entire experiment. As it can be seen, during the load torque transition, the current is maintained inside predefined limits to ensure safe operation.

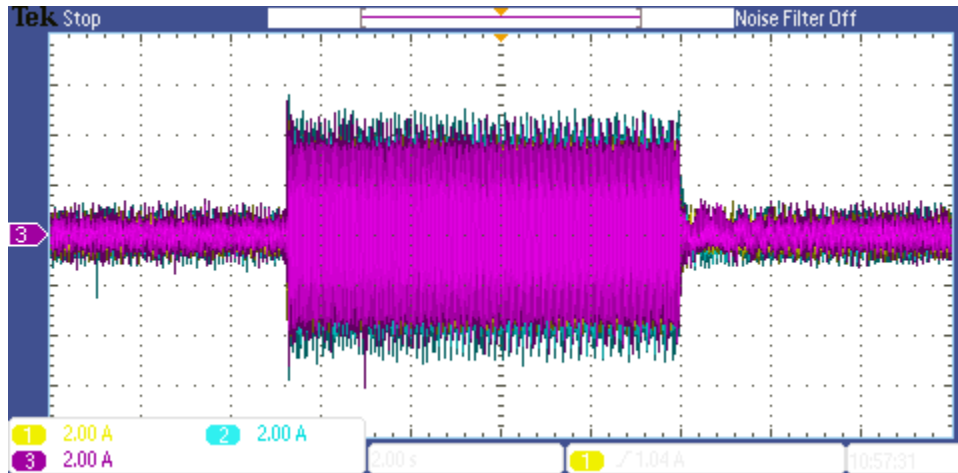


Fig. 6.10. Current waveform during load torque variation.

6.3.3 Transition from motor to generator

From Fig. 6.11 it can be seen that the transitory regime is very similar to the previous case. The speed increases at the moment when the torque is applied with approximately 1.6%. The control is able to limit the speed increase and to stabilise the system.

When the load torque is removed, the machine changes to motor mode and the speed decreases. As for the previous case, the control is able to stabilise the system, and to ensure nominal speed.

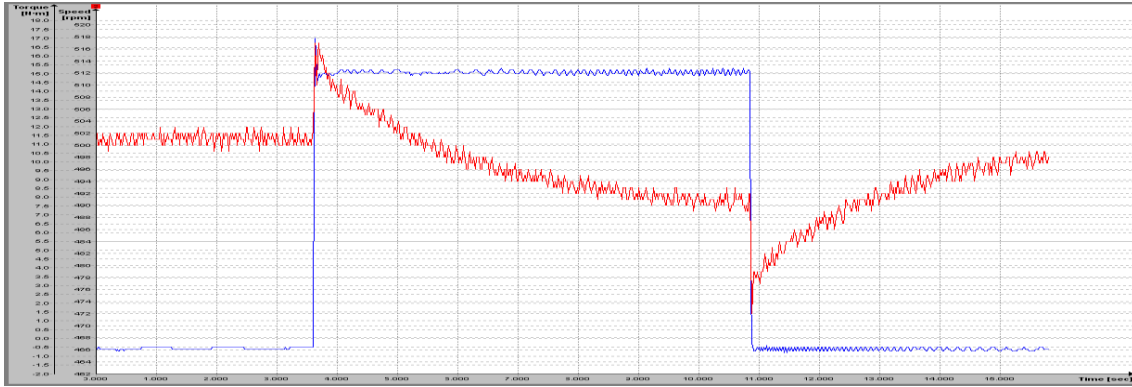


Fig. 6.11. Machine speed (red) and load torque (blue), during motor-generator transition.

The current waveform (Fig. 6.12), during the entire process, is very similar with the previous case. The control ensures that the current is maintained between the safety margins during the transition from motor to generator and back.

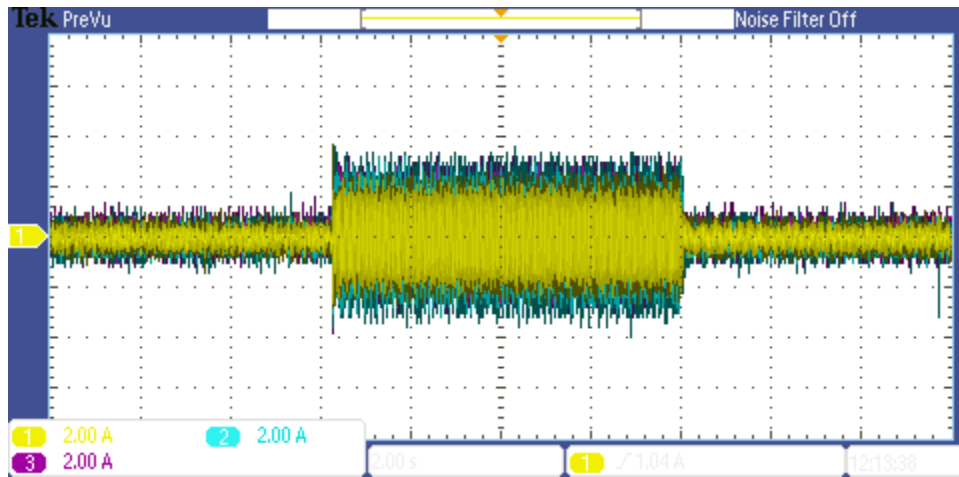


Fig. 6.12. Current waveform in motor and generator mode.

To observe the current direction during generator mode, the DC link current that enters the converter was measured with the oscilloscope.

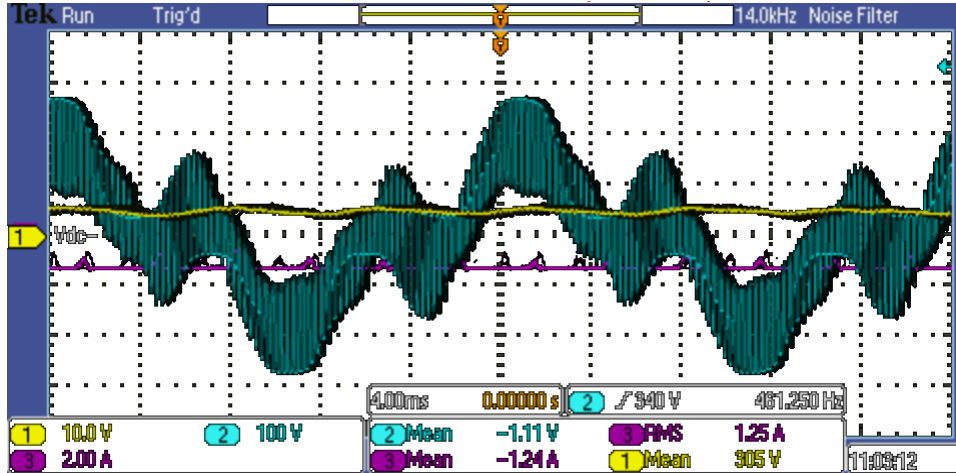


Fig. 6.13. DC link current (magenta), phase voltage (cyan) and V_0 voltage (yellow) in generator mode.

As it can be seen from Fig. 6.13, the DC link current that enters the converter (red line), has a negative sign, meaning that the current flows from the converter to the resistor.

6.3.4 Emergency breaking

To observe the difference between simulation and experiment, the same test conditions were used. From Fig. 6.14, it can be seen that the transition from nominal to zero speed is linear. The control is capable to follow the ramp reference given.

When the speed is reduced close to zero, the control encounters stability problems, because the speed and position estimator cannot provide very accurate information.

Although the speed of the machine will not be kept constant at zero, the sensorless control can maintain the speed in a low range, characterised by rotor vibrations.

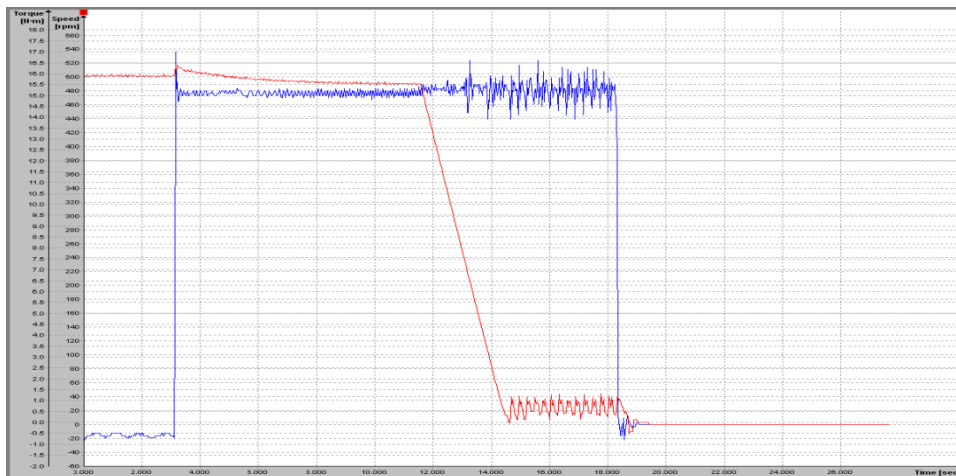


Fig. 6.14. Machine speed (red) and load torque (blue), during emergency breaking.

In the last part of the test, after the machine is brought down to zero speed, the load torque is eliminated. In this situation the control maintains the speed at zero, without rotor vibrations.

The difference between the simulation and experiment is consistent during the low speed operation. This is because the experiment requires accurate position information to maintain stability. Because the position cannot be estimated at zero speed, the speed cannot be maintained zero. In order to obtain better control at very small speed, a dedicated position estimator has to be implemented in the control.

The current waveform is presented for the entire test in Fig. 6.15. As it can be seen, the current increases slightly in magnitude, as the speed decreases. When the speed of the machine reaches values closed to zero, the current maintains a high magnitude to produce sufficient torque.

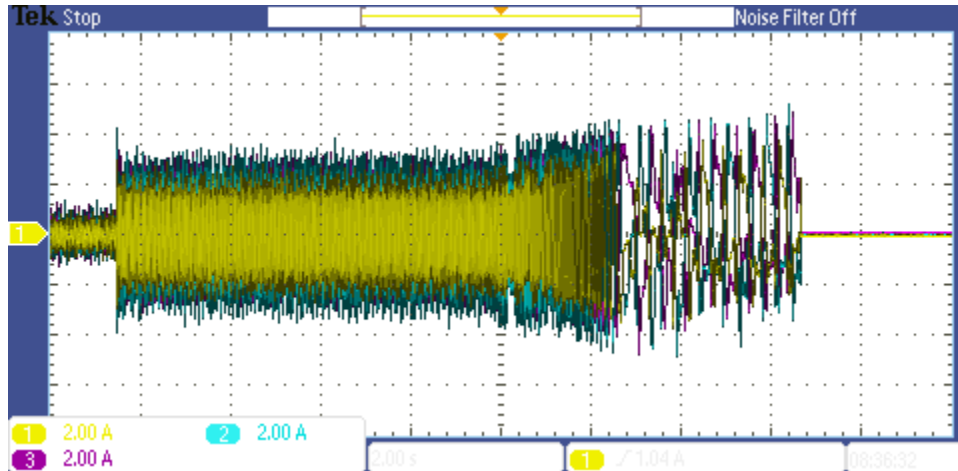


Fig. 6.15. Current waveform during emergency breaking.

6.3.5 Holding the machine at zero speed

The result of the test is presented in Fig. 6.16. From the result it can be seen that when a load torque is applied at the shaft, the control encounters problems to maintain the stability.

Similar with the emergency breaking case, at low speed the control is unable to maintain the speed at a constant zero value. The reason for this problem is the same as for the previous case.



Fig. 6.16. Machine speed (red) and load torque (blue), during zero speed test.

Another observation has to be made here. If a considerable torque step is applied at the shaft, the control is not able to counteract, causing instability.

The current waveform from Fig. 6.17, presents a similar behaviour to the previous case (Fig. 6.15). During low speed operation the current is situated inside the safety margins, and has an irregular form, caused by the poor stability.

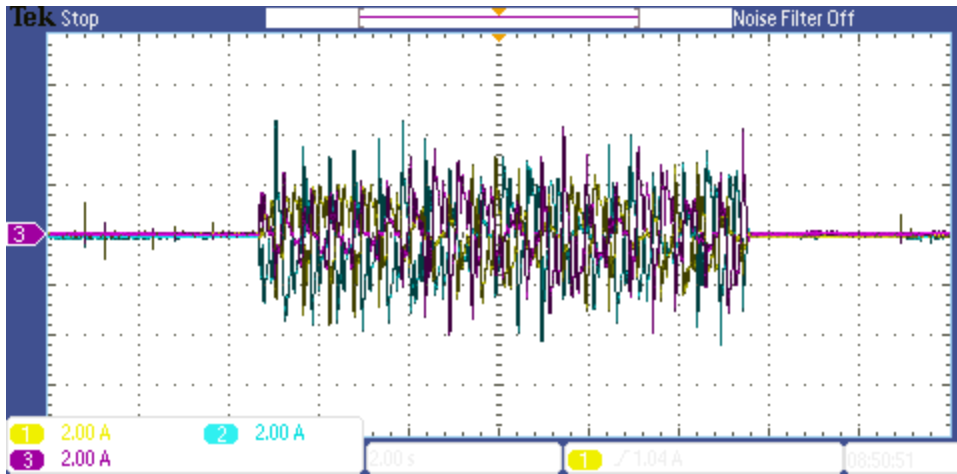


Fig. 6.17. Current waveform during zero speed.

7

Conclusions

From the current project a series of conclusions can be drawn. These conclusions are separated based on the topic they address.

➤ **Conclusions regarding the converter:**

The three level NPC converter is a viable solution for this wind turbine application, because it provides numerous advantages compared to the two level converter, while the disadvantages are not so significant.

The prototype constructed in the laboratory was able to fulfill all the requirements imposed during the experiments.

➤ **Conclusions regarding the control:**

The scalar control strategy implemented in the current project cannot be implemented as the main control for the wind turbine, because it cannot provide stability in all situations.

Scalar control can be recommended for certain situations, as maintenance situations, when the speed of the turbine is small [19].

The speed and position estimator provided fast and accurate information, for the medium and high speed range, as it was observed in simulations and experiments.

Problems were encountered at speeds closed to zero, as it could be seen in the experiments, because the estimator determines the position from the back-EMF term, which is proportional with the speed.

The sensorless vector control was able to maintain the stability, and to provide good dynamic response during the starting procedure.

For a more stable operation at zero and very low speeds, a dedicated estimator has to be implemented.

Appendix A. Reference Frame Transformation

To create the mathematical model of an electrical machine the three phase “abc” system was initially used, because it relates to the physical machine [30, 31]. Because this system comes with disadvantages like time varying components and complex differential equations, new reference frame transformations were developed to deal with these problems. The new variables obtained, after reference frame transformation, do not have a physical correlation to the real variables, which are encountered in the three phase ‘abc’ system.

a) Reference frame transformation from “abc” to “ $\alpha\beta 0$ ”

If we consider the three phase system “abc” and the complex domain, in which “a” axis is along the real axis, the “ $\alpha\beta 0$ ” system can be developed, where α is along the real axis, β is along the imaginary axis and 0 is the zero component of the three phase system, perpendicular to the plan of the paper. It should be noted that the $\alpha\beta 0$ reference frame is fixed to the stator. The transformations from “abc” to “ $\alpha\beta 0$ ” reference frame and vice versa are made using the transformation matrix presented in [1] and [2] [30, 31].

This new reference frame presents advantages in the study of transient regimes for unbalanced three-phase circuits [30, 31].

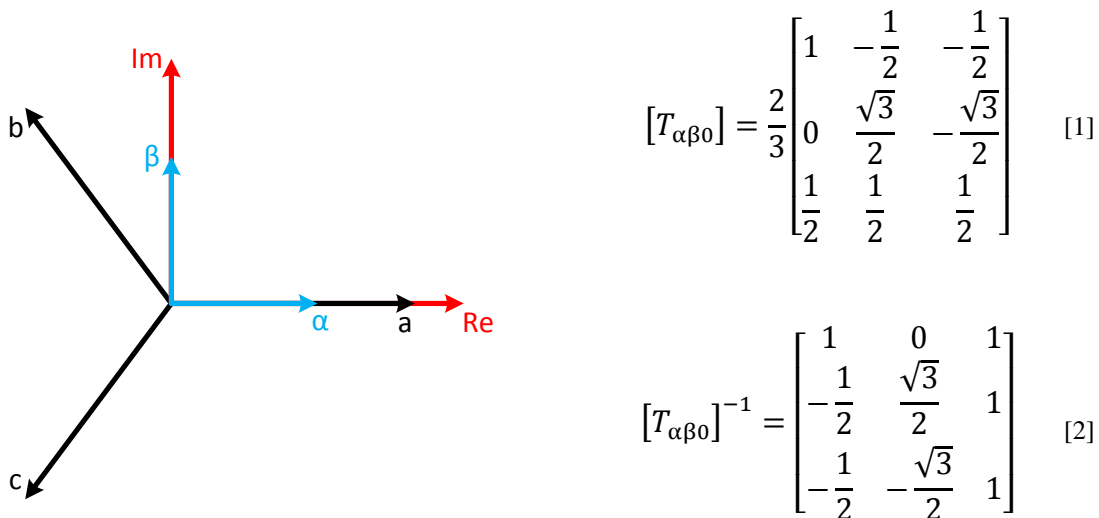


Figure 1. Reference frame transformation from “abc” to “ $\alpha\beta 0$ ”.

b) Reference frame transformation from “abc” to “dq0”

As in the “ $\alpha\beta 0$ ” reference frame the “dq0” reference frame is represented in the complex domain, where the “d” axis is along the real axis, the “q” axis is along the imaginary axis and the zero component is the same [30, 31]. The difference between these two reference frames is that the “dq0” is fixed to the rotor and it is rotating with the same speed ω_r compared to the stator.

The transformation from “abc” to “dq0” reference frame is made using the transformation matrix presented in, also called Park matrix [30, 31]. To make the transformation from “dq0” back to “abc” the inverse of the matrix is required. This matrix is presented in [4].

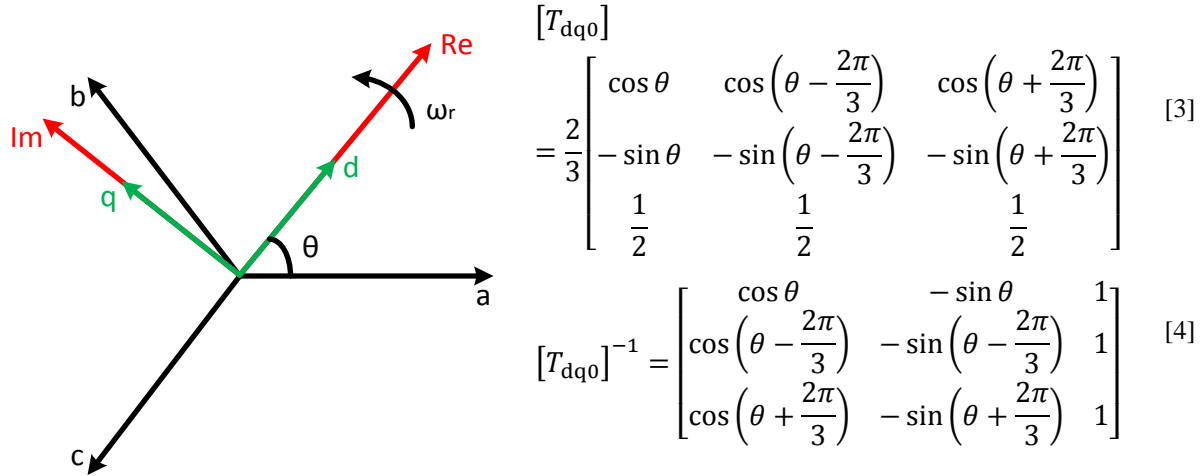


Figure 2. Reference frame transformation from “abc” to “dq0”.

For this transformation the equivalence between the number of turns in the real machine and in the equivalent machine is:

$$n_d = n_q = n_a \quad [5]$$

, where: $n_{d,q,a}$ - number of turns on d, q or a axis;

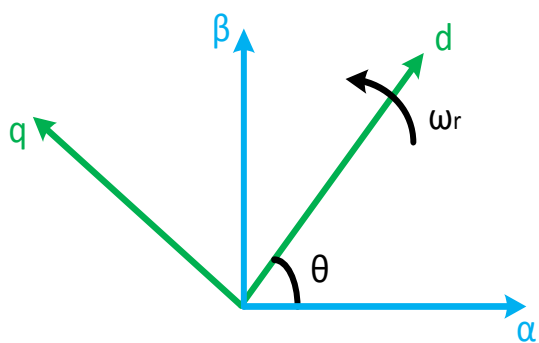
The balance of powers between the “abc” and the “dq0” reference frame is affected by the 3/2 coefficient [30, 31]:

$$p = u_a i_a + u_b i_b + u_c i_c = \frac{3}{2} (u_d i_d + u_q i_q + u_0 i_0) \quad [6]$$

c) Reference frame transformation from “αβ0” to “dq0”

In many applications it is also required to perform the transformation from “αβ0” to “dq0”. As stated before the difference between the two is that “αβ0” reference frames is fixed to the stator and “dq0” reference frames is fixed to the rotor and is rotating with the same speed.

The transformation from “αβ0” to “dq0” reference frame is made using the transformation matrix given in [7], and inverse transformation from “dq0” to “αβ0” is also presented in [8] **Error! Reference source not found.**



$$[T_\theta] = \begin{bmatrix} \cos \theta & \sin \theta & 0 \\ -\sin \theta & \cos \theta & 0 \\ 0 & 0 & 1 \end{bmatrix} \quad [7]$$

$$[T_\theta]^{-1} = \begin{bmatrix} \cos \theta & -\sin \theta & 0 \\ \sin \theta & \cos \theta & 0 \\ 0 & 0 & 1 \end{bmatrix} \quad [8]$$

Figure 3. Reference frame transformation from "αβ0" to "dq0".

Appendix B. Neutral Point Voltage Balance Results

To ensure neutral point voltage balance, the SVM method presented in Modulation Strategies subchapter was implemented on the DSP. An RL load was used to test the modulation.

From Figure 4, it can be seen that the modulation produces nine voltage levels ($\pm 400\text{V}$, $\pm 300\text{V}$, $\pm 200\text{V}$, $\pm 100\text{V}$, 0V), as it was expected. All these voltage levels appear because the modulation index is set to one.

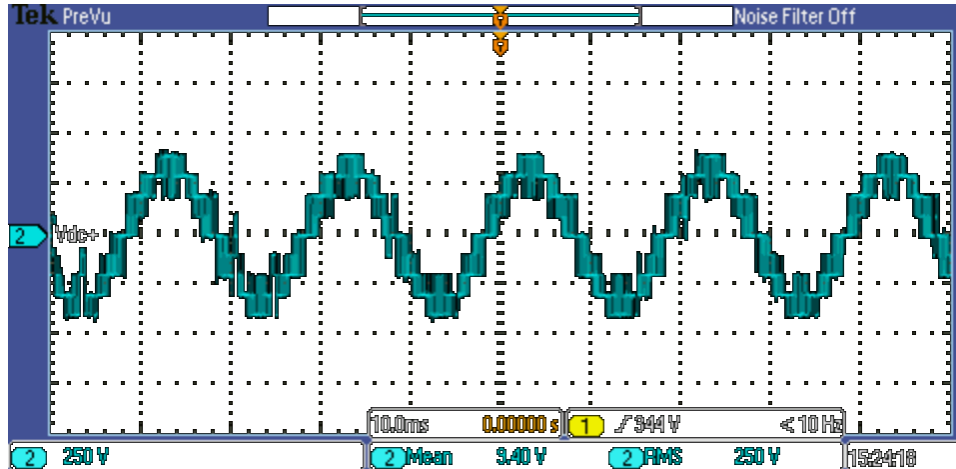


Figure 4. Phase voltage.

From Figure 5, the phase to phase voltage is observed. In this situation, five voltage levels appear ($\pm 600\text{V}$, $\pm 300\text{V}$, 0V).

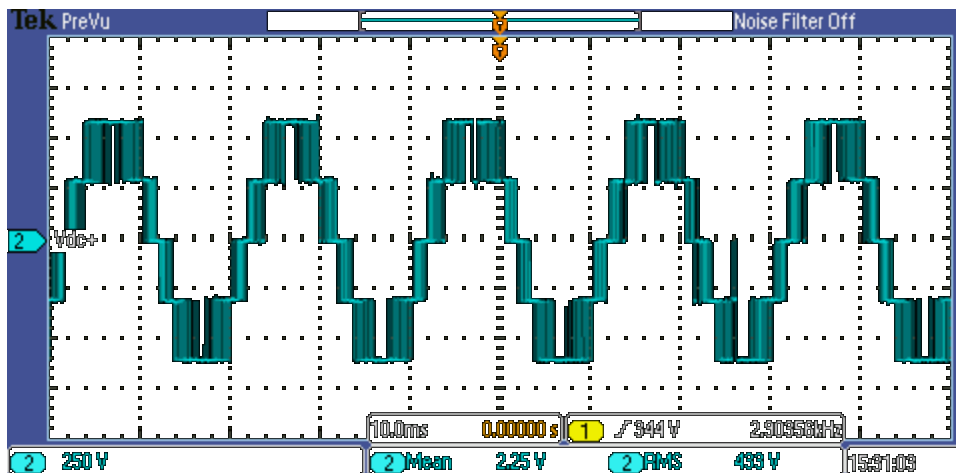


Figure 5. Phase to phase voltage.

For all the experiments done in the laboratory, sinusoidal pulse width modulation is used. This control does not have the capability to maintain the neutral point voltage balance, when an external influence appears. However, if no such influence appears, the balance is maintained naturally by the modulation, as it can be seen from the following oscilloscope captures.

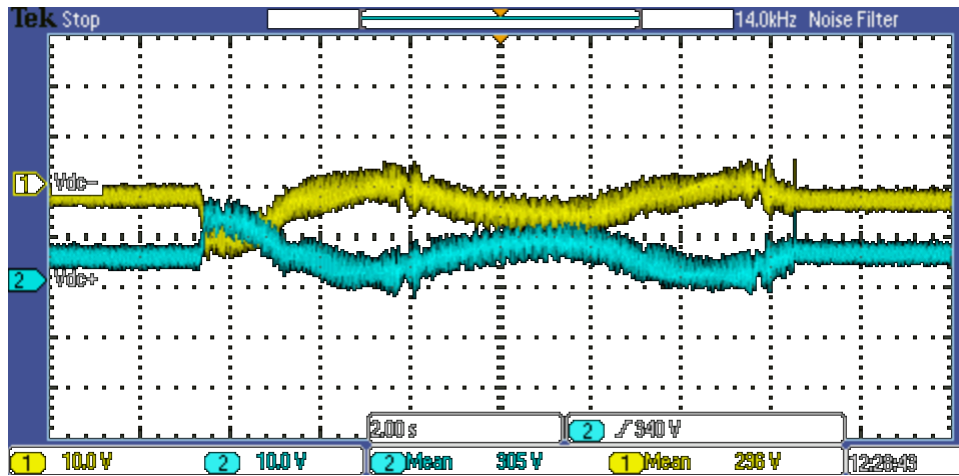


Figure 6. Speed reference variation (scalar control).

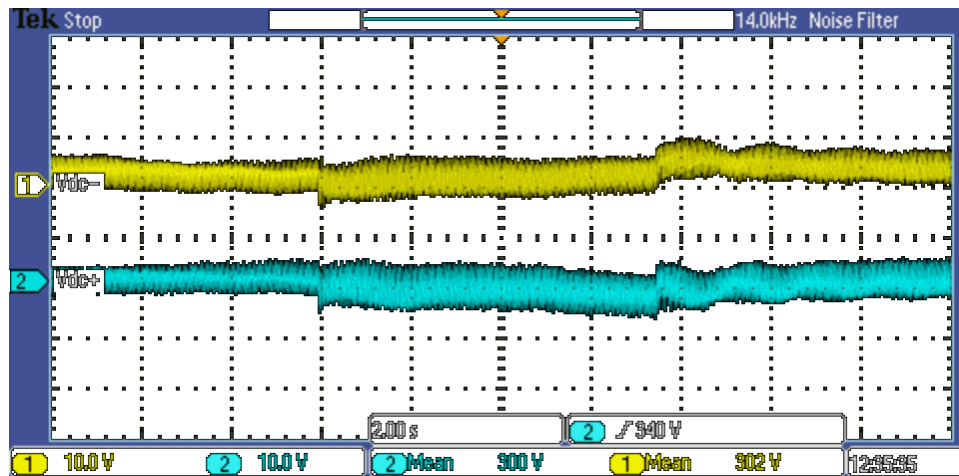


Figure 7. Load torque variation (scalar control).

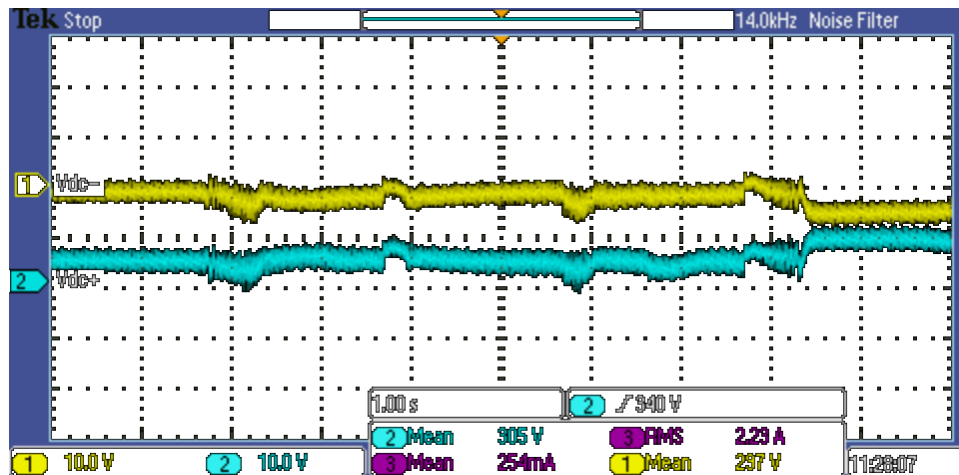


Figure 8. Speed reference variation (vector control).

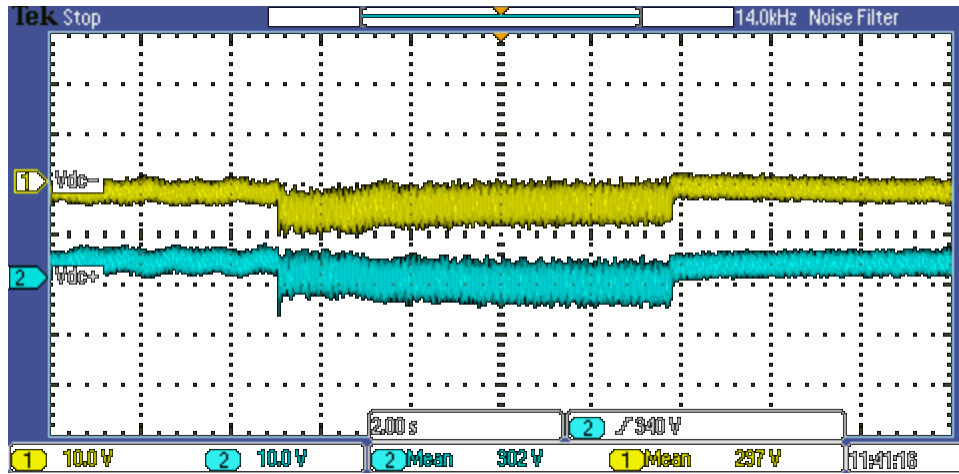


Figure 9. Load torque variation (vector control).

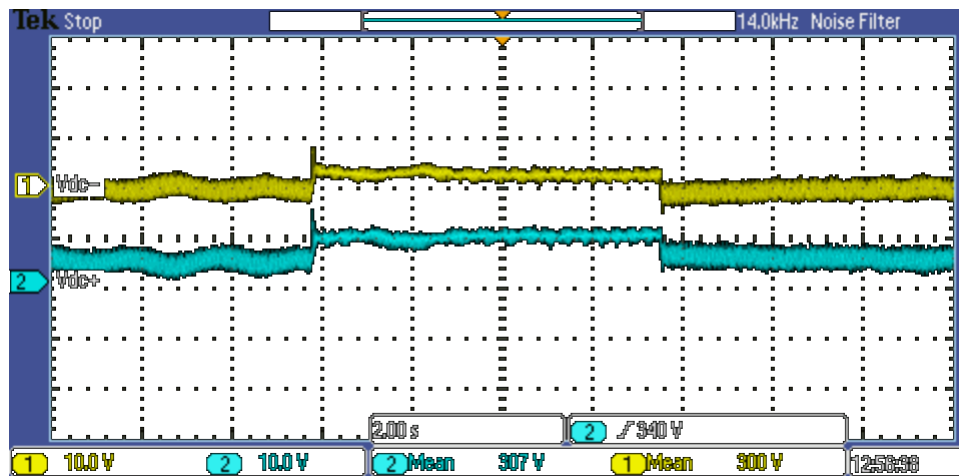


Figure 10. Transition from motor to generator (vector control).

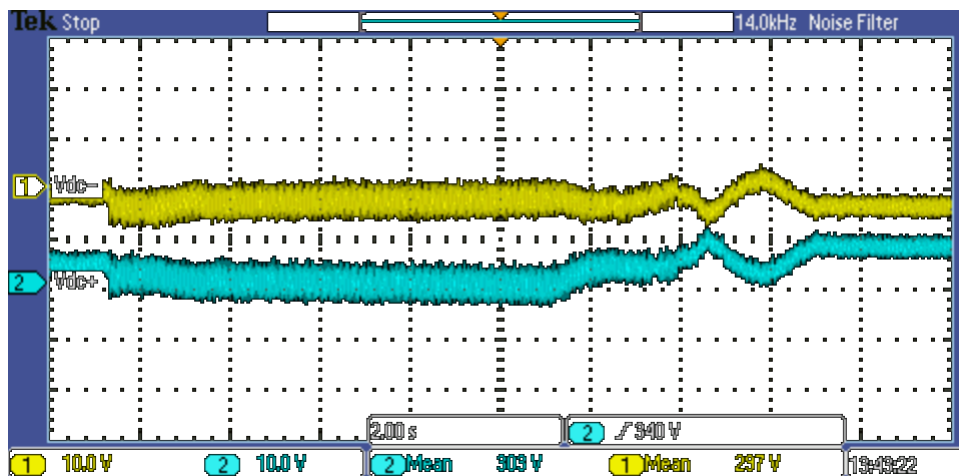


Figure 11. Emergency breaking (vector control).

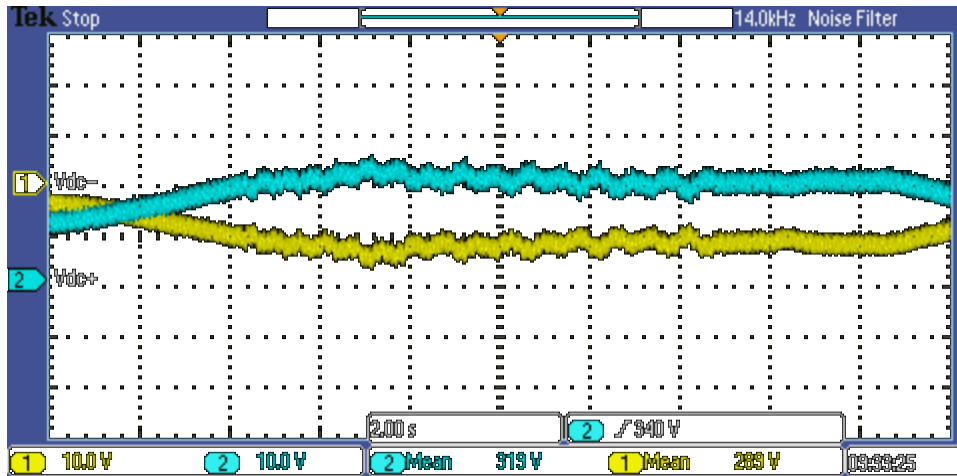


Figure 12. Holding the machine at zero speed (vector control).

As it could be seen from all the oscilloscope captures, the natural balance of the DC link is maintained during the test procedure.

It has to be noted here though, that it is recommended to implement a balance control algorithm, to ensure safe operation, in all situations.

Appendix C. Numeric Parameters

The parameters used to construct the Simulink model and to implement the control are presented in the following table.

Name	Symbol	Value	Unit
Rated Speed	N_n	500	[rpm]
Stator Resistance	R_s	0.71	[Ω]
Synchronous Inductance	L_d	17.0466e-3	[H]
Synchronous Inductance	L_q	15.6869e-3	[H]
PM Flux Linkage	λ_{mpm}	0.4932	[Wb]
No. of pole pairs	p	6	[-]
Viscous Damping	B	1e-3	[-]
Coulomb Friction	T_c	7.7	[Nm]
Rotor Moment of Inertia	J_i	95.107e-3	[kg*m ²]
Assambly Moment of Inertia	J	102.738e-3	[kg*m ²]
DC link voltage	V_{dc}	600	[V]
DC link capacitance	C_{dc}	330e-6	[F]
Carrier Frequency	F_s	4000	[Hz]
Dead time	$Dead_{time}$	1.5e-6	[s]

Bibliography

- [1] (2014, January 30). *Understanding the 2030 Climate and Energy Framework (Analysis of Impact Assessment)*. Available: <http://www.erec.org/>;
- [2] (2014, February 05). *Global Wind Statistics 2013*. Available: http://www.gwec.net/wp-content/uploads/2014/02/GWEC-PRstats-2013_EN.pdf.
- [3] (2011, July 01). *Pure Power; Wind energy targets for 2020 and 2030*; Available: [http://www.ewea.org/fileadmin/ewea_documents/documents/publications/reports/Pure Power II I.pdf](http://www.ewea.org/fileadmin/ewea_documents/documents/publications/reports/Pure_Power_II_I.pdf).
- [4] (2013, February 04). *Programme: Framework Programme Seventh - DeepWind (Future Deep Sea Wind Turbine Technologies)*. Available: http://cordis.europa.eu/projects/rcn/96069_en.html; [http://www.risoecampus.dtu.dk/Research/sustainable_energy/wind_energy/projects/VEA_Deep Wind.aspx](http://www.risoecampus.dtu.dk/Research/sustainable_energy/wind_energy/projects/VEA_Deep_Wind.aspx).
- [5] (2011, October 15). *DeepWind - Future DeepSea Wind Turbine Technologies*. Available: http://cordis.europa.eu/projects/rcn/96069_en.html.
- [6] F. V. T. Nica, P. D. Burlacu and S. Shivachev, "Control of a 5MW multilevel converter for wind turbine application," Aalborg University, May. 2013.
- [7] B. Daniela and B. Ciprian, "Development of modulation strategies for NPC inverter addressing DC link balancing and CMV reduction," 2012.
- [8] B. Wu, *High-Power Converters and AC Drives*. Wiley. com, 2006.
- [9] da Silva, Edison Roberto C, E. Cipriano dos Santos and C. B. Jacobina, "Pulsewidth modulation strategies," *Industrial Electronics Magazine, IEEE*, vol. 5, pp. 37-45, 2011.
- [10] P. Pillay and R. Krishnan, "Modeling, simulation, and analysis of permanent-magnet motor drives. I. The permanent-magnet synchronous motor drive," *Industry Applications, IEEE Transactions On*, vol. 25, pp. 265-273, 1989.
- [11] M. P. Kazmierkowski, H. Tunia and J. Tomaszczyk, *Automatic Control of Converter-Fed Drives*. Elsevier, 1994.
- [12] P. C. Krause, O. Wasynczuk, S. D. Sudhoff and S. Pekarek, *Analysis of Electric Machinery and Drive Systems*. Wiley. com, 2013.
- [13] M. Štulrajter, V. Hrabovcova and M. Franko, "Permanent magnets synchronous motor control theory," *Journal of Electrical Engineering*, vol. 58, pp. 79-84, 2007.

- [14] P. C. Perera, F. Blaabjerg, J. K. Pedersen and P. Thogersen, "A sensorless, stable V/f control method for permanent-magnet synchronous motor drives," *Industry Applications, IEEE Transactions On*, vol. 39, pp. 783-791, 2003.
- [15] C. Perera, F. Blaabjerg, J. K. Pedersen and P. Thogersen, "Open loop stability and stabilization of permanent magnet synchronous motor drives using DC-link current," 2000.
- [16] R. S. Colby and D. W. Novotny, "An efficiency-optimizing permanent-magnet synchronous motor drive," *Industry Applications, IEEE Transactions On*, vol. 24, pp. 462-469, 1988.
- [17] Y. Nakamura, T. Kudo, F. Ishibashi and S. Hibino, "High-efficiency drive due to power factor control of a permanent magnet synchronous motor," *Power Electronics, IEEE Transactions On*, vol. 10, pp. 247-253, 1995.
- [18] T. M. Jahns, "Variable frequency permanent magnet AC machine drives," *Power Electronics and Variable Frequency Drives: Technology and Applications*, pp. 277-331, 1997.
- [19] M. Fatu, R. Teodorescu, I. Boldea, G. Andreescu and F. Blaabjerg, "IF starting method with smooth transition to EMF based motion-sensorless vector control of PM synchronous motor/generator," in *Power Electronics Specialists Conference, 2008. PESC 2008. IEEE*, 2008, pp. 1481-1487.
- [20] A. Kronberg, *Design and Simulation of Field Oriented Control and Direct Torque Control for a Permanent Magnet Synchronous Motor with Positive Saliency*, 2012.
- [21] I. Boldea, M. C. Paicu and G. Andreescu, "Active flux concept for motion-sensorless unified AC drives," *Power Electronics, IEEE Transactions On*, vol. 23, pp. 2612-2618, 2008.
- [22] C. L. Phillips and D. Royce, "Harbor, Feedback control systems," *M.: Лаборатория Базовых*, 1988.
- [23] C. Bohn and D. Atherton, "An analysis package comparing PID anti-windup strategies," *Control Systems, IEEE*, vol. 15, pp. 34-40, 1995.
- [24] R. Ottersten, *On Control of Back-to-Back Converters and Sensorless Induction Machine Drives*. Chalmers University of Technology, 2003.
- [25] T. A. Lipo, *Vector Control and Dynamics of AC Drives*. Oxford University Press, 1996.
- [26] J. Chen, T. Liu and C. Chen, "Design and implementation of a novel high-performance sensorless control system for interior permanent magnet synchronous motors," *Electric Power Applications, IET*, vol. 4, pp. 226-240, 2010.
- [27] (2008, January 17). *SK50MLI065* [Online]. Available: <http://www.usbid.com/assets/datasheets/89/SK50MLI065.PDF>.

[28] (2011, March 25). *Fully Integrated, Hall Effect-Based Linear Current Sensor IC with 3 kVRMS Voltage Isolation and a Low-Resistance Current Conductor*. Available: <http://www.allegromicro.com/~Media/Files/Datasheets/ACS756-Datasheet.ashx>.

[29] J. N. Khan, "Design Considerations in Using the Inverter Gate Driver Optocouplers for Variable Speed Motor Drives," .

[30] M. P. Kazmierkowski, H. Tunia and J. Tomaszczyk, *Automatic Control of Converter-Fed Drives*. Elsevier, 1994.

[31] C. Kingsley and S. D. Umans, *Electric Machinery*. McGraw-Hill Companies, 2003.